



COOLING HISTORY OF A RIFTED PASSIVE MARGIN –
NEW INSIGHTS FROM (U-TH)/HE
THERMOCHRONOLOGY ALONG THE LABRADOR
PASSIVE MARGIN

Sarima Vahrenkamp

SUBMITTED IN PARTIAL FULFILLMENT OF THE REQUIREMENTS FOR
THE DEGREE OF BACHELOR OF SCIENCES, HONOURS,
DEPARTMENT OF EARTH SCIENCES
DALHOUSIE UNIVERSITY, HALIFAX, NOVA SCOTIA

April 2019



Department of Earth Sciences
Halifax, Nova Scotia
Canada B3H 4R2
(902) 494-2358

DATE: 28 April 2017

AUTHOR: Sarima Vahrenkamp

TITLE: Cooling History of a Rifted Passive Margin - New Insights from (U-Th)/He
Thermochronology along the Labrador Passive Margin

Degree: B. Sc. Honours Earth Sciences Convocation: May Year: 2017

Permission is herewith granted to Dalhousie University to circulate and to have copied for non-commercial purposes, at its discretion, the above title upon the request of individuals or institutions.

THE AUTHOR RESERVES OTHER PUBLICATION RIGHTS, AND NEITHER THE THESIS NOR EXTENSIVE EXTRACTS FROM IT MAY BE PRINTED OR OTHERWISE REPRODUCED WITHOUT THE AUTHOR'S WRITTEN PERMISSION.

THE AUTHOR ATTESTS THAT PERMISSION HAS BEEN OBTAINED FOR THE USE OF ANY COPYRIGHTED MATERIAL APPEARING IN THIS THESIS (OTHER THAN BRIEF EXCERPTS REQUIRING ONLY PROPER ACKNOWLEDGEMENT IN SCHOLARLY WRITING) AND THAT ALL SUCH USE IS CLEARLY ACKNOWLEDGED.

Distribution License

DalSpace requires agreement to this non-exclusive distribution license before your item can appear on DalSpace.

NON-EXCLUSIVE DISTRIBUTION LICENSE

You (the author(s) or copyright owner) grant to Dalhousie University the non-exclusive right to reproduce and distribute your submission worldwide in any medium.

You agree that Dalhousie University may, without changing the content, reformat the submission for the purpose of preservation.

You also agree that Dalhousie University may keep more than one copy of this submission for purposes of security, back-up and preservation.

You agree that the submission is your original work, and that you have the right to grant the rights contained in this license. You also agree that your submission does not, to the best of your knowledge, infringe upon anyone's copyright.

If the submission contains material for which you do not hold copyright, you agree that you have obtained the unrestricted permission of the copyright owner to grant Dalhousie University the rights required by this license, and that such third-party owned material is clearly identified and acknowledged within the text or content of the submission.

If the submission is based upon work that has been sponsored or supported by an agency or organization other than Dalhousie University, you assert that you have fulfilled any right of review or other obligations required by such contract or agreement.

Dalhousie University will clearly identify your name(s) as the author(s) or owner(s) of the submission, and will not make any alteration to the content of the files that you have submitted.

If you have questions regarding this license please contact the repository manager at dalspace@dal.ca.

Grant the distribution license by signing and dating below.

Name of signatory

Date

Table of Contents:

Table of Contents:	I
List of Tables:	III
List of Equations:	III
List of Figures:	IV
Abstract:	V
Introduction:	1
Geodynamic and Geologic Setting	4
Precambrian	4
Geology of the Hopedale Block.....	4
Formation of the Nain Province.....	6
Initiation of the Labrador – Greenland Rift System:	8
Rifting along the Greenland margin	9
Rifting along the Labrador Margin:.....	12
Post Spreading Subsidence:.....	20
Northern Rift Margins :	20
Thermochronology Methods and Results:	21
Introduction to low-temperature thermochronology:	21
Selection of sample locations:	22
Sample Preparation	23
Crystal Isolation:.....	23
Wilfley Table:.....	23
Heavy Liquid Mineral Separation:	24
Frantz Isodynamic Separator:	26
Picking of Apatites and Zircons:	26
Analytical Procedures:	26
Laser Extraction and Helium Measurement:	26
Measurement of U and Th:	27
Isotope Calculations:	27
Principles of the (U-Th)/He method and age calculation	28
Helium ingrowth	28
Alpha particle ejection and correction	30
Helium Diffusion	32
Age Calculation:	34
Results:	35
(U-Th)/He Results:	35
Apatite (U-Th-Sm)/He age results:	35
Sample SAR013.....	36
Sample SAR066.....	37
Sample SAR069.....	37

Zircon (U-Th)/He Age Results:.....	37
Sample SAR013.....	39
Sample SAR067.....	39
Sample SAR068.....	39
Sample SAR069.....	39
Interpretation of Results:.....	40
Age Trend along the Transect:.....	40
.....	41
Age versus Effective Uranium:.....	41
Apatite:.....	41
Zircon:.....	44
Thermal modelling:.....	46
HeFTy:.....	46
Setup of the models:.....	48
Modelling Result Descriptions:.....	55
Model 1:.....	55
Model 2:.....	56
Discussion.....	57
Conclusion:.....	60
References.....	61
Appendix 1: Apatite Grains.....	65
Appendix 2: Zircon Grains.....	71

List of Tables:

Table 1	Locality, age and composition of dyke swarms in Greenland.....	10
Table 2	A ₁ and A ₂ values for calculating the fraction of He retained.....	31
Table 3	Reduced data from Apatite (U-Th)/He dating.....	36
Table 4	Reduced data measured from (U-Th)/He dating of Zircons.....	38
Table 5	Thermal model parameters and results.....	50

List of Equations:

Equation 1	Natural Isotope Mass Calculation	28
Equation 2	Helium Ingrowth Equation.....	28
Equation 3	Fraction of He retained.....	31
Equation 4	Bulk He fraction.....	31
Equation 5	Fraction of He derived from ²³⁸ U.....	31
Equation 6	Arrhenius Equation.....	32
Equation 7	Dodson Equation.....	33
Equation 8	Age Calculation.....	34

List of Figures:

Figure 1	Map of Labrador Sea showing study area.....	1
Figure 2	Schematic representation of magma – poor versus magma – rich margins.....	2
Figure 3	Geological provinces of Labrador	4
Figure 4	General geology of the Hopedale block.....	5
Figure 5	Cross-section of collision between Nain province and Superior province.....	7
Figure 6	Labrador Sea outlining Saglek and Hopedale basins.....	8
Figure 7	Location of intrusions related to rifting on the Greenland margin.....	11
Figure 8	Map of Labrador Sea showing location of wells and seismic sections.....	14
Figure 9	Seismic section of Labrador Shelf.....	15
Figure 10	Labrador Shelf stratigraphy.....	17
Figure 11	Early rift to late rift schematic diagram.....	19
Figure 12	Geothermal gradient determined by tectonic and geodynamic settings.....	21
Figure 13	Range of closure temperatures for different thermochronometers.....	21
Figure 14	Sample location sites.....	22
Figure 15	Disk mill at Dalhousie University.....	23
Figure 16	Schematic diagram of Wilfley table.....	24
Figure 17	Hand magnet separation and heavy mineral separation	25
Figure 18	Alpha Decay chain.....	29
Figure 19	Alpha Decay outcomes in alpha particle.....	30
Figure 20	Closure temperature for apatite and zircon.....	33
Figure 21	Horizontal distance versus corrected age of dated grain.....	41
Figure 22	Effect of radiation damage on apatite grains.....	42
Figure 23	(U-Th)/He ages versus effective uranium concentration.....	43
Figure 24	Apatite corrected age vs. effective U content in apatite.....	44
Figure 25	Time temperature graphs for zircons due to eU - age relationship.....	45
Figure 26	Corrected age of zircons vs. the effective uranium content.....	46
Figure 27	Representative HeFTy inversion model for SAR013.....	51
Figure 28	Representative HeFTy inversion model for SAR066, SAR067.....	52
Figure 29	Representative HeFTy inversion model for SAR069, SAR068.....	53
Figure 30	Representative HeFTy inversion model for SAR069.....	54
Figure 31	Diachronous rifting along the Labrador margin.....	58

Abstract:

The Labrador Sea formed by rifting and breakup between Labrador and Greenland. The asymmetry of magmatism, bathymetry/topography, sediment distribution and crustal structure along both margins suggests a lithospheric – scale simple shear model of rifting. The initiation of rifting has been attributed to the Late Triassic to Jurassic (223–150 Ma) based on phlogopite Rb-Sr dating and U-Pb dating of perovskite found in dikes emplaced in southwest Greenland. Less rift – related magmatic activity has been found on the Labrador side, with the oldest ages determined from Early Jurassic–Early Cretaceous ages (197-145 Ma) through fossils found within a diatreme. There is still ongoing debate on when seafloor spreading initiated, which represents the end of rifting. The oldest undisputed oceanic crust has been dated to 63.0 ± 0.7 Ma, correlating to magnetic anomaly polarity Chron C27. Older ages have been attributed to 72.1 Ma (Chron C32) for Southern Labrador and 66.0 Ma (Chron C28) for northern Labrador. Cessation of spreading has been constrained stratigraphically to the late Eocene to early Oligocene. Low temperature thermochronometry includes a range of methods used to retrieve the thermal history of the uppermost crust, allowing to date and identify tectonic, magmatic and/or surface processes that have contributed to this thermal history. In this study, five bedrock samples were collected along a 200 km long transect along the Labrador passive margin between Nain (56.5417°N , 61.6969°W) and Hopedale (55.4580°N , 60.2115°W). Samples were dated using apatite and zircon (U-Th)/He thermochronometry, with closure temperatures of $\sim 70^{\circ}\text{C}$ and $\sim 170^{\circ}\text{C}$, respectively. The purpose of this study was to determine whether the low temperature thermal history of the Labrador margin recorded the rifting history and could thereby help constrain the initiation of rifting and the spatial and temporal propagation of the rift. Numerical models were used to quantify the cooling history of the margin to help determine the time-temperature history. Thermochronological data showed slow cooling between 1200 Ma to 250 Ma followed by more rapid exhumation which initiated during the Jurassic – Early Cretaceous, contemporaneous to the initiation of rifting. Time-temperature paths showed a northward decreasing age of initiation of cooling which we interpret to be due to diachronous rifting from south to north.

Acknowledgements:

I would like to thank Isabelle Coutand for her guidance, dedication and countless amounts of support throughout this project. I would also like to thank Deanne van Rooyen for giving me the opportunity to do field work in Labrador and Roman Kislitsyn for his help during the procedural aspects of this project. To Kara Vogler, thank you for all your help throughout this project and for being the greatest mentor.

Lastly, I would like to thank my family and friends for all the love and care they have given me throughout these last 4 years. I could not have done it without you.

Introduction:

The Labrador Sea is a narrow oceanic basin with a width of 900 km, bordered by Labrador and Greenland (Figure 1). In the north, the Labrador Sea shallows and transitions into the 300 km wide Davis Strait, which leads to Baffin Bay. The Labrador Sea is a very unique system, as it is bound by volcanic (magma-rich) margins in the north and magma-poor margins in the south (Keen et al., 2012). These mark two end member extremes of rifted margins.

Volcanic margins occur when lithospheric mantle breaks before or at the same time as the crust, producing large volumes of syn-rift igneous rocks (Franke, 2013). These margins are characterized by rapid extension and seaward-dipping reflectors (SDRS) and require the presence of very hot mantle under the rift shortly before breakup in order to generate the large volumes of magma (Franke, 2013).

Magma-poor margins show breakup of the entire crust before breakup of the lithospheric mantle. These margins are typically broken into a succession of zones which include 1) a zone of limited crustal stretching, 2) a zone of hyperextended crust, 3) exhumed mantle, and 4) ultra-slow-spreading or normal oceanic crust (Figure 2) (Doré and Lundin, 2015). Hyperextension occurs when the

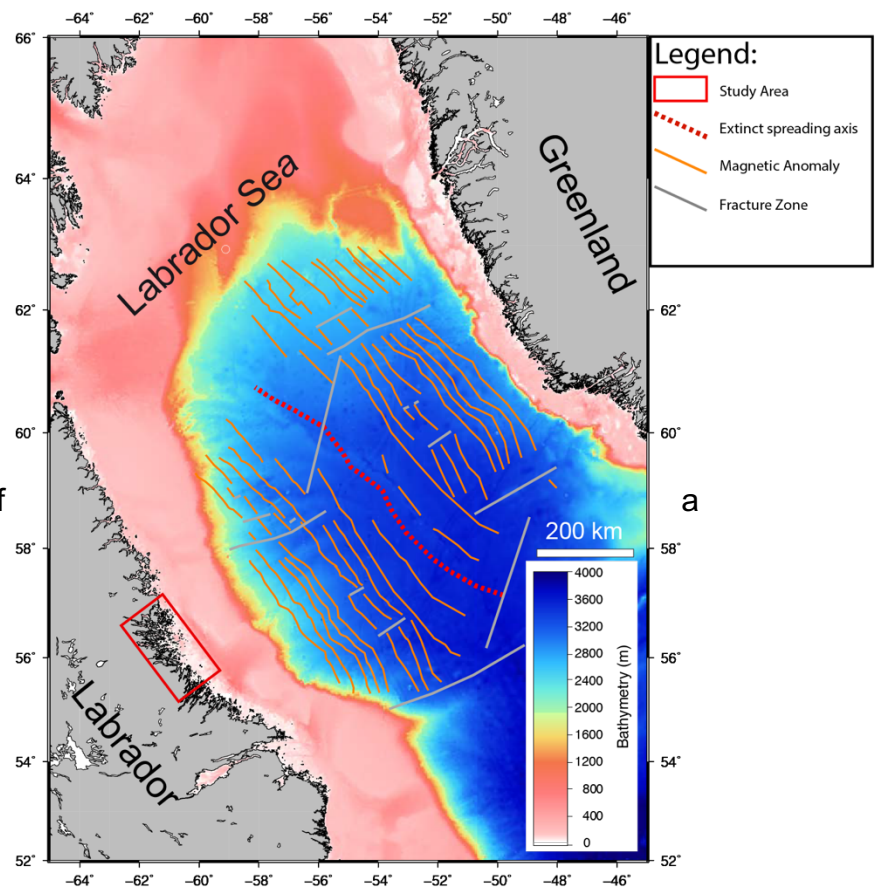


Figure 1; Map showing study area along Labrador margin. Extinct spreading axis is shown by dashed red line. Modified from Peace et al. (2016).

lower and the upper crust couple and begin to act in a brittle manner. This allows major listric faults to penetrate the mantle, causing serpentinization of the uppermost mantle. In the Labrador Sea, there are hyperextended basins (Hopedale and Saglek) and an 80 km wide transition zone of serpentinized mantle (Dickie et al. 2011).

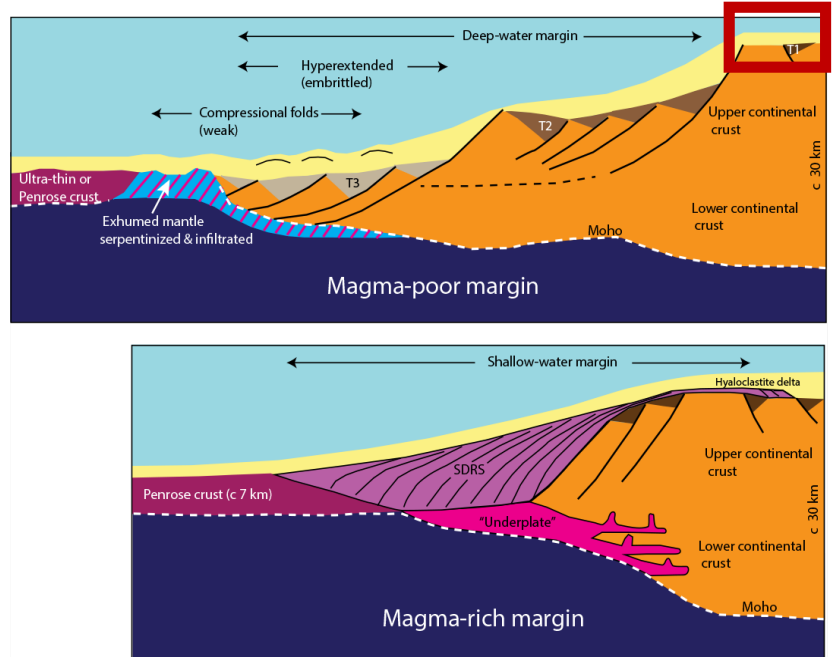


Figure 2; Schematic representation of magma-poor (top), compared to magma-rich (bottom) rifted margins (Doré and Lundin, 2015). Red box indicates relative location of study area along the rifted margin. Area was affected by rift-related processes but was not exposed to a thermal input.

The focus of this study is the southern Labrador Sea, a magma poor margin. Such margins are characterized by listric faults bounding rift basins along the proximal parts of the margin. The distal margin is characterised by extremely thinned crust that transitions to an area of exhumed subcontinental mantle before reaching ocean crust (Franke, 2013). Basins along the Labrador margin show up to 11 km of syn- and post rift sediment infill compared to the Greenland margin which show less than 2 km thick sediment deposits (Peace et al. 2016).

The Labrador Sea is the result of a now extinct rift system between Labrador on the North American plate and Greenland. The initiation of rifting of the Labrador Sea has been attributed to Late Triassic to Jurassic based on Rb-Sr and U-Pb dating of dikes in southwest Greenland (Larsen et al., 2009). There is still ongoing debate on the timing and duration of rifting, from its onset until its end, when Labrador seafloor spreading began. The initiation of spreading has also been difficult to constrain as fracture zones are buried under thick layers of sediment and magnetic anomalies show variable signatures making them difficult to correlate (Srivastava 1978). Spreading models produced show the first formation of oceanic crust with magnetic anomalies at C33 (83- 79 Ma) (Srivastava 1978). Other models were not able to show magnetic

anomalies older than C27 (62- 63 Ma) (Larsent et al. 2009). The break-up between these conjugate margins has been suggested to be asymmetrical based on evidence of magmatism, bathymetry, sediment distribution and crustal structure (Peace et al. 2016). Outstanding questions in this region include: 1) uncertainties on timing of rift initiation, 2) what is the spatial and temporal propagation of rifting and 3) the post break-up thermal and erosional history of the Labrador margin.

Thermochronometry along passive margins, used in conjunction with thermal modeling models and field observations can give insight to the tectonic processes involved during pre-, syn-, and post-rift phases (Wildman et al. 2019). Additionally, thermochronometers can be used to constrain the timing and rates of exhumation associated with passive margins and rifting (Wildman et al. 2019). The purpose of this study is to determine the spatial and temporal thermal history of the upper continental crust of the Labrador margin along the coastline from Hopedale to Nain using low temperature thermochronometry, and to identify the potential responsible processes. To achieve this, five bedrock samples were collected parallel to the coastline in the summer of 2018, over a length of 200 km and processed for apatite and zircon (U-Th)/He dating. Age results were modelled using a numerical modelling software called HeFTy to quantify the crustal cooling history of the margin as a result of exhumation.

Geodynamic and Geologic Setting

Precambrian

Labrador is divided into five geological provinces; the Superior province, the Nain province, the Grenville province, the Makkovik province and the Churchill province (Figure 3). The study area is located in the Nain province, which is composed of the Hopedale block in the south and the Saglek block in the north. These two blocks were amalgamated prior to 2.8 Ga as suggested by: the intrusion of a granitoid pluton in an older gneiss complex at 2578 ± 3 Ma; intrusion of the same complex by regional dyke sets at 2559 Ma; and metamorphism and deformation at 2550 Ma (Connelly and Ryan, 1996).

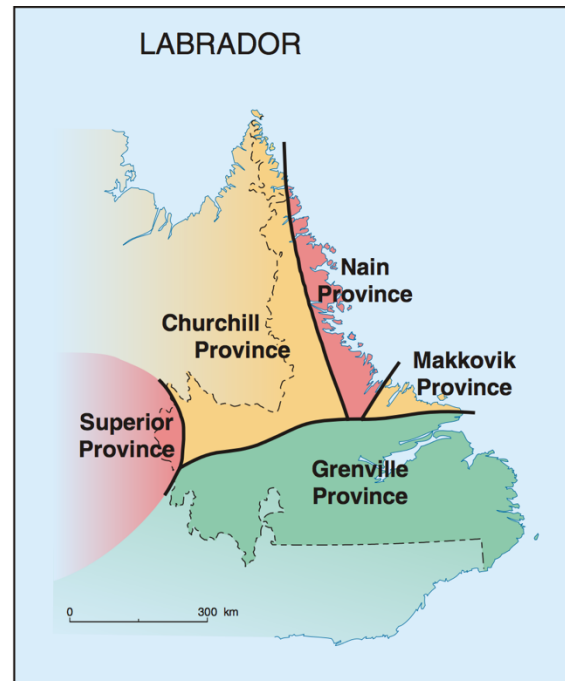


Figure 3; The five geologic provinces of Labrador (figure taken from www.nr.gov.nl.ca/nr/mines/maps/lab.pdf)

Geology of the Hopedale Block

The Hopedale block consists of 3.3 to 2.5 Ga old continental crust (James et al., 1996). The Maggo Gneiss, which covers most of the Hopedale block, is the oldest dated unit. It has an emplacement age of 3245 Ma (James et al., 2002). The block is bounded by shear zones separating it from the Churchill and Makkovik provinces to the West and South, respectively (James et al., 1996). See Figure 4 for the general geology of the Hopedale block.

Two volcanic suites occurred within the Hopedale block. The first is represented by the 3.1 Ga Hunt River volcanic belt, extending approximately 70 km NE-SW (Figure 4) and the second event is the 3.0 – 2.98 Ga Florence Lake volcanic belt (James et al., 2002). The Hunt River volcanic belt is composed of amphibolite – facies metavolcanic and metasedimentary rocks, while the Florence Lake volcanic belt has similar

composition to the Hunt River volcanic belt, but with higher percentage of komatiites and felsic volcanic rocks (James et al., 2002). Each volcanic event was followed by metamorphic and deformational episodes categorized as the Hopedalian, following the Hunt River volcanism, and the Fiordian, following the Florence Lake volcanism (James et al., 2002).

The Hopedalian deformational event has not been precisely dated, but dykes from the event do not intrude the Hunt River volcanic belt, indicating that deformation must have occurred after 3.1 Ga (James et al., 2002). During the Hopedalian, mafic lavas and aluminous and quartzofeldspathic sediments were deposited (Ermanovics, 1993). Sediments were metamorphosed to upper amphibolite facies with granulite facies metamorphism occurring at deeper crustal levels (Ermanovics, 1993). The Fiordian deformation event created a general northeast-plunging linear fabric and northeast trending planar fabric. This period of metamorphism affected the entire Hopedale block (Ermanovics, 1993). The growth of new zircons between 2960 – 2950 Ma in the Maggo Gneiss constrains the age of regional peak metamorphism and associated deformation during the Fiordian episode (James et al., 2002). The metamorphic grade of this episode ranges from greenschist facies in the southwest to upper amphibolite facies in the Northeast (James et al., 2002).

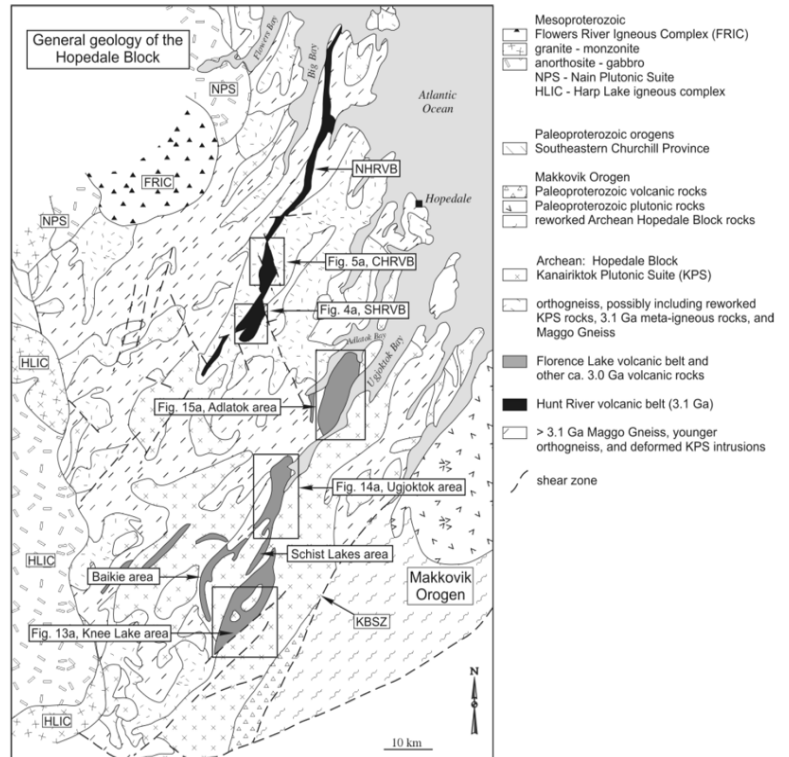


Figure 4; General geology of the Hopedale Block. The contact between the Kanairiktok Plutonic Suite, orthogneiss, and Maggo Gneiss units is highly approximate. CHRVB, central Hunt River volcanic belt; KBSZ, Kanairiktok Bay shear zone; NHRVB, northern Hunt River volcanic belt; SHRVB, southern Hunt River volcanic belt. Figure taken from James et al., (2002).

Formation of the Nain Province

The collision of the Nain province and Superior province (Figure 3) was an integral part of the formation of the Northeastern Canadian – Greenland shield and produced the Churchill province (Wardle et al., 2001). The Nain province was initially rifted from its parental craton between 2.2–2.1 Ga. During this time, a rifted margin formed and there was associated regional dyke emplacement (Figure 5- Stage 1). The Superior province also rifted from its parental craton at this time (Wardle et al., 2001). Between 1.91–1.89 Ga, there was eastward subduction below the Nain margin creating the Burwell domain in the Churchill province. At approximately 1.88 Ga, rifting resumed along the Superior margin, as well as the possible separation of the Archean Core zone from the Superior province (Figure 5- Stage 2) (Wardle et al., 2001). Between 1.87–1.85 Ga, the Nain province collided with the Core zone producing the Torngat Orogen. This thickened the continental crust to approx. 80 km and formed a crustal root (Figure 5 - Stage 3) (Wardle et al., 2001). The thickness of the crustal root in Labrador had a significant role in magmatism during subsequent rifting and opening of the Labrador Sea. At 1.845–1.820 Ga, there was deformation within the Torngat orogen causing axial sinistral shear that steepened earlier fabrics. During this time interval, eastward thrusting most likely buried the Nain craton (Figure 5- Stage 4). The Nain craton and the Core zone collided with the Superior craton between 1.82–1.77 Ga, forming the New Quebec Orogen and renewing the exhumation of the Torngat Orogen (Figure 5-Stage 5) (Wardle et al., 2001). The Kanairiktok shear zone marks the boundary between the Nain province and the Makkovik province. The shear zone is 1-2 km wide and composed of amphibolite and greenschist facies rocks (Ketchum et al., 2002). The shear zone is steeply dipping with a northeast trending planar fabric and subhorizontal linear fabrics (Ermanovics, 1993). The earliest movement along this zone was dated to ≥ 1870 Ma, implying that it formed during the collision between the Nain province and Labrador (Ketchum et al., 2002).

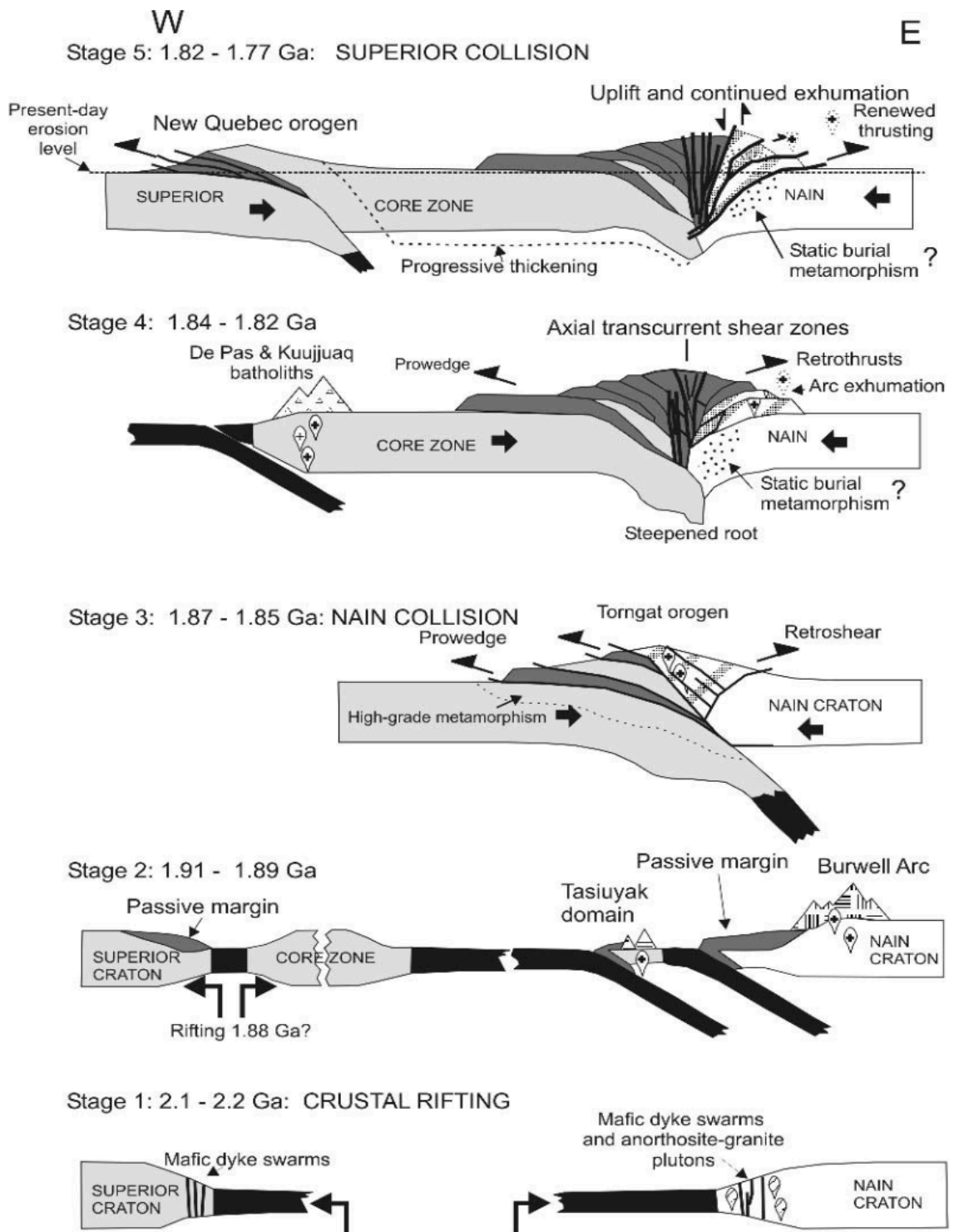


Figure 5; Showing a cross-section of the initial rifting of the Nain province from its parental craton to collision with the Superior province to create the Churchill province and the Torngat orogeny. (Wardle et al., 2001).

Initiation of the Labrador – Greenland Rift System:

The Labrador Sea is a 900 km wide oceanic basin separating the Labrador and Greenland rifted margins (Figure 6). There is limited chronological evidence regarding initiation and duration of rifting and the onset of spreading of the Labrador Sea (Peace et al. 2016). The rift system has been classified as an ultra-slow, asymmetric rift with breakup occurring closer to southwestern Greenland than Labrador (Peace et al. 2016). The margins display various rifting expressions with more evidence along the Greenland margin than the Labrador margin. The differences include: 1) rift – related dyke magmatism on the Greenland margin compared to minor magmatism on the Labrador margin, 2) a continental shelf margin of < 50 km wide off of Southwest Greenland and ~150 km wide on the Labrador margin and 3) less than 2 km thick sedimentary basins on the Greenland margin versus 8-11 km thick depocenters on the Labrador margin (Peace et al. 2016).

In the next sections, I will first describe the rifting expression along the Greenland margin in terms of geochronological, petrological, and stratigraphic evidences. Then I will analyze the rifting signal along the Labrador margin and the potential evolution from a rifting system to a spreading environment.

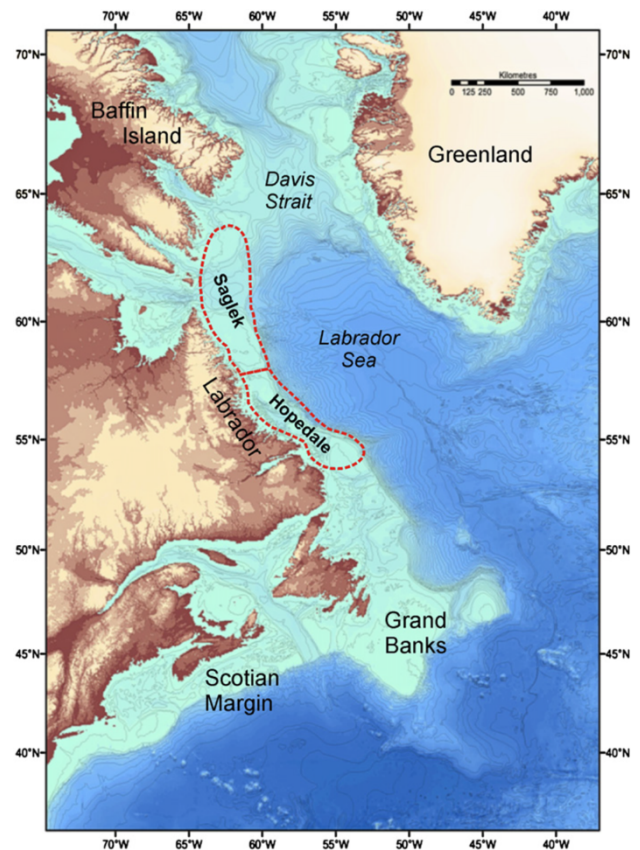


Figure 6: The Labrador Sea bounded by Greenland in the North west and Labrador in the southwest. Red dotted circles represent outlines of the Saglek and Hopedale Basin. Figure from Dickie et al. (2011).

Rifting along the Greenland margin

Geochronological and petrological evidences

In Greenland, the earliest evidence attributed to rifting are alkaline dykes emplaced during the Late Triassic to Late Jurassic (Larsen et al. 2009). The oldest mafic dyke was found in Færingehaven (Figure 7), yielding crystallization ages of 222.7 ± 0.3 Ma (Rb-Sr dating on whole rock and phlogopite, date determined using two points isochron) and 217.9 ± 5.8 Ma (Perovskite U-Pb dating) (Larsen et al. 2009). However, most dykes dated in this region yielded ages between 166–150 Ma (Table 1). These include a dyke in Færingehaven, located 6 km away from the oldest date dyke, which yielded ages of 158.9 ± 0.2 Ma (phlogopite Rb-Sr) and 153.4 ± 16.8 Ma (U-Pb dating on separated Perovskite). Localities of the dated dykes are reported in Figure 7.

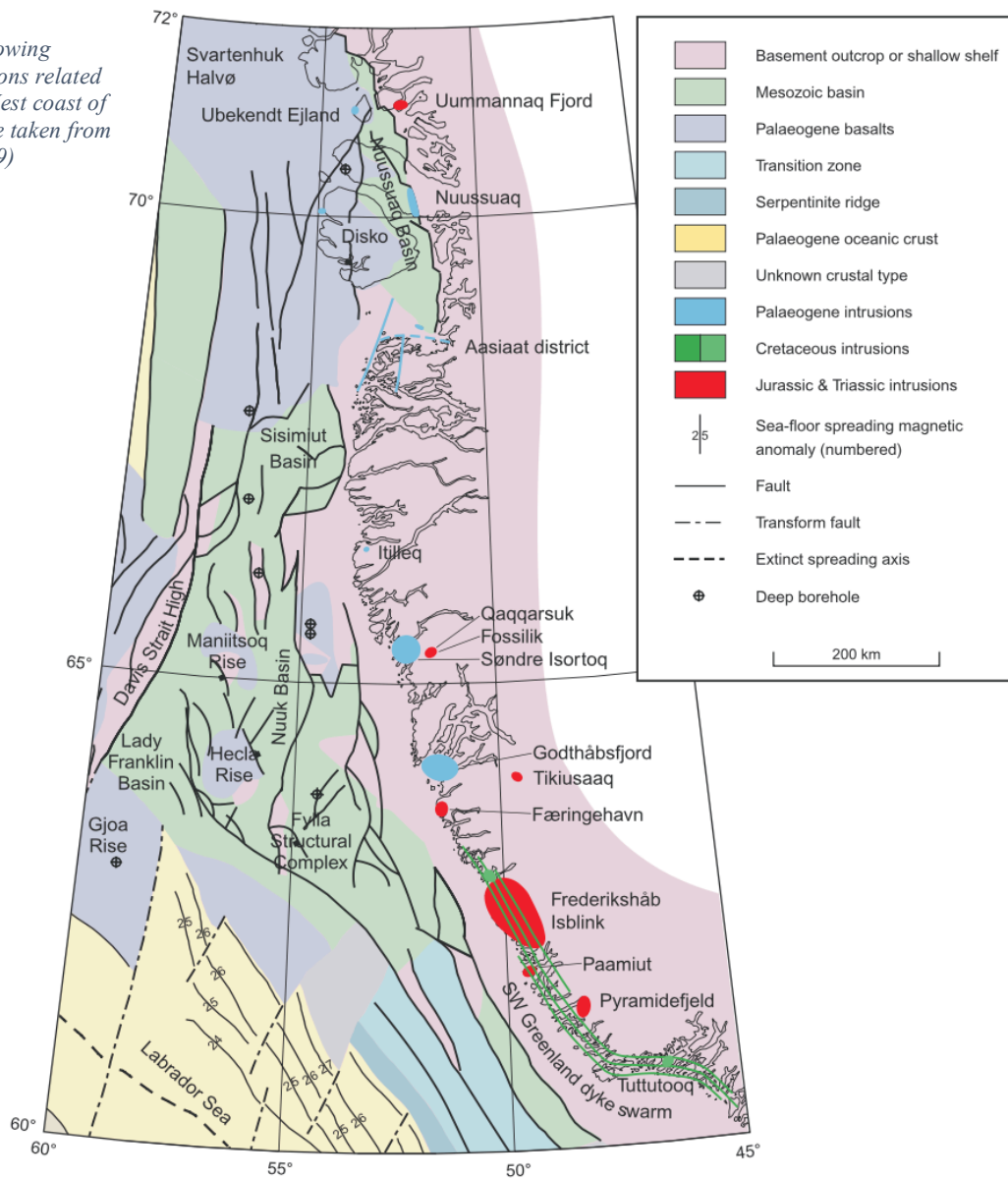
Locality	Lithology	Rock type	Method	Age (Ma)	Reference
Qaqqarsuk	Central complex and dykes	Carbonatite, aillikite	Rb-Sr, U-Pb	c. 165	Secher et al. (2009)
Fossilik	Explosive breccia	Aillikite	Rb-Sr	164.2 ± 1.8	Secher et al. (2009)
Tikiusaaq	Central complex and dykes	Carbonatite and aillikite	Rb-Sr, U-Pb	155-165	Tappe et. al (2009)
Færingehavn	Few dykes	Aillikite	Rb-Sr, U-Pb	159; 223	Larsen et. al (2009)
Frederikshåb Isblink	Loose dyke swarm	Monchiquite, alnöite, carbonatite, phonolite	Rb-Sr, U-Pb	106.1 ± 1.5, 149 -152	Larsen et. al (2009)
Paamiut	Small dyke swarm	Aillikite	K-Ar	166 ± 5	Larsen & Møller (1968)
Pyramidefjeld	Small dykes and sills	Aillikite	U-Pb	150 -152	Larsen et. al (2009), Frei et al. (2008)

Table 1; Locality, age and composition of dyke swarms from Late Triassic to Early Jurassic in West Greenland. Table modified from Larsen et al. (2009)

Dykes emplaced in the Late Triassic to Late Jurassic include aillikites, alnöites and carbonatites, which are all ultramafic alkaline rocks (Tappe et al., 2009). A petrogenetic relationship was found between carbonatite and aillikite dykes emplaced in Tikiusaaq based on the presence of abundant carbonate groundmass in the aillikite dykes that are found near the massive carbonatite sheets in Tikiusaaq, as well as their overlapping emplacement ages (Tappe et al. 2009). Emplacement ages of aillikite dykes range from 165 – 157 Ma (U-Pb dating on perovskite) and carbonatite sheets show ages between ~158 – 155 Ma (U-Pb dating of baddeleyite and pyrochlore) (Tappe et al., 2009). This petrogenetic relationship suggests that the proto-aillikite melt was parental to the carbonatite magmatic sheets which is a significant observation because it shows an evolution of the magma composition over time as rifting develops, which will be discussed in the following section (Tappe et al., 2009). Additionally, Tappe et al. (2009) suggests that due to a similar age range of magmatism at Qaqqarsuk and

Frederikshåb Isblink, dyke emplacement may indicate the presence of a regional stress field which produced this magmatism along the southwest Greenland margin. Due to the similarity in chemical composition, it may even indicate that magmatism was derived from the same source of melt (Tappe et al., 2009). The carbonatite – aillikite composition of this magmatism suggest that melt was generated at the asthenosphere–lithosphere boundary during initial cratonic rifting processes and represents the earliest evidence of rifting that eventually led to the opening of the Labrador Sea (Tappe et al., 2009).

Figure 7; Map showing location of intrusions related to rifting on the West coast of Greenland. Figure taken from Larsen et al. (2009)



In southwestern Greenland, evidence of the compositional evolution of the dykes attributed to rifting is observed (Larsen et al. 2009). As rifting evolves, higher degrees of melting at the lithosphere – asthenosphere boundary are expected with melts becoming increasingly enriched in SiO₂ and depleted in volatiles (Larsen et al. 2009). This suggests that at low degrees of melting, carbonatites and ultramafic alkaline silicate melts (e.g. aillikite and alnöite) dominate. As rifting develops, strongly under-saturated mafic alkaline melts (e.g. monchiquite and camptonite) are found, which progress into alkali basalts and tholeiitic basalts as the degree of melting increases (Larsen et al. 2009). This change in composition reflects the depth of melting, with lower degrees of melting expected at greater depths and higher degrees at shallower depths. As rifting evolves, the lithosphere and crust are stretched resulting in upwelling of the asthenosphere and shallower melt generation as well as increased degrees of melting due to a decrease in pressure (Doré and Lundin, 2015).

The dikes emplaced in Frederikshåb Isblink show rocks of Monchiquitic composition (higher degree of melting) and provide evidence of a regional extensional stress field with an overall NNW-SSE direction parallel to the Greenland margin (Figure 7) (Larsen et al. 2009).

During the Early Cretaceous a large, 400 km long coast – parallel dyke system emplaced along the southwestern Greenland margin (Figure 7) (Larsen et al., 2009). The dykes are composed of basaltic alkaline to enriched tholeiitic magma suggesting a higher degree of melting of asthenospheric origin at a shallower depth (Larsen et al. 2009). This is most likely due to asthenospheric upwelling due to lithospheric thinning.

In West Greenland a camptonite sill emplaced in Tuttutooq dated by ⁴⁰Ar/³⁹Ar to 115.4 ± 4.7 Ma and a coast parallel phonolitic dyke emplaced in Frederikshåb Isblink of 106.1 ± 1.5 Ma (Larsen et al., 2009). Camptonite and phonolite are symptomatic of intermediate degrees of melting.

Rifting along the Labrador Margin:

The rifting expression on the Labrador margin is less evident when compared to the Greenland margin. However, due to hydrocarbon potential, there has been significantly

more offshore exploration along the Labrador margin resulting in well logs and seismic data.

Petrographic Evidence:

Earliest evidence of rifting has been bio-stratigraphically dated by microfossils in a lamprophyric diatreme in Ford's Bight (shown in Figure 8 by blue dot) discovered by King and McMillan (1975). The Microfossils found were *Crepidolithus Crassus* which are restricted to the early-upper Jurassic (197-145 Ma) and deposited in a proximal marine environment (King and McMillan, 1975). The diatreme is inferred to have erupted through Jurassic and Lower Cretaceous marine sediments (King and McMillan, 1975).

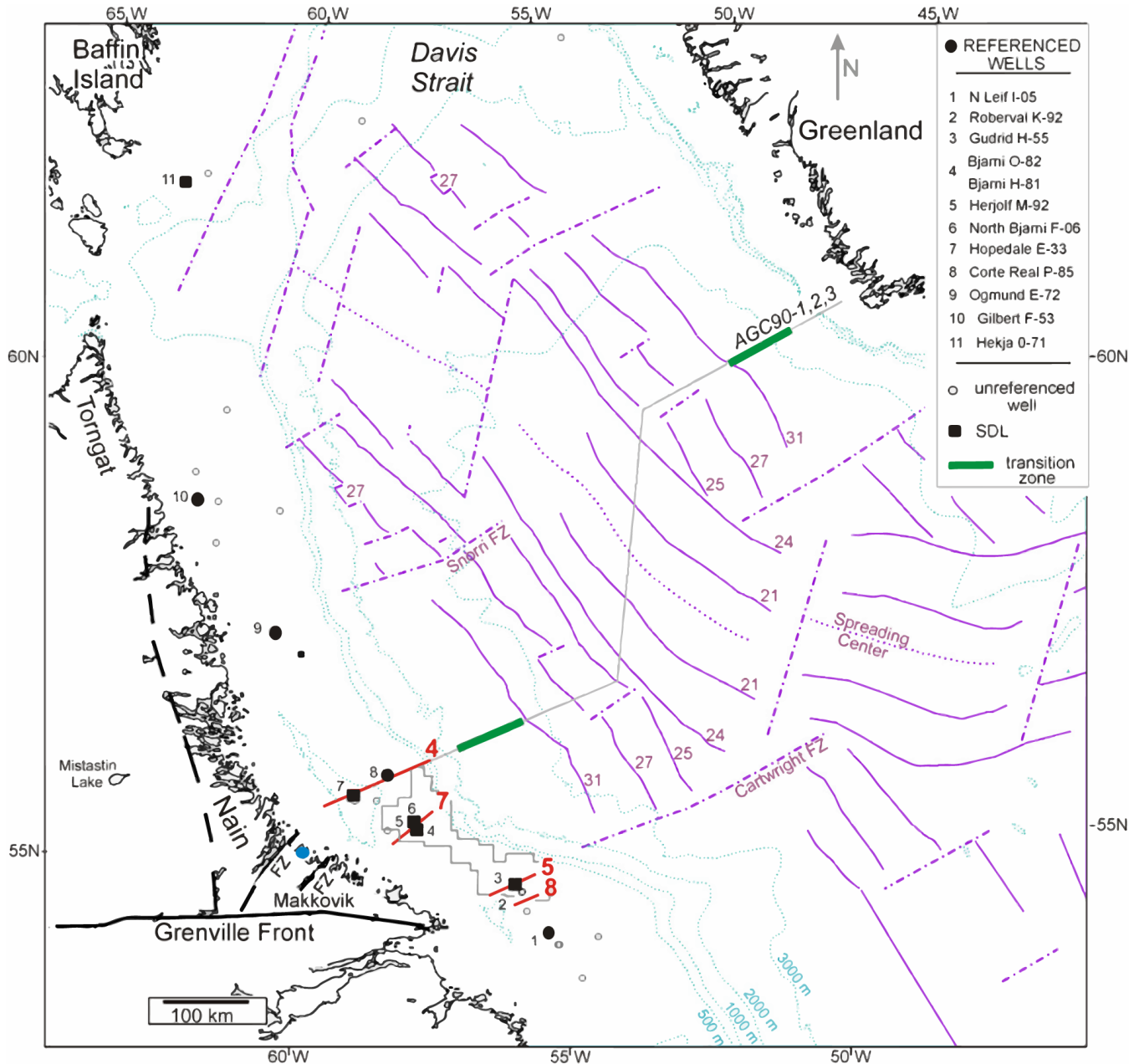


Figure 8; Map of the Labrador Sea. Ford's Bight, where the lamprophyric diatreme was found is shown with a blue dot. Well locations shown in the map. Additionally, location of the seismic profile in Figure 9 is given by line 4. Dotted blue lines show sea floor bathymetry. Purple lines show magnetic anomalies with associated magnetic anomaly ages, dot-dashed purple lines show fracture zones and the dotted purple line shows the spreading center. Red lines show seismic lines taken perpendicular to the Labrador margin. Green lines show the continent ocean transition zone. (Figure modified from Dickie et al. 2011).⁴

Stratigraphic Evidence:

The formations on the Labrador shelf are divided into three mega-sequences based on deposition during successive tectonic regimes (Balkwill et al. 1990): 1. intra-cratonic rifting, 2. cratonic separation of North America and Greenland followed by ocean spreading, and 3. post-spreading subsidence of the Labrador Sea oceanic crust. Insight into these sequences is a result of offshore wells paired with seismic data.

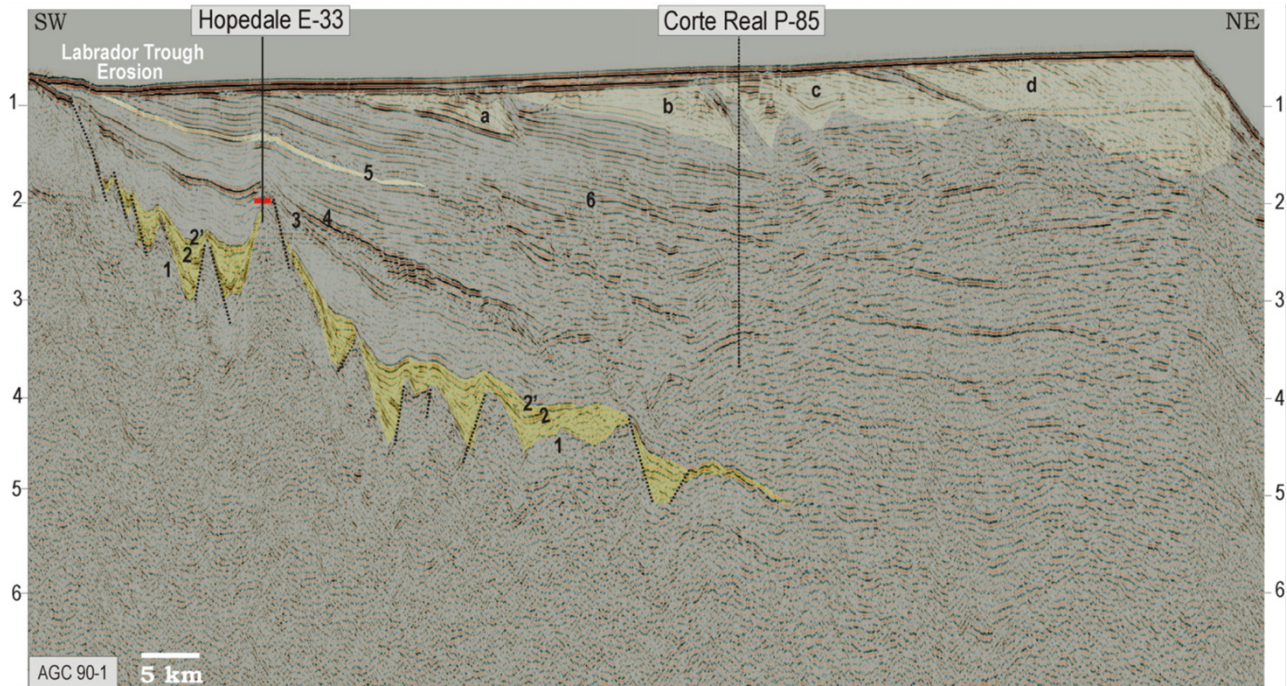


Figure 9; Seismic section of the Labrador continental shelf. Location of section is shown by line 4 in Figure 7. The vertical axis is in 2-way travel time (seconds). Gold color indicates sand prone units of the Early to Middle Cretaceous preserved in grabens and half grabens formed by steep normal faults. Pale yellow color at the top of the section show late Cretaceous and younger deposits. a, b, and d show clinoform developments from the Neogene. Numbers 1- 6 mark unconformities. Figure from Dickie et al. (2011).

Intra-Cratonic rifting:

Sediments deposited during intra-cratonic rifting overlay pre-rift basement or Paleozoic beds that are less than a few hundred meters thick (Balkwill et al. 1990). Prior to deposition of sediments during intra-cratonic rifting, extension and increased faulting of pre-rift basement resulted in the formation of half grabens and steep normal faults which cut the upper continental crust (Figure 9) (Dickie et al. 2011). Evidence of basement is only visible as a weak reflection beneath grabens and is therefore difficult to distinguish from overlying Paleozoic rock and syn-rift deposits and clastics (Dickie et al. 2011). The change from pre-rift to syn-rift deposits is defined by an unconformity and can be seen

in Figure 9 as (1). Volcanics of the Alexis formation commonly ground the grabens formed during intra-cratonic rifting and correspond to the earliest evidence of rifting preserved offshore Labrador. These volcanics have been dated as Early Cretaceous (131 ± 6 to 121 ± 5 Ma) using K-Ar dating on whole rock (Umpleby, 1979; Dickie et al. 2011). The formation was found at depths ranging from 1800 m to 4000 m (Geological survey of Canada, 1989).

The Alexis formation is overlain by syn-rift coarse-grained arkoses of the Bjarni Formation (Figure 10) (Balkwill et al., 1990; Dickie et al. 2011). The Bjarni formation was deposited in a predominantly non-marine environment transitioning to a marginal marine to lagoonal setting as global sea level was increasing (Figure 10) (Balkwill et al., 1990, Dickie et al. 2011). The sediment that makes up this formation is of local origin and is biostratigraphically constrained to the Hauterivian. The deposition of this formation marks a period of subsidence and sedimentation (Larsen et al., 2009). The top of the Bjarni formation is marked by an erosional unconformity during the Cenomanian stage.

The Markland formation, deposited during the Late Cretaceous, overlies this erosional unconformity and the upper members of this formation mark the transition from rifting to spreading. This transition is marked by a shift in narrowing of the upwelling asthenosphere, focusing extensional strain further offshore causing extreme lithospheric thinning near the area of eventual breakup (Dickie et al. 2011). Shales of the Markland formation onlap the underlying Bjarni unconformity (Dickie et al. 2011). The Markland formation contains a sandstone unit (Freydis member) which thins oceanward, transitioning into the marine shales of the Markland formation. The deposition of this formation marks a period of widespread marine transgression during the Campanian and Maastrichtian which most likely flooded most of the Labrador shelf (Dickie et al. 2011). Transgression is thought to have been very rapid due to the occurrence of deep marine shales of the Markland formation overlying much coarser grained deposits of the Bjarni formation (William et al., 1990).

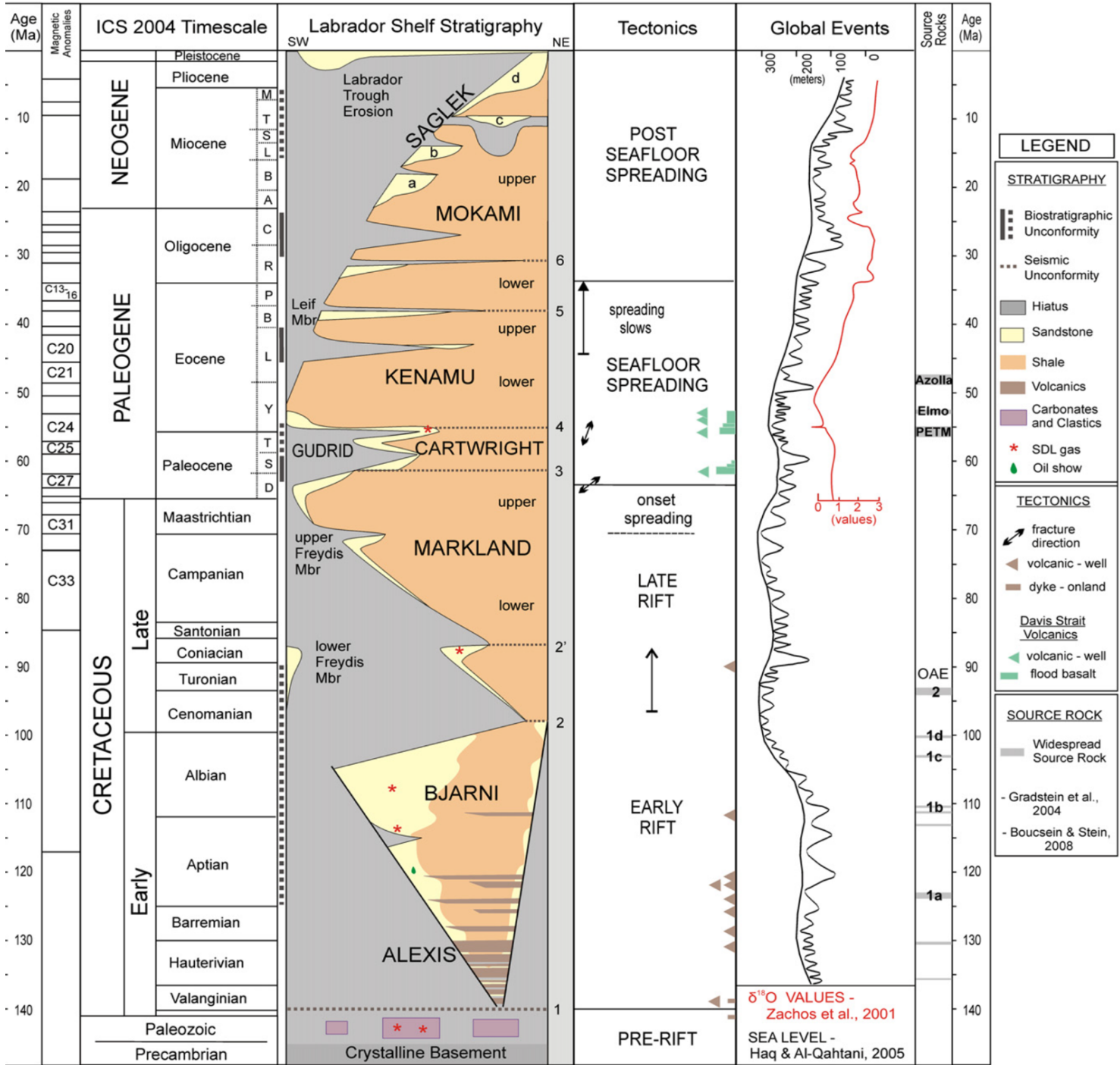


Figure 10; Labrador Shelf stratigraphy initiating with Alexis volcanic deposits. The tectonic column indicates the phase of rifting during the deposition of each formation. The black line in global events depicts sea level fluctuations, which plays a major role in the evolution of the Labrador margin. Figure taken from Dickie et al. (2011).

Additionally, the lack of deposition during the mid-Cretaceous (erosional unconformity) can be attributed to sediment starvation due to the marine drowning of coastal rivers (Balkwill et al. 1990). According to Dickie et al. (2011), this period of transgression corresponds to an increase in subsidence rate within the Hopedale Basin, due to the onset of spreading in the southern Labrador Sea and resulting cooling of the shelf region and margin.

Separation of North America and Greenland followed by ocean spreading:

During the Late Cretaceous to Paleocene, rifting and thinning led to break up of North America and Greenland and the formation of new oceanic crust. To constrain the beginning of seafloor spreading, scientists have analyzed magnetic anomalies of the sea-floor. Srivastava (1978) generated a magnetic anomaly map that identified C31 (68 Ma) as the beginning of sea floor spreading. However, the oldest undisputed age is Chron 27n (61.3-60.9 Ma) (Chalmers and Laursen, 1995). The age associated with these magnetic anomalies describes the evolution of spreading. The Labrador Sea spreading center has been classified as a slow to ultraslow spreading center by Delescluse et al. (2015). There was a re-orientation of the spreading axis around magnetochron 24r (55.9-53.3 Ma) after which there was a new stress orientation (N-S) (Abdelmalak et al., 2012). After the re-orientation of the spreading axis, there was a significant change in spreading rate from slow to ultra-slow (Delescluse et al., 2015). Spreading of the Labrador Sea ceased completely by Chron 13 (Chalmers 2001). Spreading ceased with a low magma supply: however, the tectonic nature behind the extinction of the spreading ridge is not yet fully understood (Delescluse et al., 2015).

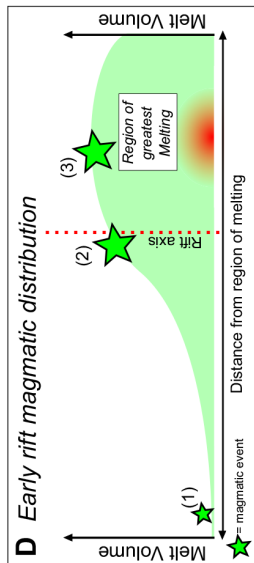
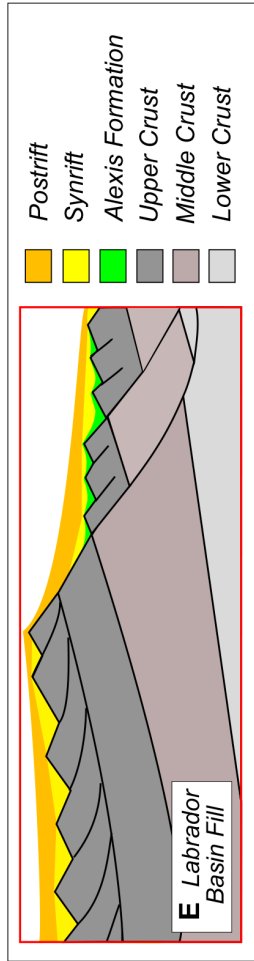
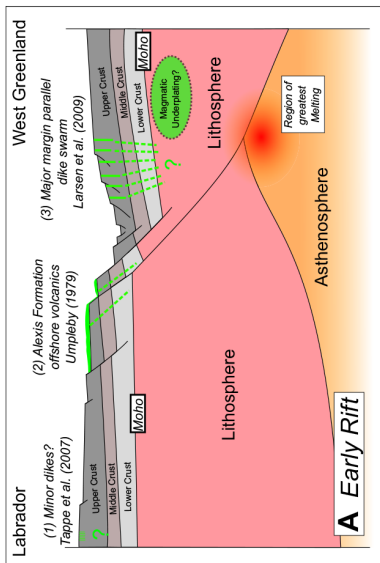
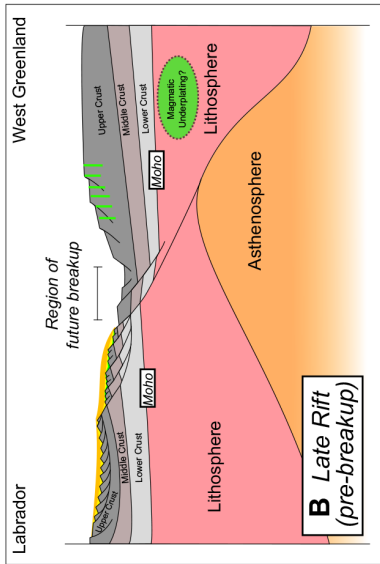
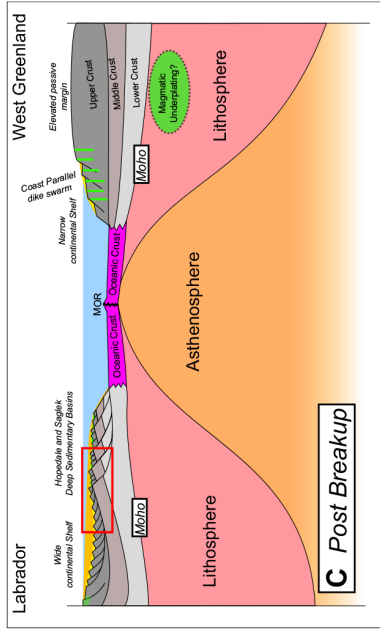


Figure 11: (A) Depicts early rifting under a simple shear rifting regime prior to the opening of the Labrador Sea. Magmatic events that occurred during this phase of rifting are shown in green. Early rift phase is dominated by steep normal faults that form with the initiation of extension. High angle normal faults result in uplift of the footwall, with increasing topography resulting in higher rates of erosion. (B) Depicts late rift phase prior to breakup. The upper crust of the Labrador margin is dominated by listric faults which create accommodation space for sediment infill shown by post and syn rift deposits. Prior to break up narrowing of extensional strain will focus the rift offshore to the location of the now extinct spreading ridge. (C) Post breakup architecture of the rifted conjugate margins after a simple shear rifting regime resulting in a wider Labrador margin compared to the Greenland margin. The sediment infilled Hopedale and Saglék basins are also visible where (E) depicts section of the basin showing their geometries. (D) shows early rift magmatic distribution with regard to distance from melting. The three magmatic events shown here can be seen in (A). Figure from Peace et al. (2016).

Post Spreading Subsidence:

The final mega-sequence deposited along the Labrador margin comprises the Mokami formation, which spans from the Early Oligocene to the Quaternary (Dickie et al. 2011). This phase involves thermal subsidence of the oceanic basin floor of the Labrador Sea (Balkwill et al. 1990). Additionally, there was uplift of coastal margins during this time, resulting in the deposition of coarse clastic deposits due to erosion of these higher relief areas (Balkwill et al. 1990). The subsidence rate of the Labrador Sea was not fast enough to accommodate sediment supply rates resulting in basinward progradation of the sediment deposits, forming the slope and continental shelf that is presently preserved (Balkwill et al. 1990).

Northern Rift Margins :

The Labrador margin has a different rifting expression in the north compared to the southern margin. The northern margin is a volcanic rifted margin (Keen et al. 2012). Additionally, deep seismic profiles taken perpendicular to both the volcanic and nonvolcanic margins displayed a reversal in asymmetry between conjugate margins in the north and south. In the volcanic margin, asymmetric rifting created a narrower margin on the Labrador shelf, and a wider one on the Greenland side (Keen et al. 2012). In contrast, in the south where our study is focused, Labrador is the wide margin and Greenland is the narrow margin.

Thermochronology Methods and Results:

Introduction to low-temperature thermochronology:

Thermochronology is a discipline based on radiometric dating that measures, in certain minerals, the growth of daughter isotopes from radioactive decay and the loss of those daughter products via thermally – activated diffusion, thereby giving insight into the thermal history of rocks and constraining the spatial and temporal evolution of various geologic processes (Reiners and Shuster, 2009; Braun 2006). Systems used for thermochronology are temperature dependent. A mineral begins to retain daughter isotopes, due to cooling, as it is brought closer to the surface by exhumation. England and Molnar (1990) define exhumation as the displacement of a rock with respect to the surface where the rate of exhumation will depend on the rate of erosion by surface processes (e.g. fluvial or glacial incision, landslides) and/or the removal of overlying crustal material by tectonic processes (e.g. normal faulting). The depth in the crust at which a mineral begins to retain daughter products varies in large part on the geothermal gradient, which is a result of the tectonic and geodynamic setting of the region (Braun 2006). The geothermal gradient is higher in tectonically active regions and lower in stable

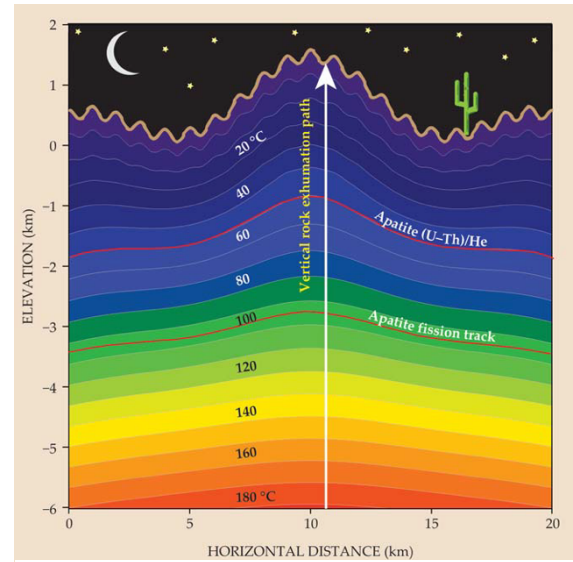


Figure 12; The geothermal gradient is determined by tectonic and geodynamic settings. Temperatures are represented by isotherms. Red lines indicate the closure temperature for apatite fission track and apatite (U-Th)/He. (Reiners and Shuster, 2009).

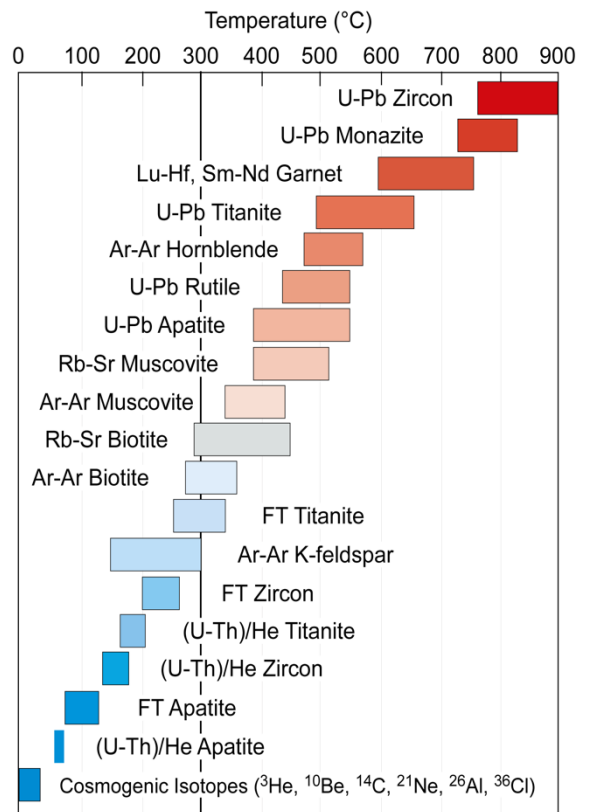


Figure 13; Range of closure temperatures for different thermochronometers (Courtesy of I. Coutand).

cratonic regions, and the shape of the isotherms can be influenced by the topography (Figure 13) (Reiners and Shuster, 2009).

This study applies apatite and zircon (U-Th)/He thermochronometry, which are low-temperature (≤ 200 °C) thermochronometers (Figure 13).

Selection of sample locations:

Field work was conducted with the Geological Survey of Canada from July 4th -26th, 2018 and based out of Hopedale, Labrador. Sample sites were selected along a 200 km long transect along the strike of the Labrador margin between Hopedale and Nain (Figure 14). Five bedrock samples were selected for dating based on their even spatial distribution along the coast and their rock type. Rocks were considered suitable for collection if they were likely to contain abundant apatite and zircon. Ideal rock types are silicic to intermediate intrusive igneous rocks (granite, granodiorite, diorite and tonalite), volcanics and orthogneisses. Collected samples were medium grained felsic metaplutonic granites, granodiorites, diorites and tonalities. A total of 3-5 kg of each sample was collected and shipped to Dalhousie University.

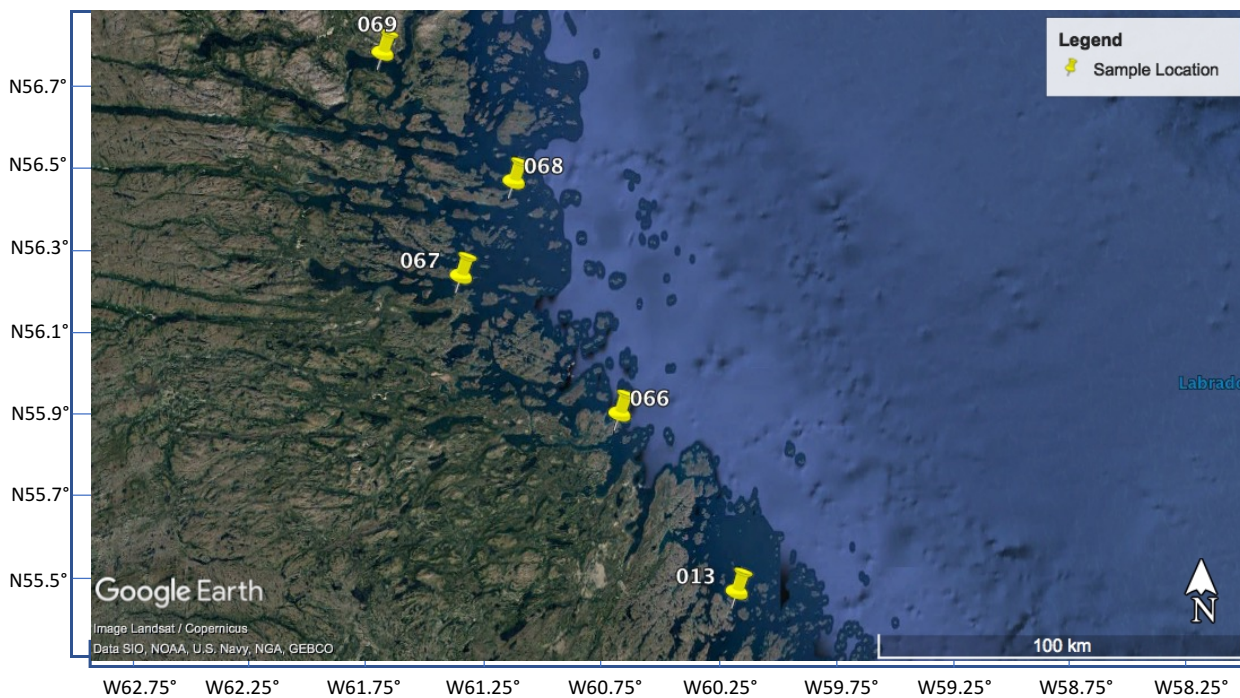


Figure 14; Sample location sites. Study area is shown by red box in Figure 1.

Sample Preparation

Crystal Isolation:

The rocks were broken into fist-sized pieces using a sledge hammer, crushed into gravel-sized fragments using a jaw crusher and then into medium-grained sand particles using a disk mill (Figure 15) at the Dalhousie University Rock Disaggregation facility. Grains were then sieved at 250 μm and the fraction finer than 250 μm was processed over a Wilfley table.



Figure 15; Disk mill used in the initial stage of crystal isolation. Sieve used was for 250 micrometers.

Wilfley Table:

On a Wilfley table, minerals undergo separation based on their respective density.

The medium-grained sand sample is placed into a feeder where it is gradually released to flow over the table. As it enters onto the table, which is inclined in two directions, it mixes with water as the table shakes back and forth, driven by a piston engine. This movement separates the minerals into different sections of the table as a function of their density (Figure 16). We collected the material in four trays containing heavy ($d \geq 2.86$), medium ($2.86 \geq d \geq 2.79$), and light ($d \leq 2.79$) minerals. The heavy minerals tray collects a concentrate of oxides, garnet, pyroxene, apatite and zircon (the latter two being the fractions of interest). Less dense minerals such as quartz, micas, feldspars and clay are retrieved in the light and medium trays. All trays are then placed into an air-forced Memmert oven where they are dried over 2 days at about 40 °C.

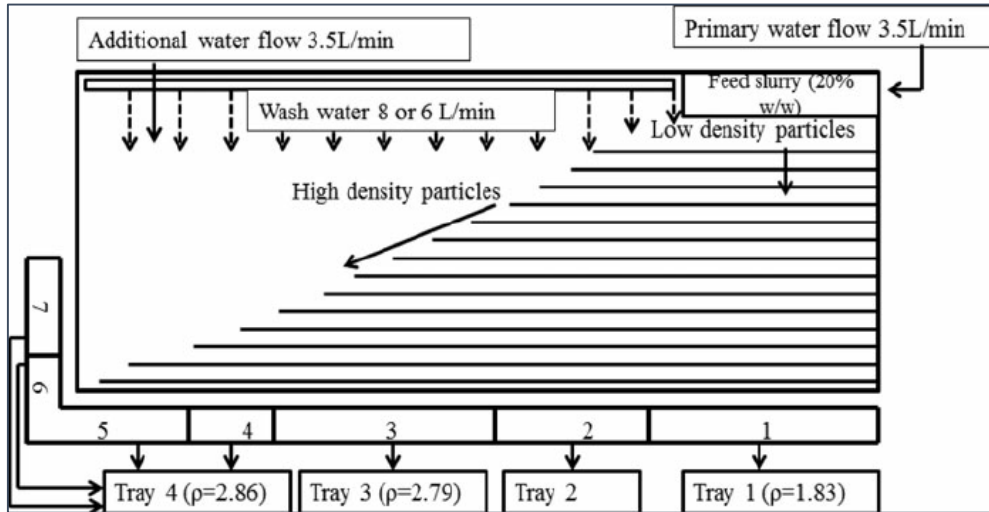


Figure 16; Schematic diagram of a Wilfley table. Sieved sample enters via the feed slurry onto the table and mix with water. Low Density particles are carried over the ridges by the water and are collected in tray 1 and 2. Grains of medium density are collected in tray 3. High density grains move along the ridges and are collected in tray 4. Figure from Palakkeel Veetil et al. (2014).

Heavy Liquid Mineral Separation:

The grains separated into the heavy tray in the previous step were cleaned using a hand magnet to remove highly magnetic oxides and then processed using heavy liquid mineral separation (Figures 17 a & b). The heavy liquid used for separation is Lithium Metatungstate (LMT) which is salt dissolved in deionized water with a density between 2.8-2.9 g/cm³. This process works through density-based separation where the sample is added to the LMT in a separatory funnel and thoroughly mixed. After a few minutes heavy minerals that have a density higher than that of the LMT sink to the bottom of the funnel and lighter minerals float at the top (Figures 17c & d). The solution is then purged, removing only the heavy minerals such as apatite and zircon which have densities of 3.19 g/cm³ and 4.85 g/cm³, respectively. The heavy minerals are then thoroughly cleaned to remove all LMT and placed back into the Memmert oven to be dried. Once dry they are cleaned again with a hand magnet to remove any remaining highly magnetic grains.

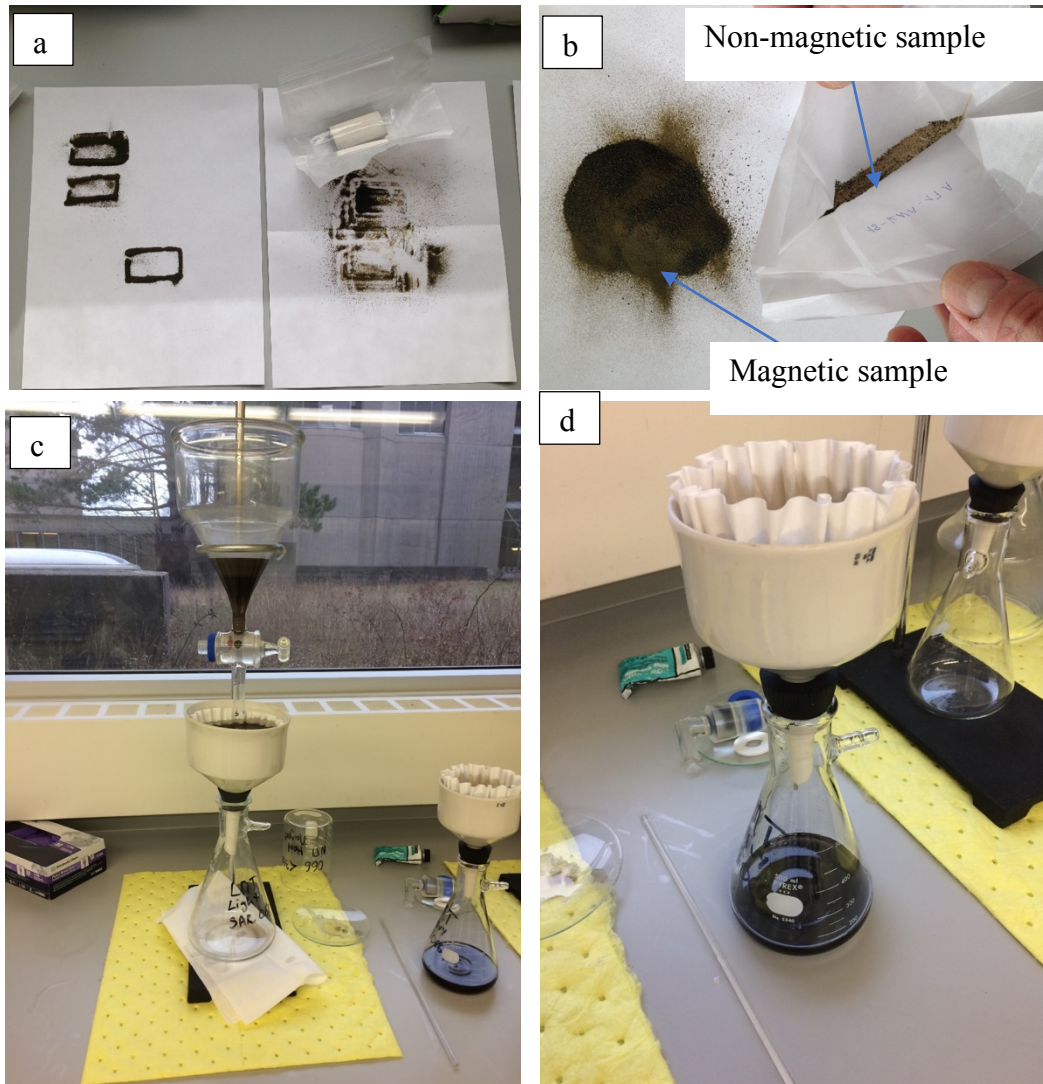


Figure 17; a. Separation of highly magnetic minerals via hand magnet. On the left sheet of paper are the removed magnetic grains. On the top right sheet of paper is the powerful hand magnet used. Grains on the right sheet of paper are remaining sample. b. shows a close up of the separated sample after the hand magnet has been used. The non- magnetic sample is composed of much lighter grains such as apatite's and zircons whereas the magnetic portion is composed of darker grains such as oxides. c. shows the separatory funnel filled with LMT and the sample. Less dense minerals will remain at the surface whereas dense minerals will sink to the bottom. After 15 minutes the knob is turned so that the sample can be purged and heavy mineral grains can be removed. Once the grains at the bottom of the funnel have been removed, remaining sample is stirred and then left to settle. The following purging steps are repeated until no more particles are settling at the bottom of the funnel. Once this occurs the Buchner funnel is removed and a new funnel is placed under the separatory funnel. Remaining less dense grains from the sample are collected into the second Buchner funnel. Heavy and light density samples are then thoroughly cleaned to remove all remaining LMT. d. Buchner funnel with coffee filters that are used to filter grains within LMT mixture. Photos taken in Dalhousie University Thermochronology Lab.

Frantz Isodynamic Separator:

The Frantz machine contains a powerful magnet that is used to further purify the heavy mineral fraction by removing more weakly magnetic grains. The device has an inclination of 15° to allow for gravity-based separation of grains that are not magnetic. Separation occurs via a feeder where the sample is divided into two chutes, with non-magnetic grains falling to the lower chute due to the inclination of the chute and the magnetic grains remaining in the higher chute as the magnetic attraction of the grains to the magnet overcome gravity. The sample is run through the magnet three times at increasing currents of 0.4 A, 0.8 A and 1.2 A. Remaining grains will be those with low magnetic susceptibilities including apatites, zircons, pyrite and galena.

Picking of Apatites and Zircons:

Apatite and zircon grains were picked using a Nikon SMZ1500 stereoscopic microscope equipped with transmitted, reflected and polarised light. Grains optimal for dating are prismatic, euhedral, contain both terminations, have high relief and birefringence, and no inclusions. Grain size should be between 70 -150 µm. Inclusions must be avoided as, especially in apatite, they are often zircon which would result in high He measurements and grain age. Apatite grains were selected based on the same criteria as zircons. Flat crystals were avoided as half the trajectories taken by alpha particles would lead to higher ejection (Farley, 2002). Measuring and packing of grains was done by Roman Kislitsyn.

Analytical Procedures:

Helium dating was carried out by Roman Kislitsyn in the Noble Gas Laboratory at Dalhousie University.

Laser Extraction and Helium Measurement:

The packed samples were first shipped to the TRAIL lab at the University of Colorado, Boulder to undergo He degassing. Individual grains were heated via a laser to extract He gas. Apatite grains were heated to 1050 °C for 5 minutes and zircon grains were

heated to 1250 °C for 15 minutes. After heating, a calibrated amount of ^3He spike was added to the vacuum line containing the sample gas. The spike, along with the sample gases were then frozen in a Cryogenic trap at 16 Kelvin. This allows for the accumulation of all the gases in one place, including other gases also released during heating (O, N, H₂O). Once frozen, the sample is heated to 37 Kelvin, at which He will return back to a gaseous state and other gases will remain frozen. A mass spectrometer (MS) was then used to measure the ratio of $^4\text{He} : ^3\text{He}$, which is the ratio between the known amount of spike added and the ^4He within the sample. This allows us to determine the amount of ^4He in the sample via isotope dilution method.

Measurement of U and Th:

Measurement of U and Th was done at Dalhousie University. To measure the parent, the individual apatite grains were dissolved in 7N HNO₃ and a spike of U²³⁵, Th²³⁰ and Sm¹⁴⁹ was added. The sample was heated in a Memmert oven between 80-90°C for 1.5 hours. 1 ml of water was then added to the solution. The solution was then analysed in an Inductively Coupled Plasma Mass Spectrometer (ICP-MS) to measure the ratios of the isotopes and spikes present.

The zircon grains were placed into capsules and diluted using hydrofluoric acid (HF) with some nitric acid (8:1 ratio) and a spike of U²³⁵, Th²³⁰, and Sm¹⁴⁹ was added. The solutions were then placed into the oven for 4 days at 200°C. Once the sample was cooled, the HF was dried down on a hotplate and 6N HCl was added. The sample was returned to the oven at 200°C for another 24 h. Once complete, the solution was heated using a hot plate until all HCl was vaporised. 7N HNO₃ was then added to the remaining solution and the sample was placed back in the oven for 1.5 h at 80°C. The solution was diluted with 1 mL of water and then analysed by ICP-MS.

Isotope Calculations:

The isotope dilution techniques were used to determine the amounts of ^4He , ^{238}U , ^{235}U , ^{232}Th and ^{147}Sm in the grain based on the natural isotope and a known isotopic

ratio from the added spike. The amount of specific radioisotope can be calculated using the following equation (Attendorn and Bowen, 1998):

$$N_w = S_w \left(\frac{W_N}{W_S} \right) \left(\frac{Ab_S^A - R_M \times Ab_S^B}{R_M \times Ab_N^B - Ab_N^A} \right) \quad \text{Equation 1}$$

Where N_w is the mass of the natural isotope A , S_w is the mass of spike isotope B , and W_N and W_S are the isotopic weights of the natural isotope and spike isotope respectively, Ab_S^A , Ab_S^B , Ab_N^B and Ab_N^A are the relative abundances of isotopes A in nature and B in the spike, and R_M is the ratio of isotopes A and B which is measured in the ICP-MS (Attendorn and Bowen 1998). Once N_w has been solved for, it is divided by the molar mass of the specific isotope to find its molar concentration, which will be used in the age equation.

Principles of the (U-Th)/He method and age calculation

Helium ingrowth

^4He is produced by the decay of ^{238}U , ^{235}U , ^{232}Th and to a lesser amount ^{147}Sm (Farley 2002). The ingrowth of ^4He with time can be defined using equation 2.

$$^4\text{He} = 8^{238}\text{U} (\exp (\lambda_{238} t) - 1) + 7 (^{238}\text{U} / 137.88)(\exp (\lambda_{235} t) - 1) + 6 (^{232}\text{Th} (\exp \lambda_{232} t) - 1) \quad \text{Equation 2}$$

Here ^4He , U and Th refer to present day concentrations in the crystal, t refers to accumulation time and λ is the decay constant for the various isotopes ($\lambda_{238} = 1.551 \times 10^{-10} \text{yr}^{-1}$, $\lambda_{235} = 9.849 \times 10^{-10} \text{yr}^{-1}$, $\lambda_{232} = 4.948 \times 10^{-11} \text{yr}^{-1}$). Coefficients in front of the isotope describe the number of alpha particles emitted in each of the decay series (Figure 18). The value expressed with ^{238}U (1/137.88) represents the present day $^{235}\text{U}/^{238}\text{U}$ ratio (Farley 2002).

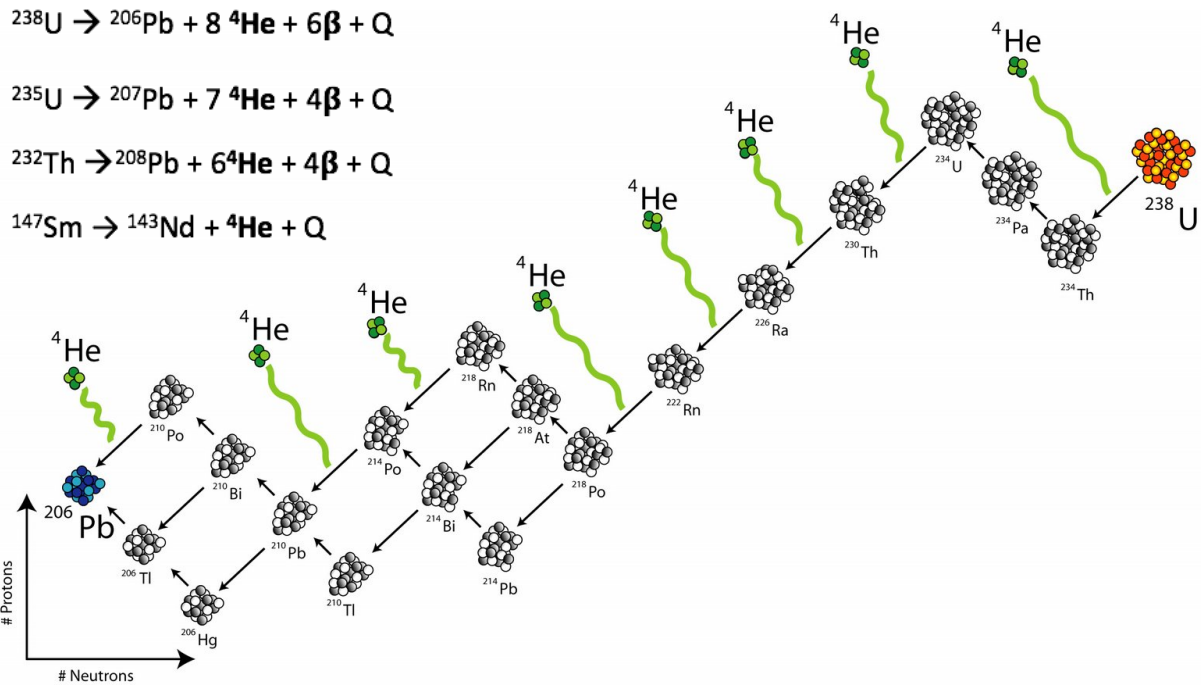


Figure 18; Alpha decay chain of ^{238}U with products of the other decay chains shown in the top left (<http://apparentdip.blogspot.com/2007/01/u-the-thermochronology.html>). In the decay chains, helium is released as alpha particles, β are beta particles, and Q is the energy released during decay.

Some basic assumptions are made when using equation 2. The first assumption is that there is secular equilibrium among all the daughter products in the decay chains. This is almost certain for all crystals that formed more than 350 thousand years before the onset of ^4He retention (Farley 2002). Secular equilibrium refers to a state where over time, the decay of the parent product to intermediary daughter product is equal to the decay of the intermediary daughter product. Another assumption made by the ingrowth equation is that there was no initial ^4He present in the crystal (Farley 2002). This assumption is generally valid because the concentration of atmospheric He is very low (5 ppm) and so trapped atmospheric He is unlikely to be significant in this calculation. Conditions that can affect He concentrations and lead to inaccurate data are fluid inclusions from the crust or mantle and the presence of inherited helium due to incomplete degassing of a grain from its previous history (Farley 2002).

Alpha particle ejection and correction

As Th and U decay, they release alpha particles which can travel different distances depending on the medium of the crystal; however it is approximately 20 μm for apatite and between 10 – 20 μm for zircon.

Depending on the size of the crystal and the stopping distance of the alpha particle, particles can either be retained, ejected or implanted (Farley, 2002; Ehlers and Farley, 2003). Retention occurs when the distance from the edge of the crystal to the parent nucleus is located more than the stopping distance away (Farley, 2002). This results in the alpha particles being retained in the crystal regardless of its magnitude. Ejection occurs when the distance between the parent isotope and the crystal edge is one stopping distance away or less. If a particle is on the edge of the crystal its

ejection probability rises to 50% (Figure 19) (Farley, 2002). Implantation is the injection of alpha particles from surrounding crystals into the crystal chosen for dating

(Ehlers and Farley, 2003). This is mostly insignificant however, because the concentration contrast between the mineral dated and the host rock is so large that implanted particles are inconsequential compared to particles produced in-situ (Farley, 2002). The only time this assumption is violated is when apatites are U-Th poor or the crystal surroundings are highly radioactive (Farley, 2002; Ehlers and Farley, 2003). If alpha ejection is not corrected for, significant errors can be introduced in (U-Th)/He ages by tens of % (Ehlers and Farley, 2003). The magnitude of alpha particles retained in a crystal is determined by the surface to volume ratio (β), the stopping distance and the distribution of parent atoms relative to the surface.

A quantitative model used for correcting He ages of long alpha stopping distances was made by Farley (2002) based on measured grains and sizes. Homogeneous spatial

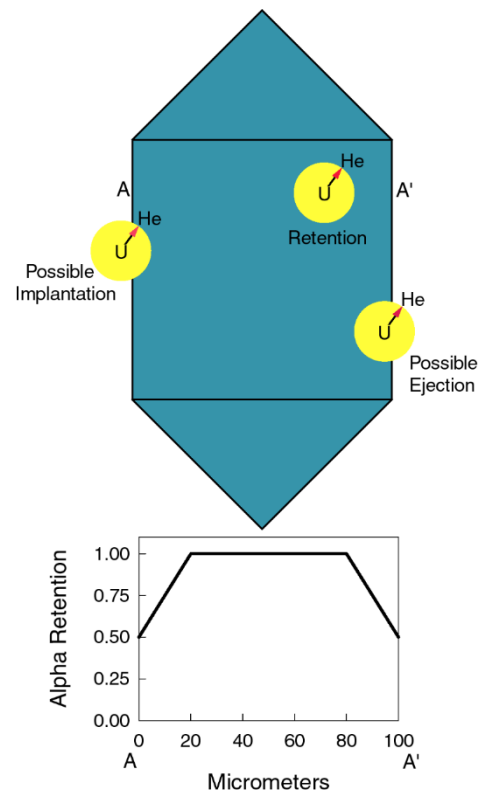


Figure 19; Possible outcomes of alpha decay in a crystal being dated and the likelihood of retention of the alpha particle. Figure from Farley (2002).

distribution of U and Th is assumed but the various effects of zonation on alpha ejection correction are discussed by Farley (1996). The model assumes a tetragonal prism with pinacoidal termination crystal morphology. The fraction of He retained is then calculated using a polynomial fit to surface area to volume ratio and the fraction of alphas retained using the following equation:

$$F_{\text{He}} = 1 + A_1\beta + A_2\beta^2 \quad \text{Equation 3}$$

A_1 and A_2 are given for different morphologies that can be seen in Table 2. The calculated F_{He} for each nuclide is then weighted corresponding to the ratio of Th/U in the sample to determine the bulk F_{He} using the following equation:

$$\text{mean}F_{\text{He}} = a_{238} {}^{238}\text{U}F_{\text{He}} + (1-a_{238}) {}^{232}\text{Th}F_{\text{He}} \quad \text{Equation 4}$$

Where a_{238} is the fraction of He derived from ${}^{238}\text{U}$ and can be found by:

$$a_{238} = (1.04 + 0.245 (\text{Th}/\text{U}))^{-1} \quad \text{Equation 5}$$

<i>Parent Nuclide</i>	<i>Tetrahedral prism with pinacoidal terminations</i>				<i>Tetrahedral prism with pyramidal terminations</i>	
	<i>(Farley 2002)</i>		<i>(Hourigan et al. 2005)</i>		<i>(Hourigan et al. 2005)</i>	
	<i>A₁</i>	<i>A₂</i>	<i>A₁</i>	<i>A₂</i>	<i>A₁</i>	<i>A₂</i>
${}^{238}\text{U}$	-4.31	4.92	-4.35	5.47	-4.28	4.37
${}^{232}\text{Th}$	-5.00	6.80	-4.94	6.88	-4.87	5.61

Table 2; Values used for A_1 and A_2 in equation 3 when calculating the fraction of He retained. Values are for zircons based on different crystal geometries. Figure from Reiners (2005).

Helium Diffusion

Helium's rapid diffusion rates, resulting in a low closure temperature, have made it a useful indicator of the time – temperature evolution of rocks. Most information of diffusional loss of helium in zircons and apatites has been done via outgassing laboratory studies (Cherniak et al., 2009). This method requires that samples are heated in a stepwise manner and the released He is measured by a mass spectrometer. Although this method has provided a lot of insight on He diffusion, it also has its limitations. The bulk releases of He in this method lacks information on the initial distribution of He in the sample (Cherniak et al., 2009). The distribution of He is controlled by the distribution of U and Th, alpha ejection from the mineral grain and differential He losses due to the past thermal history of the grain (Cherniak et al., 2009). Zonation also plays a significant role in diffusion rates with higher concentrations of U and Th near the rim resulting in higher rates of He loss by diffusion compared to homogenous distribution (Ehlers and Farley, 2003). Cooling rate also plays a significant role with grains that are rapidly cooled experiencing less diffusive loss (Ehlers and Farley, 2003). He loss in apatite below 300 °C can best be described using the Arrhenius relationship:

$$D/a^2 = D_0/a^2 e^{-E_a/RT}$$

Equation 6

Where D is diffusivity, D_0 is the diffusivity at infinite temperature, E_a is the activation energy, R is the universal gas constant ($8.314 \times 10^{-3} \text{ kJ mol}^{-1} \text{ K}^{-1}$), T is the temperature (Kelvin) and a is the diffusion domain radius (Farley 2002). If the Arrhenius relationship is obeyed it can be plotted as a straight line. The closure temperature of apatite is 60-75 °C for a cooling rate of about 10 °C / Myr (Ehlers and Farley, 2003). Zircons however, do not follow the Arrhenius equation because they have anomalously high He diffusion in the early stages of step heating (Farley 2002). This is because radiation damage promotes He loss from zircons. Radiation damage occurs in zircons at temperatures only below 250 °C meaning that if a zircon crystal has been cooler than this temperature

for up to a few hundred Myr, it should not be greatly compromised by radiation damage (Farley 2002). The Dodson equation (Equation 7) is a way to derive closure temperature which is a function of grain size, diffusion parameters, shape and cooling rate (Reiners, 2005).

$$\frac{E_a}{RT_c} = \ln \left(\frac{ART_c^2 D_0 / r^2}{E_a dT/dt} \right) \quad \text{Equation 7}$$

Where r is the effective grain size, A is a geometric factor, T_c is the closure temperature, D_0 is the frequency factor, E_a is the activation energy, R is the gas content and T is absolute temperature. For this equation to be used to calculate the closure temperature, a linear thermal history of $1/T$ is assumed (Figure 20) (Reiners, 2005).

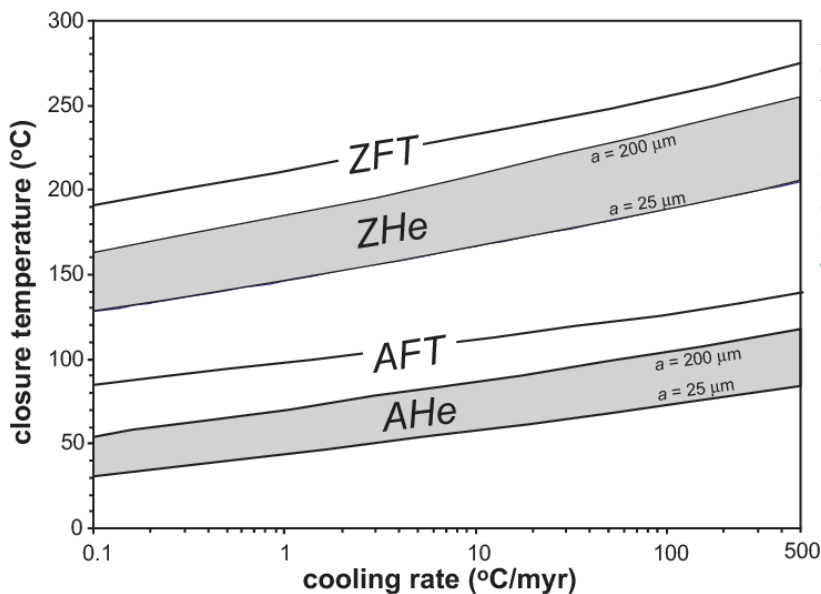


Figure 20; Closure temperatures calculated for apatite and zircon He and for apatite and zircon AFT. The parameters used for He are from Farley (2000) and Reiners et al. (2004). The closure temperatures are calculated assuming a potential variation in grain size of apatites and helium and cooling rates. The closure temperatures used for thermal modelling constraints in this study were selected from this figure. Figure from Reiners (2005).

The closure temperature signifies when daughter products which were previously diffusing out of the grain are retained. The system does not go from an open to closed system instantaneously, but instead over a gradual transition known as the partial retention zone (PRZ) (Harrison and Zeitler, 2005). The location of the PRZ will vary based on the local geological conditions and the local tectonic history. It also has

enough of a distinctive form that it can be used as an indicator in tectonic history. An example of this could be if an area had been tectonically stable for a certain duration and then experienced sudden rock uplift, a “fossil” PRZ could be identified which would give insight to the timing of initiation of the most recent tectonic phase (Harrison and Zeitler, 2005).

Age Calculation:

The He ages of the samples were calculated using the age equation which is as follows:

$$t = \frac{1}{\lambda} \ln \left(\frac{N_d}{N_p} + 1 \right) \quad \text{Equation 8}$$

Where N_d is the number of daughter atoms, N_p is the number of remaining parent atoms, λ is the decay constant (unit time⁻¹) and t is the isotopic age which is the time at which the daughter products started to accumulate (Reiners and Shuster 2009). This is an over-simplification of the age equation which in reality is much more complicated.

Results:

(U-Th)/He Results:

From the five samples selected along the transect only three samples contained apatite grains (SAR013, SAR066, SAR069) and four of the samples contained datable zircon grains (SAR013, SAR067, SAR068, SAR069).

Apatite (U-Th-Sm)/He age results:

AHe cooling ages were obtained from three of the five samples along the transect. For each sample, five single-grain aliquots were selected that met the previously discussed criteria. The method used for measurements of parent and daughter isotope was first tested on two Durango apatite standards and yielded ages of 31.96 ± 0.14 Ma and 32.10 ± 9.14 Ma. The actual age calculated by Farley (2002) of the Durango apatite is 32.1 Ma. As we obtained the same age within error margins, the instrumentation and methodology were considered calibrated. For each sample a mean corrected age was calculated as well as an error for this mean age. The error for the mean corrected age is the standard deviation of the ages of the grains in the sample. All values found for (U-Th)/He dating of apatite are presented in Table 3. Grains selected can be seen in Appendix 1.

Sample	Corrected Age (Ma)	Analytical Error (Ma)	U (ng)	Th (ng)	¹⁴⁷ Sm (ng)	[U]e	Th/U	He (nmol/g)	F _t	Raw Age (Ma)
aDUR-82	32.0	0.14	0.10	2.16	1.47	120.4	22.31	21.5	1.00	31.97
aDUR-83	32.1	0.14	0.06	1.22	0.91	69.6	19.47	12.4	1.00	32.06
aSAR013-1	105.1	0.44	0.01	0.01	0.37	2.7	1.00	1.3	0.77	80.65
aSAR013-2	119.0	0.57	0.02	0.01	0.32	3.5	0.23	1.8	0.77	91.89
aSAR013-3	152.4	0.75	0.03	0.00	0.22	2.9	0.09	2.0	0.79	120.20
aSAR013-4	99.1	0.49	0.01	0.00	0.31	2.4	0.25	1.0	0.76	75.42
aSAR013-5	168.2	0.83	0.03	0.00	0.35	3.8	0.08	2.9	0.79	132.06
aSAR066-1	300.3	1.50	0.03	0.00	0.75	6.7	0.03	9.0	0.76	227.41
aSAR066-2	174.9	0.76	0.02	0.02	0.93	7.6	0.74	5.8	0.73	127.04
aSAR066-3	402.3	1.91	0.04	0.01	0.13	18.4	0.24	28.6	0.69	277.72
aSAR066-4	157.7	0.70	0.03	0.02	0.57	5.4	0.59	3.8	0.78	122.96
aSAR066-5	184.0	0.91	0.09	0.01	0.81	11.3	0.06	9.2	0.79	144.69
aSAR069-1	220.2	1.09	0.21	0.01	3.70	16.4	0.06	17.0	0.82	180.29
aSAR069-2	122.1	0.61	0.06	0.00	2.61	7.4	0.04	4.4	0.81	98.58
aSAR069-3	697.9	3.15	0.08	0.04	1.76	9.2	0.48	30.5	0.79	550.68
aSAR069-4	121.9	0.61	0.08	0.00	1.82	9.4	0.00	5.2	0.79	96.13
aSAR069-5	185.1	0.88	0.08	0.02	0.60	24.0	0.23	18.0	0.73	134.68

Table 3: Reduced data from Apatite (U-Th)/He dating. [U]e is the effective uranium content and represents the amount of U needed to produce the measured concentrations of He present in the grain if U was the sole parent isotope. F_t is the alpha ejection correction that is used to calculate the corrected age. Raw age is calculated using parent and daughter isotope concentrations without taking alpha ejection into consideration.

Sample SAR013

The mean corrected age for the selected aliquots of this sample is 129.7 ± 30.21 (SAR013). Single-grain ages range from 99.1 ± 0.49 Ma (SAR013 -4) to 168.2 ± 0.83

Ma (SAR013-5). The calculated ages can be grouped into two ranges of similar values with the younger range being $99.1 \pm 0.49 - 119.0 \pm 0.57$ Ma (SAR013-1,2,4) and the older range from $152.4 \pm 0.75 - 168.2 \pm 0.83$ Ma (SAR013-3,5) (Figure 21a).

Sample SAR066

The corrected ages of the five grains selected and dated within this sample yielded a mean age of 243.9 ± 104.9 Ma. Aliquot ages ranged from 157.7 ± 0.7 Ma (SAR013-4) to 402.3 ± 1.9 Ma (SAR013-3) (Figure 21a). Three of the grains have similar ages (SAR013-2,4,5) ranging from 157.7 ± 0.7 Ma to 184.0 ± 0.9 Ma (mean age: 172.2 ± 13.3 Ma). The remaining two grains (SAR066-1, 3) have much older ages of 300.3 ± 1.5 Ma and 402.3 ± 1.9 Ma (mean age: 351.3 ± 72.1 Ma).

Sample SAR069

For sample SAR069, five apatite aliquots yielded a mean age of 269.5 ± 243.2 Ma. There is one outlier within the sample of age 697.9 ± 3.2 Ma (SAR069-3) (Figure 21a). When discarded, the calculated mean of corrected ages is much younger at 162.4 ± 48.7 Ma. SAR069-3 seems to show zonation and potentially contained an inclusion. It also had significantly higher Th concentrations compared to the other grains.

Zircon (U-Th)/He Age Results:

Four samples were used for (U-Th)/He dating of zircons and five single-crystal aliquots were selected per sample. The calibration of the instruments used for dating was tested using zircons of known age from the Fish Canyon Tuff. Ages of 29.84 ± 0.14 Ma and 30.91 ± 0.14 Ma were obtained from zFCT-59 and zFCT-60, respectively. These values fall within the margin of error for the actual ZHe age which is 28.2 Ma so the method and instrumentation is considered calibrated. (U-Th)/He results for zircons are in Table 4. Dated zircon grains can be seen in Appendix 2.

Sample	Corrected Age (Ma)	Analytical Error (Ma0)	U (ng)	Th (ng)	¹⁴⁷ Sm (ng)	[U]e	Th/U	He (nmol/g)	Ft	Raw Age (Ma)
zFCT-59	29.84	0.14	2.45	1.10	0.03	307.7	0.45	39.7	0.80	23.84
zFCT-60	30.91	0.14	2.54	1.19	0.00	293.1	0.47	39.0	0.80	24.61
zSAR013-1	1176.06	5.59	1.35	0.31	0.00	112.8	0.23	650.4	0.81	952.24
zSAR013-2	667.58	3.19	2.82	0.62	0.07	192.1	0.22	602.4	0.82	548.98
zSAR013-3	77.49	0.39	9.94	0.11	0.06	607.5	0.01	213.1	0.84	64.74
zSAR013-4	285.78	1.41	2.91	0.14	0.00	411.6	0.05	503.0	0.78	222.05
zSAR013-5	179.39	0.89	6.26	0.14	0.00	587.2	0.02	464.3	0.81	144.81
zSAR067-1	970.42	4.20	1.94	1.42	0.03	119.9	0.73	560.9	0.82	795.95
zSAR067-2	1073.47	4.40	0.23	0.25	0.04	19.8	1.08	104.1	0.82	884.25
zSAR067-3	986.78	4.10	0.78	0.75	0.00	66.5	0.96	310.4	0.81	795.18
zSAR067-4	1162.67	4.68	0.37	0.46	0.00	27.7	1.24	159.7	0.83	963.03
zSAR067-5	1116.57	4.54	0.54	0.61	0.04	18.5	1.14	106.9	0.87	966.02
zSAR068-1	923.72	4.35	1.62	0.44	0.06	180.9	0.27	785.5	0.80	741.21
zSAR068-2	953.34	4.53	1.51	0.33	0.11	259.8	0.22	1120.5	0.77	736.36
zSAR068-3	702.51	3.42	1.62	0.21	0.00	227.6	0.13	724.3	0.79	556.45
zSAR068-4	880.39	4.16	1.30	0.32	0.05	261.3	0.25	1003.1	0.75	662.26
zSAR068-5	889.11	4.16	2.14	0.63	0.06	290.2	0.30	1171.0	0.78	693.62
zSAR069-1	705.98	3.45	2.01	0.20	0.00	358.5	0.10	1130.0	0.78	551.35
zSAR069-2	1050.89	5.00	3.04	0.66	0.00	327.0	0.22	1662.7	0.81	853.17
zSAR069-3	713.40	3.47	3.16	0.38	0.01	200.0	0.12	685.1	0.84	595.88
zSAR069-4	599.37	2.80	2.27	0.68	0.00	262.6	0.30	719.7	0.81	483.66
zSAR069-5	332.22	1.60	4.00	0.68	0.00	346.8	0.17	524.4	0.82	273.10

Table 4. (U0-Th)/He zircon results. U, Th, and Sm concentrations are presented in nanograms (ng); Th/U represents the ratio of the two parent isotopes; [U]e is the effective uranium content and represents the amount of U needed to produce the measured concentrations of He present in the grain if U was the sole parent isotope. F_1 is the alpha ejection correction that is used to calculate the corrected age.

Sample SAR013

The five aliquots for this sample yielded mean corrected ages of 477.26 ± 449.93 Ma. There was no clear trend in age, with a scatter of ages ranging from 77.49 ± 0.39 Ma (SAR013-3) to 1176.06 ± 5.59 Ma (SAR013-1) (Figure 21b). Higher Th/U ratios were found in samples that provided significantly older ages. The sample did not have abundant zircons to select from and therefore there was limited choice in selecting the final grains for dating.

Sample SAR067

For sample SAR067, mean corrected ages calculated were 1061.98 ± 82.56 Ma. The ages of the different aliquots display low dispersion and are highly consistent ranging from 970.42 ± 4.20 Ma (SAR067-1) to 1162.67 ± 4.68 Ma (SAR067-4) (Figure 121b).

Sample SAR068

Mean corrected ages for the five aliquots dated for sample SAR068 yielded an age of 869.81 ± 97.92 Ma. Grain ages varied from 702.51 ± 3.42 Ma (SAR068-3) to 953.34 ± 4.53 Ma (SAR068-2). The grain dated to 702.51 ± 3.42 Ma (SAR068-3) might be considered as an outlier with an offset of 177.88 Ma from the next youngest grain (Figure 21b). Remaining grains all lie within a range of 72.9 Myr of each other.

Sample SAR069

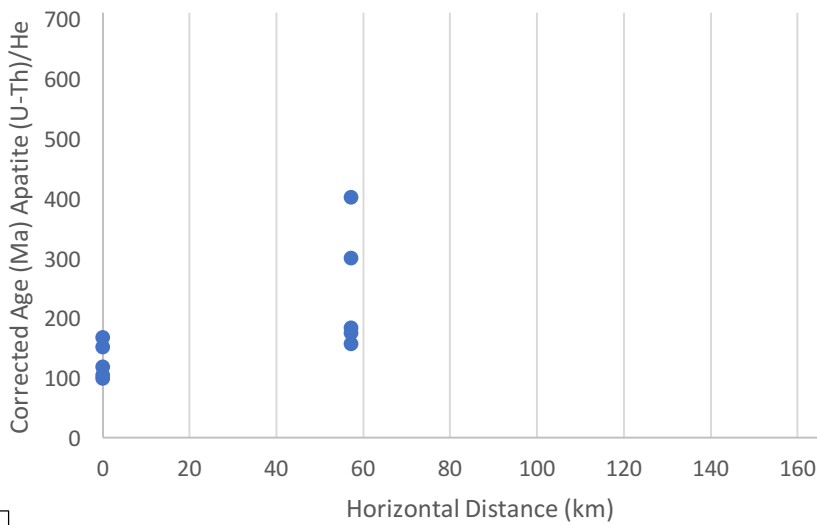
Five aliquots were selected and dated yielding a mean corrected age of 680.37 ± 258.26 Ma. The grains dated in the sample showed significant scatter (Figure 21b). Three grains show similar ages of 599.37 ± 2.80 Ma (SAR069-4), 705.98 ± 3.45 Ma (SAR069-1) and 713.40 ± 3.47 Ma (SAR069-3) and their mean corrected age is 672.92 ± 63.80 Ma is found. This value does not differ significantly from the mean corrected age calculated taking into account all grains dated for this sample. Grain SAR069-5 can most likely be considered an outlier with an age of 332.22 ± 1.60 Ma with significantly higher U concentration compared to the other grains in this sample. Additionally, SAR069-2 is an outlier of this sample yielding an age of 1050.89 ± 5.00 Ma.

Interpretation of Results:

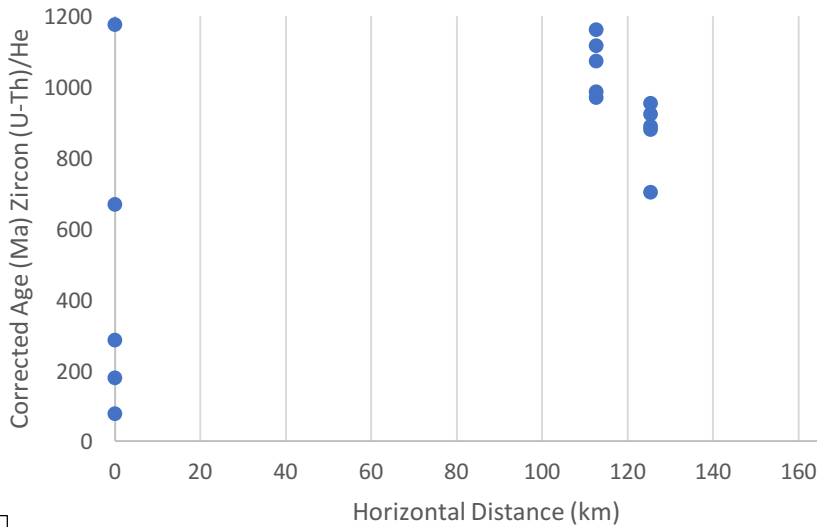
Age Trend along the Transect:

To get an understanding of the relationship between age and distance along the transect, the calculated corrected AHe and ZHe ages were plotted against horizontal distance (Figure 21). Each sample's horizontal distance is described in terms of the distance, in km, from the southernmost sample, sample SAR013. The plots help determine any obvious outliers within the dataset. These outliers will most likely be disregarded during thermal modelling due to the limitations of the model which will be discussed later.

The age versus time plots can also give insight of any spatial trends that occur along the transect. Figure 21a does not show clear any spatial trends along the strike of the margin of apatite ages. Figure 21b may show a spatial trend along the margin of younger zircon ages as you move progressively more north if sample SAR013 is not regarded.



a



b

Figure 21; Horizontal distance versus corrected age of dated grain. Horizontal distances are: SAR013: 0 km, SAR066: 57.23 km, SAR067: 112.63 km, SAR068: 125.42 km, SAR069: 173.5 km.

Age versus Effective Uranium:

Apatite:

Plotting the effective uranium (eU) content against corrected age can provide insight on the expected thermal history of the measured data and assist in creating constraints during modelling. Samples that experienced a common (t-T) history can be plotted on the same graph to show the relative extent of radiation damage (Guenther et al. 2013). As previously described, the diffusion rates of both apatites and zircons are very

sensitive to radiation damage, and grains with higher eU will have been subjected to greater radiation damage.

In apatite, He diffusivity decreases with increasing radiation damage in the grains. This is because isolated sites of radiation damage decrease the rate of helium mobility by “trapping” He atoms (Figure 22) (Shuster et al. 2006). Sites of radiation damage can create small differences in the crystal that generate enough space for ^4He atoms to accumulate. He atoms will accumulate here as it requires less energy than to continue to diffuse out of the crystal lattice. As long as this is the case, He atoms will remain trapped within this void until they have acquired enough energy to overcome the energy barrier (E_t) needed to exit this space and re-enter the crystal lattice.

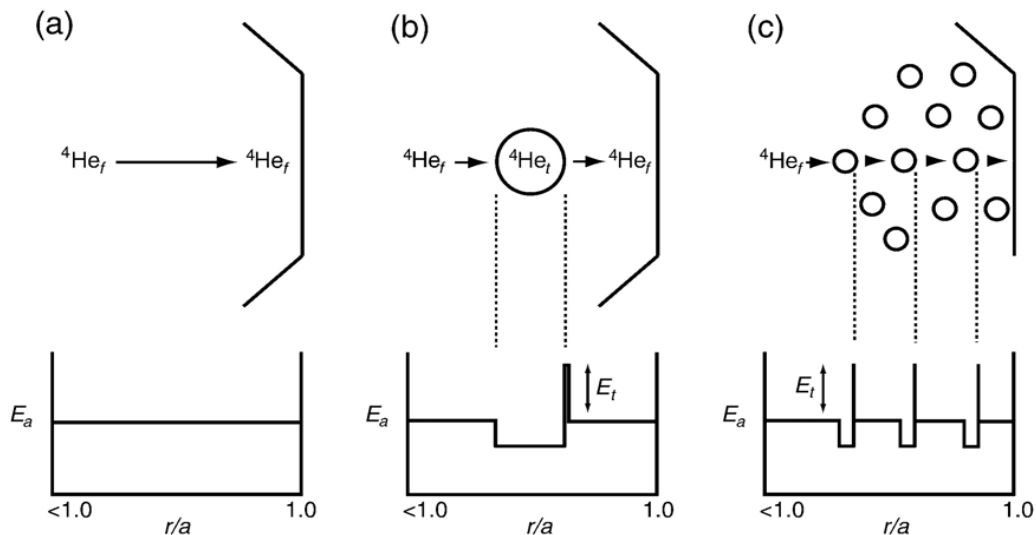


Figure 22; Schematic model created by Shuster et al. (2006) showing the effect of radiation damage sites on He diffusion. (a) The diffusion of a He atom without any radiation damage in the grain, effective activation energy (E_a) remains linear throughout. E_a is plotted as a function of radial position (r) where a is the radius of the sphere. The surface of the grain is represented by $r/a = 1$. (b) Radiation damage present along the pathway of He atom across the same distance. The damaged area is represented by the circle. (c) represents an increased accumulation of damaged areas. For (b) and (c), $^4\text{He}_t$ represents trapped He atoms and $^4\text{He}_f$ represents free He atoms. E_a is the activation energy needed for a He atom to diffuse out of the crystal without radiation damage. E_t is the energy needed for a He atom to move out of a trapped surface.

Since radiation damage increases over time, an increase in He retentivity is also expected over time. He retentivity can be shown by eU concentrations where

decreasing He diffusion, due to radiation damage, will result in a positive correlation between the age of the grain and the effective uranium content. This means that as the age of the grain increases, its eU will also increase due to decreased rates of diffusion that are caused by increased radiation damage.

Flowers (2009) tested the effects of reheating on partial He loss of apatite. Reheating was done with different peak temperatures where temperatures below ~ 30 °C did not induce He loss from apatite grains due to an inadequate amount of heat (Flowers 2009). However, when grains are reheated to temperatures between $\sim 30 - 100$ °C, the model showed highly variable dates that created positive eU correlation (Flowers 2009). A positive correlation is created (Figure 23) because apatites with the lowest eU and least radiation damage will lose most of their He during reheating, producing the youngest ages (Flowers 2009). Helium will be effectively lost in grains with little radiation damage as atoms are not trapped in damage sites. Grains with increasing eU, will have increased He retentivity resulting in a decrease of He loss at the peak reheating temperature (Flowers 2009). Reheating will have little effect on He loss in grains with the highest eU concentrations thus yielding the oldest ages.

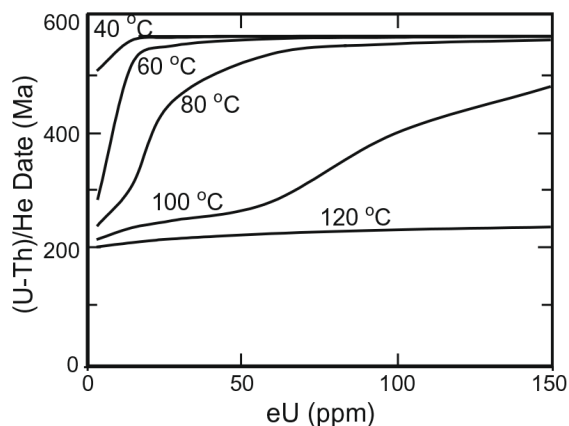


Figure 23; (U-Th)/He ages versus effective uranium concentration. Solid lines show different peak reheating temperatures at 40, 60, 80, 100 and 120 °C. Figure from Flowers (2009).

The apatite grains dated for this study were plotted together and produced a positive correlation of corrected age versus effective uranium content (Figure 24). This suggests, based on the previously described scenario by Flowers (2009), that reheating resulting in partial He loss in apatite suites may have occurred in our study area.

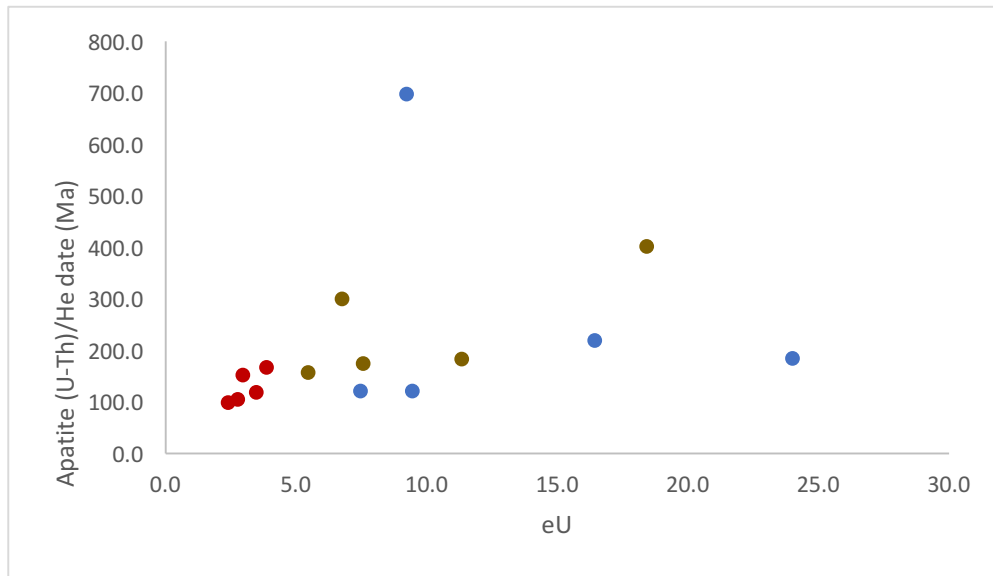


Figure 24; Corrected age of apatites vs. the effective uranium content. Coloring of markers shows sample; Red- SAR013, Brown- SAR066, Blue- SAR069. There is a positive correlation as age increases, the effective uranium content also increases.

Zircon:

In zircons, He diffusivity increases with increasing radiation damage to a point, beyond which He diffusivity decreases significantly. This results in grains having much lower ages. Models made by Guenther et al. (2013) show how t-T paths vary as a result of effective uranium content over time

Similarly to apatite, if all the zircon grains within a sample were to undergo a reheating event, grains with different amounts of radiation damage will be reset to varying degrees also resulting in a positive correlation (Guenther et al. 2013). Positive correlation between grain ages and eU can also be seen in scenarios of slow, monotonic cooling (Figure 25A). Both scenarios show that when grains with already accumulated radiation damage and a range of eU concentrations inhabit the PRZ, a positive correlation will result (Guenther et al. 2013). A decrease in He diffusivity however is not the result of traps in zircons but is instead the result of preferred pathways of the He atom as it

diffuses out of the grain. According to Guenther et al. (2013), disruption of the pathways by radiation damage would result in a decrease in He diffusivity.

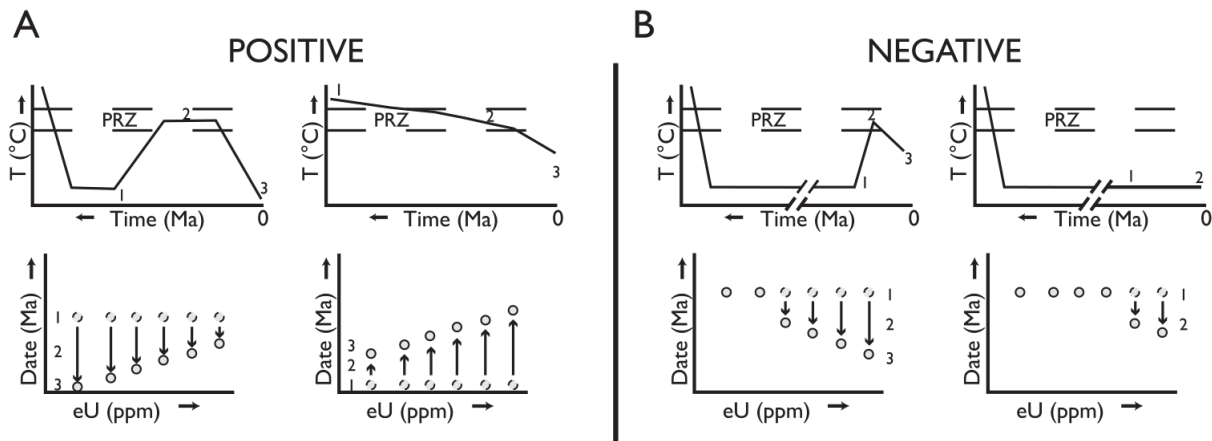


Figure 25; A schematic diagram of time- temperature graphs that can produce the associated eU - age relationship. A) if a sample has low radiation damage and experiences a thermal pulse or if it passes through the PRZ slowly enough for damage in growth and diffusion to occur at the same time, a positive correlation will form. B) Grains with high radiation damage, exposed to a thermal pulse will result in negative eU correlations. A negative correlation can also occur if the grains remain at low temperatures for a long time resulting in significant He loss. Arrows show the direction in which the values increase. Figure from Guenther et al. (2013).

To produce negative correlation pathways, zircon grains must reach a threshold of radiation damage after which He diffusivities will increase abruptly. Above this threshold damage zones within the grain will begin to connect to form channels in the lattice creating pathways that allow for rapid diffusion of He (Guenther et al. 2013, Reiners 2005). For this threshold to be reached, zircon grains must be exposed to long term radiation damage at low enough temperatures to prevent annealing. Annealing can occur from He loss and short-term resetting due to exhumation to the surface or via a brief, low temperature reheating event causing resetting (Guenther et al. 2013).

Zircon age versus eU concentration plots (Figure 26) show a negative correlation which suggests that the grains contained a lot of radiation damage. However, it is not clear from the plot whether the negative correlation is a result of a thermal pulse or of the grains remaining at low temperatures causing significant He loss.

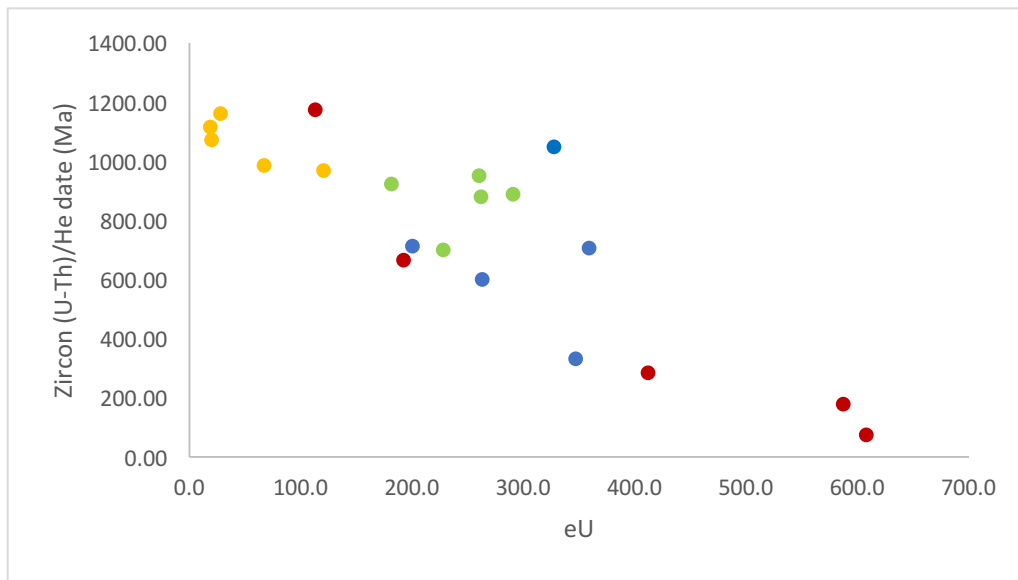


Figure 26; Corrected age of Zircons vs. the effective uranium content. Coloring of markers shows sample location; Red- SAR013, Brown- SAR066, Blue- SAR069. There is a negative correlation as age decreases, the effective uranium concentration will increase.

Consideration of the eU vs age plots prior to modelling will provide insight to possible constraints that should be applied or at least tested.

Thermal modelling:

HeFTy:

HeFTy is a modelling software that uses the theoretical understanding of how thermochronometers behave to explore the range of possible time—temperature (t-T) histories of the measured data. Due to the loss of He via diffusion and alpha particle ejection, modelling of the (U-Th)/He system requires the following parameters; diffusion calibration, and dimension (sphere of a given radius), the type of alpha correction and zoning in parent isotopes (if known) (Ketcham 2005). HeFTy is able to produce two different types of models; forward and inverse. An inverse model, which is the model used in this study, is used to create a range of thermal histories that lie within a statistical criterion and are consistent with measured data (Ketcham 2005). The model allows us to predict how the system may have evolved over time and temperature. Output varies based on the geological problem being solved and the thermochronologic data (Ketcham 2005).

To increase the accuracy of results, prior to modeling data should be evaluated and the following specifications should be taken into consideration. First, the model must begin at sufficiently high temperatures to ensure that at initial conditions there is no retained He. To ensure this, the earliest constraint for the t-T path should be considerably above the closure temperature of He in zircon, which is the most retentive thermochronometer being used in this study (Ketcham 2005). The constraint will be created using a user-defined box that will surround a section of time-temperature space. The second constraint will be the present-day temperature at which the sample was collected at. A path will then be created via line segments from sample collection temperature to the constraint boxes. The line segment can either be straight or broken down into sub—segments allowing for greater variability in the model. This has been defined as allowed complexity and is used because the t-T history of the sample is not known (Ketcham 2005). In the case of this study, lines were broken into sub—segments for added complexity because the goal was to create a range of thermal histories that were statistically consistent.

The method used to statistically compare the model predictions to the measured data is Goodness of Fit (GOF) (Ketcham 2005). When the minimum is > 0.05 the model is deemed acceptable (passes 95% confidence test) and when the minimum is > 0.5 the model is considered good (statistical precision limit) (Ketcham 2005). These paths will be represented in green for acceptable and pink for good. HeFTy uses two different approaches to test the adequacy of the different paths, the Monte Carlo approach and the optimization algorithm. The approach used for this study was the Monte Carlo approach which creates time – temperature paths that are independent to one another and evaluates them.

This modelling system cannot produce an exact t-T path for cooling due to limited precision in measurements, an absence of system uniqueness and informational loss (Ketcham 2005). Other limitations of the model include that more than seven aliquots cannot be entered into single model runs consequently grains must be empirically selected for modelling and the remaining will be disregarded. As grains must be selected, outliers will be the first grains disregarded for modelling. To produce the most

accurate models, geological history should be taken into consideration to input additional constraints for the thermal history of the sample.

Setup of the models:

Eight inverse thermal models were run using the HeFTy software with the collected data. Samples SAR069 and SAR013 were the only samples that contained both dated apatite and zircon grains. The remaining three samples, SAR066, SAR067 and SAR068, contained only apatite or zircon grains. Therefore, those three samples were grouped based on their geographic locations. The apatite grains of sample SAR066 were grouped with the zircon grains of sample SAR067. The apatite grains of sample SAR069 were grouped with the zircon grains of sample SAR068. Two different thermal scenarios were tested for each sample where: 1) the samples experienced cooling only and 2) the samples were cooled above the AHe PRZ with the potential to be re-heated during rifting or post-rift burial.

The constraints used in the first scenario (referred to as Model 1 in the rest of the text) are as follows (Table 5): (1) The first constraint is at 160-200 °C between 1250-700 Ma; in timing, it covers the age range of the selected zircons single-grain ages for all the samples and in temperature, it covers the ZHe PRZ to up to 200 °C, a temperature sufficiently high ensuring that at initial conditions there was no retained He (see Reiners, 2005; base of the PRZ for grains of 200 µm and cooling rates of 10 °C/Ma is about 200 °C) (2) the next constraint placed on both models was at 40-200 °C at 50-250 Ma. The upper temperature limit of this constraint reflects the upper limits of the partial retention zone of an apatite crystal. The lower limit does not reflect the lower limit of the PRZ of apatites but was placed at this value because in sample SAR013, zircons were dated at 222.05 and 144.81 Ma so this temperature limit was set to accommodate these grains. The upper age limit selected for apatites reflects the range in age of the measured grains. However, it also reflects the oldest age of magmatism (222.7 ± 0.3 Ma) found in a Greenland dyke attributed to rifting according to Larsen et al. (2009). The dated dykes provide a convincing constraint on the beginning of significant extension in the north Atlantic plate and therefore a logical constraint for models in which we are

trying to detect a rifting signal. (3) The last constraint that was applied to both models was the present-day temperature at which the sample was collected. The mean annual temperature in Hopedale ranges between -4 and -1 °C

(https://www.canal.gov.nl.ca/reports/Water_Resources_Atlas/Water_Resources_Atlas_of_Newfoundland_1992_02_CLIMATE.pdf) and therefore the lowest temperature available in the software was selected which is 0 °C.

For the second thermal scenario that we have tested (referred to as Model 2 in the rest of the text), we have used the same constraints applied to Model 1 and added a fourth constraint. The fourth constraint was placed at 20-160 °C between 300-700 Ma (Table 5). The idea was to focus the Monte Carlo search on a path in which the rock would have been exhumed close to the surface “early” in its thermal history and would have stayed there for a long period of time, before being potentially reheated (third constraint) syn-post rifting. Using a Monte Carlo random search, each model run had 10 000 iterations with monotonic variable path segments and three half-segments evenly spaced between each constraint (3lv).

This modeling strategy was based on geological evidences and on our thermochronological results. The possibility of a very slow cooling to thermal stagnation followed by post 250 Ma reheating event was hypothesized based on our results when plotting ZHe and AHe apparent ages against effective uranium content for all our samples (Figure 24, 25). The ZHe plot shows a clear negative correlation which could be indicative of the above-mentioned thermal history. Furthermore, the large difference in ages between zircon and apatite grains could suggest that there was either very slow monotonic cooling between the closure temperatures of the two systems or that there was a reheating event that only reset AHe grains (Hansen & Reiners, 2006). Lastly, the ages of the apatite grains measured in this study broadly coincide with the rifting event of the Labrador Sea so the presence of a thermal pulse due to this event is a reasonable hypothesis.

Sample (s)	(a, z)SAR013	(a, z)SAR013	aSAR066, zSAR067	aSAR066, zSAR067	aSAR069, zSAR068	aSAR069, zSAR068	(a, z)SAR069	(a, z)SAR069
Constraint 1 (ZHe)	700-1250 Ma 200 -160 °C	700-1250 Ma 200 -160 °C	700-1250 Ma 200 -160 °C	700-1250 Ma 200 -160 °C	700-1250 Ma 200 -160 °C	700-1250 Ma 200 -160 °C	700-1250 Ma 200 -160 °C	700-1250 Ma 200 -160 °C
Constraint 2	N/a	300-700 Ma 20- 160 °C	N/a	300-700 Ma 20- 160 °C	N/a	300-700 Ma 20- 160 °C	N/a	300-700 Ma 20- 160 °C
Constraint 3 (AHe)	50-250 Ma 40-200 °C	50-250 Ma 40-200 °C	50-250 Ma 40-200 °C	50-250 Ma 40-200 °C	50-250 Ma 40-200 °C	50-250 Ma 40-200 °C	50-250 Ma 40-200 °C	50-250 Ma 40-200 °C
Constrain 4	Present 0 °C	Present 0 °C	Present 0 °C	Present 0 °C	Present 0 °C	Present 0 °C	Present 0 °C	Present 0 °C
Selected Grains	a: 1 ,2 ,3 ,4 z: 4, 5	a: 1 ,2 ,3 ,4 z: 4, 5	a: 2, 4, 5 z: 2, 4, 5	a: 2, 4, 5 z: 2, 4 ,5	a: 2, 4, 5 z: 1, 2, 5	a: 2, 4, 5 z: 1, 2, 5	a: 2, 4, 5 z: 1, 3, 4	a: 2, 4, 5 z: 1, 3, 4
Paths	10000	10000	10000	10000	10000	10000	10000	10000
Acceptable fits	221	154	239	437	267	469	735	854
Good fits	0	0	25	71	19	40	324	434

Table 5; Thermal model parameters and results. a= apatite, z= zircon

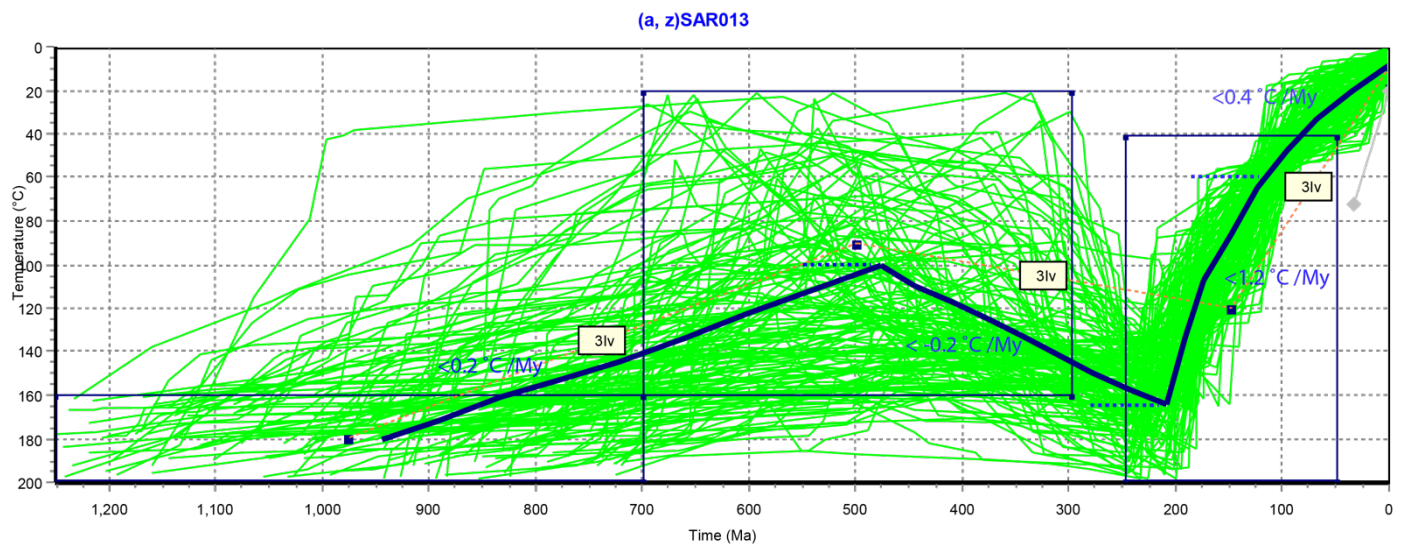
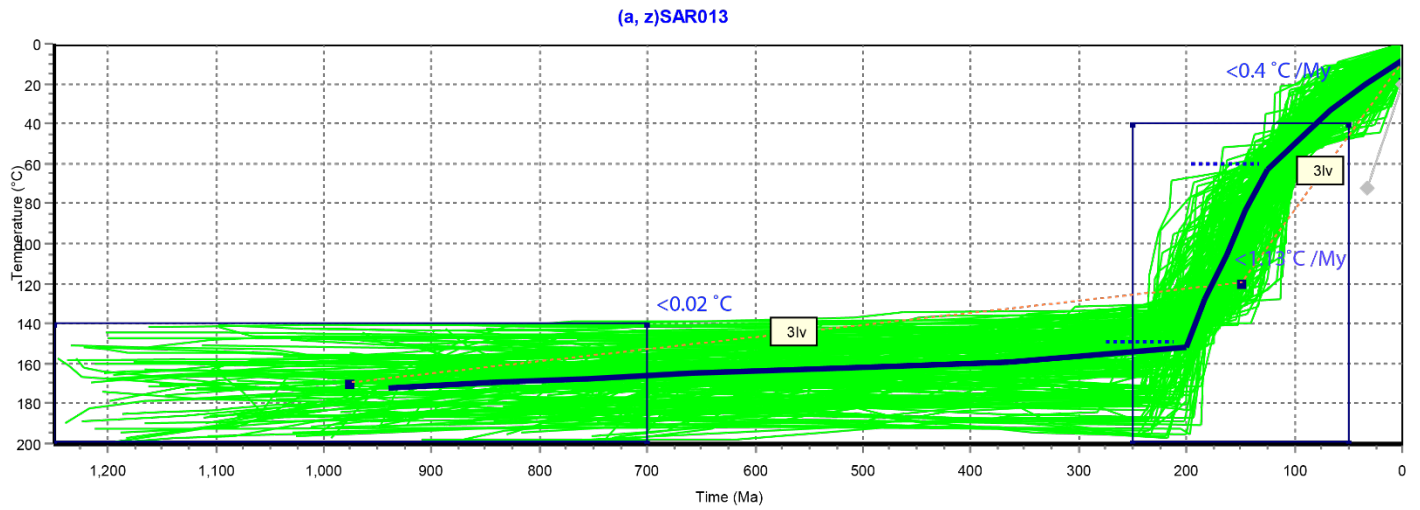


Figure 27; Representative HeFTy inversion model for (a, z)SAR013. For AHe and ZHe data, radiation damage models from Flowers et al. (2009) and Guenther et al. (2013) respectively, were used. Using a Monte Carlo random search, each model run had 10 000 iterations with monotonic variable path segments and three half-segments evenly spaced between each constraint (3lv). Top model is model 1 with three constraints and bottom model is model 2 with four constraints. Pink lines show good fits, green lines show acceptable fits and the black line is the weighted mean path. For number of acceptable and good paths refer to Table 5.

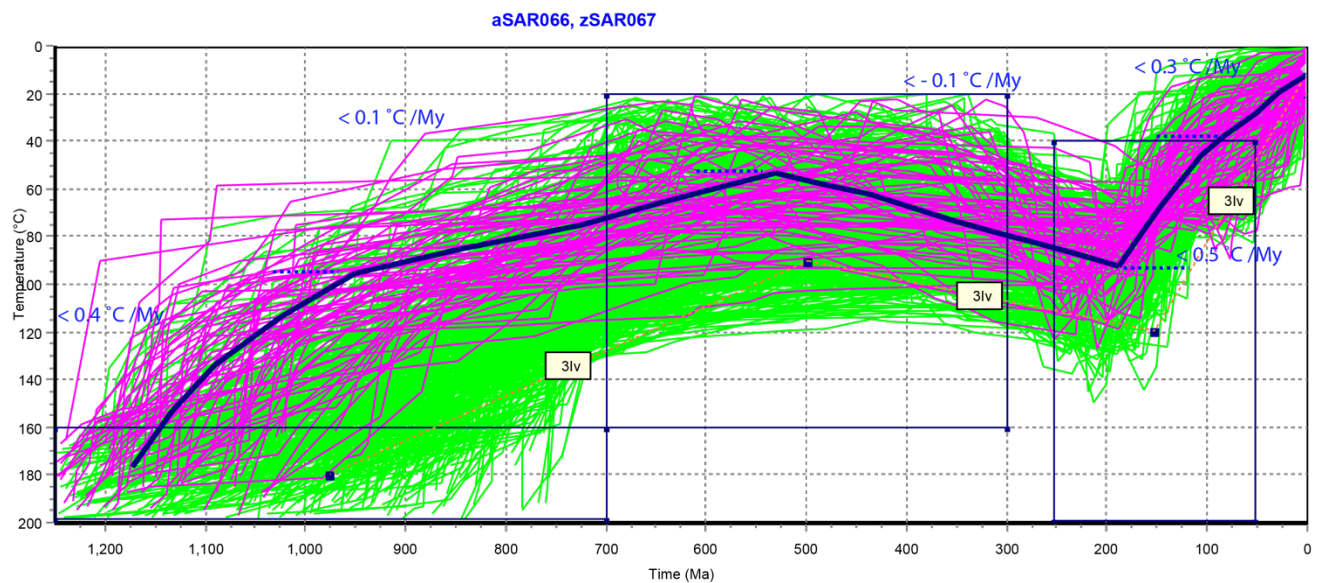
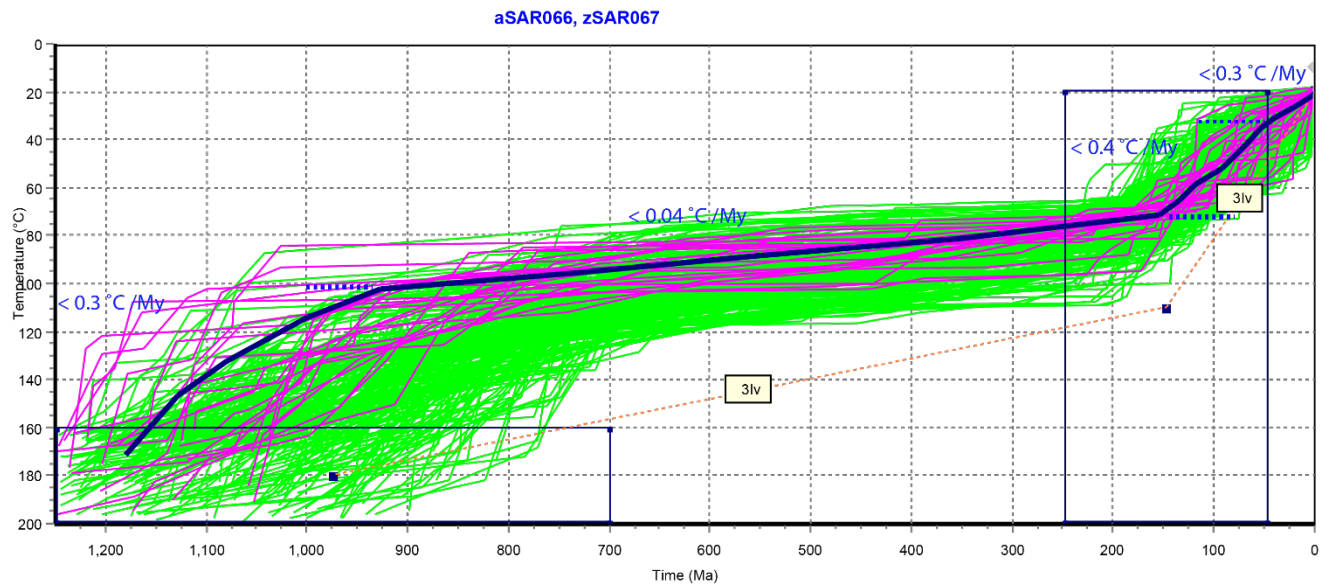


Figure 28; Representative HeFTy inversion model for aSAR066, zSAR067. For AHe and ZHe data, radiation damage models from Flowers *et al.* (2009) and Guenther *et al.* (2013) respectively, were used. Using a Monte Carlo random search, each model run had 10 000 iterations with monotonic variable path segments and three half-segments evenly spaced between each constraint (3lv). Top model is model 1 with three constraints and bottom model is model 2 with four constraints. Pink lines show good fits, green lines show acceptable fits and the black line is the weighted mean path. For number of acceptable and good paths refer to Table 5.

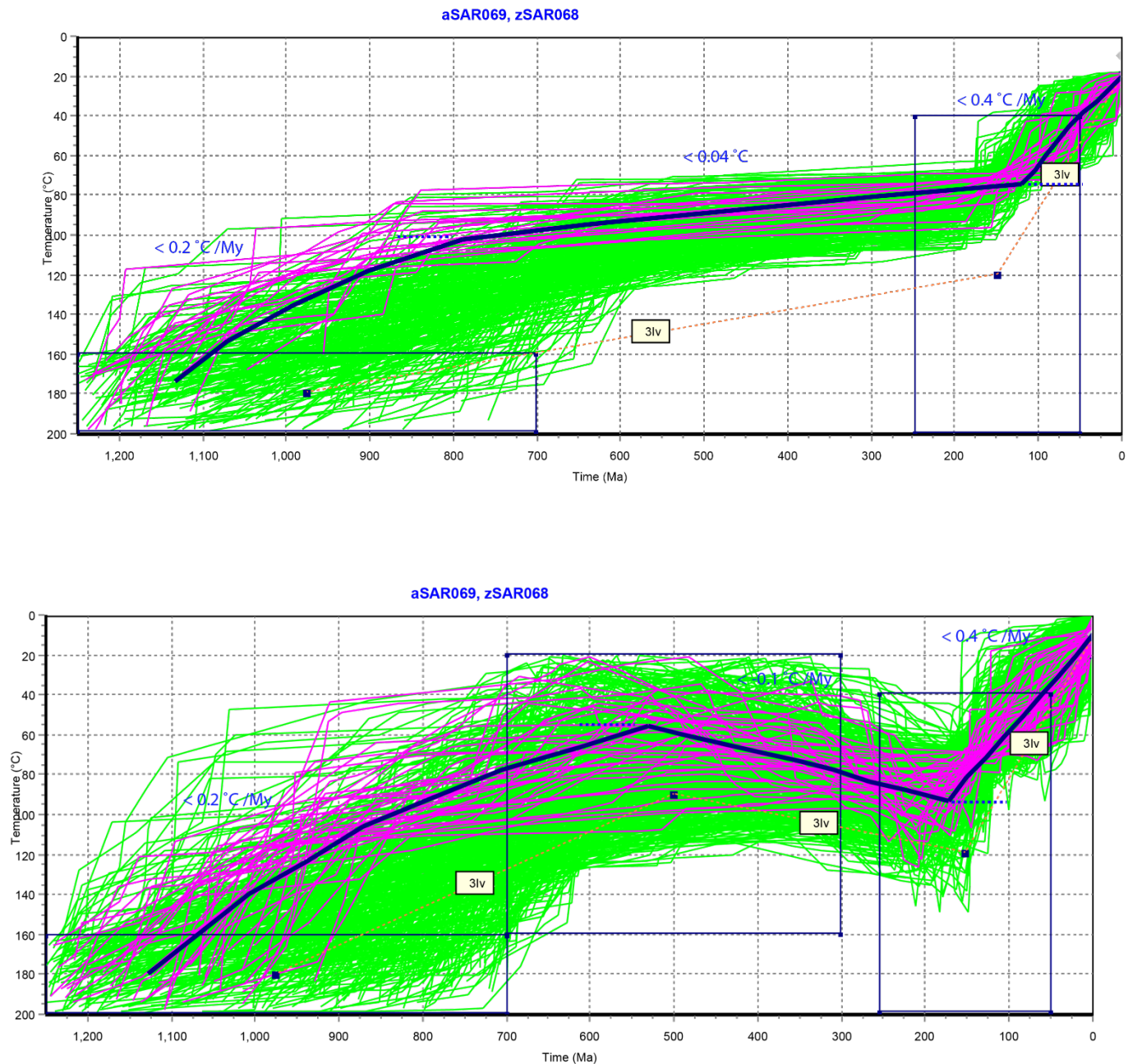


Figure 29; Representative HeFTy inversion model for aSAR069, zSAR068. For AHe and ZHe data, radiation damage models from Flowers et al. (2009) and Guenther et al. (2013) respectively, were used. Using a Monte Carlo random search, each model run had 10 000 iterations with monotonic variable path segments and three half-segments evenly spaced between each constraint (3lv). Top model is model 1 with three constraints and bottom model is model 2 with four constraints. Pink lines show good fits, green lines show acceptable fits and the black line is the weighted mean path. For number of acceptable and good paths refer to Table 5.

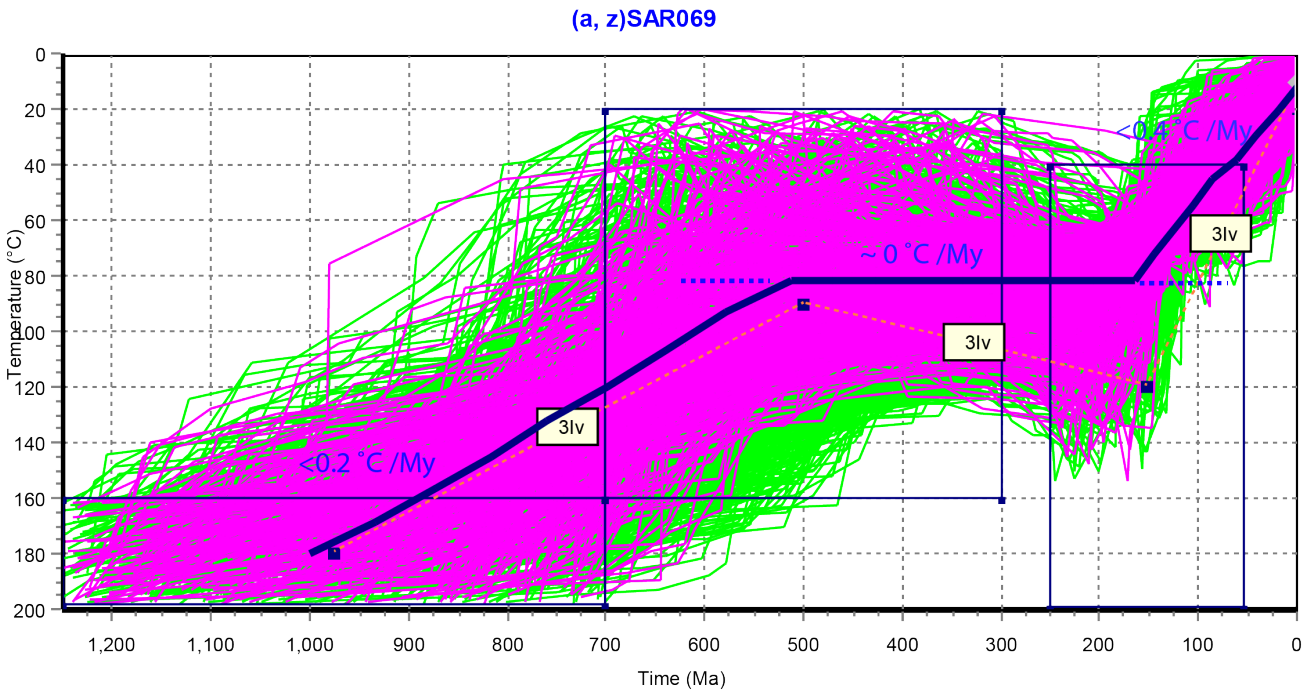
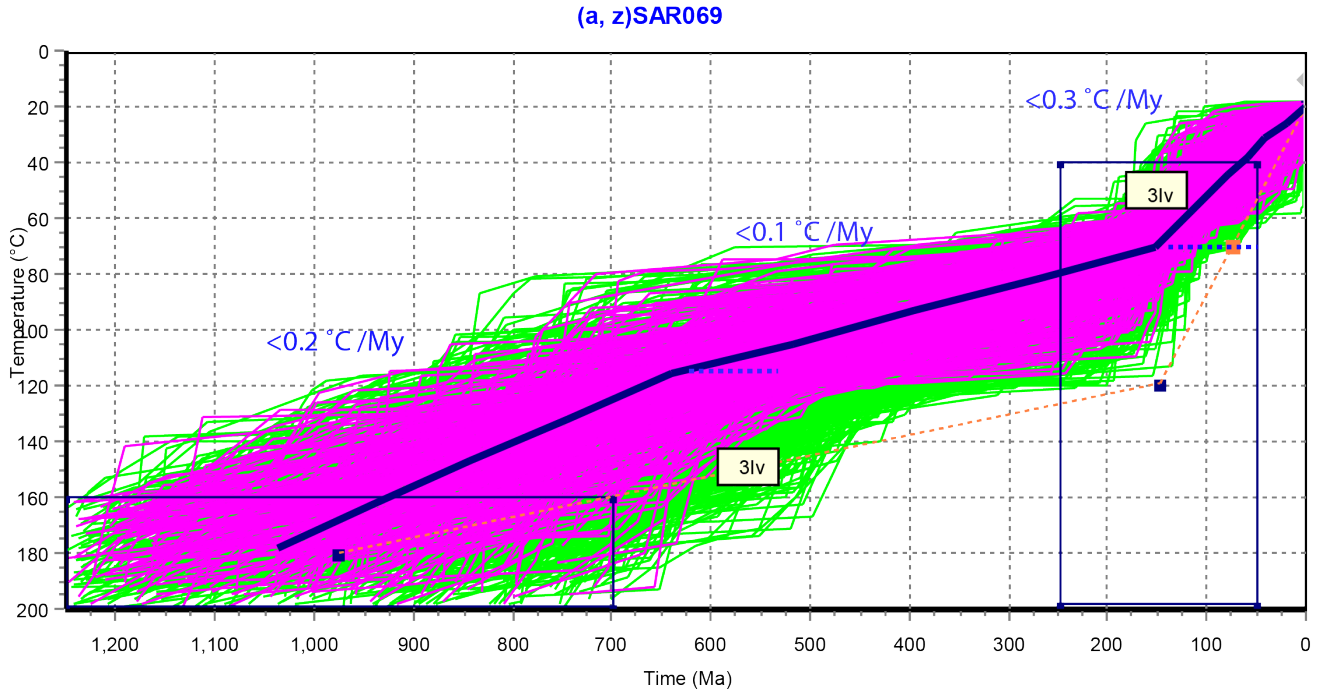


Figure 30; Representative HeFTy inversion model for (a, z)SAR069. For AHe and ZHe data, radiation damage models from Flowers et al. (2009) and Guenther et al. (2013) respectively, were used. Using a Monte Carlo random search, each model run had 10 000 iterations with monotonic variable path segments and three half-segments evenly spaced between each constraint (3lv). Top model is model 1 with three constraints and bottom model is model 2 with four constraints. Pink lines show good fits, green lines show acceptable fits and the black line is the weighted mean path. For number of acceptable and good paths refer to Table 5.

Modelling Result Descriptions:

Model 1:

(a, z)SAR013: This model produced 221 acceptable paths and 0 good paths.

In this model, cooling began at ~950 Ma and 170 °C. The initial cooling rate was < 0.02 °C /Myr which spanned roughly 750 Myr until about 200 Ma. At this time there was an increase in cooling rate to < 1.1 °C /Myr. Cooling remained at this rate until 125 Ma, after which it slowed down to < 0.4 °C /Myr, at which it remained until present day.

aSAR066, zSAR067: This model produced 239 acceptable paths and 25 good paths.

The best fit line shows cooling initiating at 1180 Ma and 170 °C cooling at a rate of < 0.3 °C /Myr for 215 My. Cooling rate changed at 925 Ma, slowing down to < 0.04 °C /Myr. Cooling remained at this rate until 150 Ma. After this time, the rate of cooling increased to < 0.4 °C /Myr, with a slight decrease in cooling rate at 50 Ma to < 0.3 °C /Myr.

aSAR069, zSAR068: This model produced 267 acceptable paths and 19 good paths.

Cooling began at 1135 Ma and 173 °C at a rate of < 0.2 °C /Myr. At ~800 Ma, there was cooling rate slowed to < 0.04 °C /Myr. This cooling rate persisted for 675 My, changing at 125 Ma to a much faster cooling rate of < 0.4 °C /Myr.

(a, z)SAR069: This model produced 735 acceptable paths and 324 good paths.

The best fit line shows cooling initiating at 1035 Ma and 180 °C with a cooling rate of < 0.2 °C /Myr. Cooling rate slows at 640 Ma to < 0.1 °C /Myr at which it remained until 155 Ma. After this time cooling increased to < 0.3 °C /Myr.

Summary of Model 1 results:

Samples (a, z)SAR069, aSAR069-zSAR068, and aSAR066-zSAR067 all showed an initial cooling rate of 0.2 – 0.3 °C /My for 250-400 My. Between 650 – 800 Ma, models showed a decrease in cooling rate to under 1 °C /Myr. Within very close proximity to

each other, models all showed a change in cooling rate between 150 and 125 Ma. After this time they show almost identical cooling histories with cooling rates of 0.3 – 0.4 °C /Myr lasting until present. Sample (a, z)SAR013 displays a different t-T history initially compared to the other models however after a period of rapid cooling between 200 Ma and 125 Ma, ended up with the same final cooling rate of 0.4 °C /Myr. The shift to a slower cooling rate occurs concurrently with the increase of cooling temperatures of the other samples.

Model 2:

(a, z)SAR013: This model produced 154 acceptable paths and 0 good paths.

In this model, cooling began at 950 Ma and 180 °C. The initial cooling rate was < 0.2 °C /Myr until about 475 Ma. At 475 Ma, cooling rate changes to < -0.2 °C /Myr indicating a period of reheating or burial. At 200 Ma, a rapid cooling rate is measured of < 1.2 °C /Myr. This cooling rate slows slightly at 125 Ma to < 0.4 °C /Myr.

aSAR066, zSAR067: This model produced 437 acceptable paths and 71 good paths.

This model produced a very variable cooling time temperature path. Cooling initiated at 1175 Ma with a temperature of 180 °C. The initial cooling rate was calculated to be < 0.4 °C /Myr which, persisted until 960 Ma. At this time cooling rates slowed to < 0.1 °C /Myr which endured for 435 Myr. At 525 Ma cooling rate decreased to < -0.1 °C /Myr which, is most likely the result of a period of reheating or burial. At 190 Ma, cooling rates increased to < 0.5 °C /Myr, slowing down slightly to < 0.3 °C /Myr at 83 Ma.

aSAR069, zSAR068: This model produced 469 acceptable paths and 40 good paths.

The best fit line shows cooling initiating at 1125 Ma and 180 °C with a cooling rate of < 0.2 °C /Myr. At 530 Ma, the sample experiences an increase in temperature possibly due to burial or reheating resulting in a cooling rate of < -0.1 °C /Myr. Exhumation resumed at 175 Ma with a cooling rate of < 0.4 °C /Myr.

(a, z)SAR069: This model produced 854 acceptable paths and 434 good paths.

Cooling initiated at 1000 Ma and 180 °C at a rate of < 0.2 °C /Myr. At 525 Ma, cooling stopped and the sample underwent a period of thermal stasis at 80 °C during which there was neither burial or reheating nor exhumation. This period lasted for ~365 Myr, with exhumation resuming at 160 Ma at a rate of 0.41 °C /Myr.

Summary of Model 2:

Samples aSAR069-zSAR068 and aSAR066-zSAR067 show very similar cooling paths, both reaching a low temperature of ~55 °C at ~525 Ma prior to reheating. Peak temperature of reheating is between 90 and 95 °C for the models and occurs between 175- 190 Ma. After this time both samples show rapid cooling rates of 0.4 – 0.5 °C/ My. Sample (a, z)SAR013 follows a similar t-T path, reaching a low temperature of 105 °C at 475 Ma. The peak reheating temperature of this sample coincides with samples aSAR069-zSAR068 and aSAR066-zSAR067, but at a slightly older age of 215 Ma. After this time, (a, z)SAR013 cools at a rate much faster than the other two samples. Sample (a, z)SAR069 displays a different t-T history to the other samples showing thermal stasis instead of reheating. However, the model does reach the temperature at which it remains during stasis at the exact timing that samples aSAR069-zSAR068 and aSAR066-zSAR067 reach peak low temperature prior to reheating. Rapid exhumation of Sample (a, z)SAR069 begins at a younger age compared to the other samples in this model.

Discussion

The most significant outcome from the models is the cooling event recorded as t-T paths move through constraint 3 (Figures 27, 28, 29, 30) in the scenario 2 model set (Models 2). According to the weighted mean path extracted from each sample, the rapid cooling event began at times ranging from 215 to 160 Ma, with timing of initiation decreasing northward, from 215 Ma in the south (sample SAR013), 190 Ma (sample SAR066-67), 175 Ma (sample SAR68-69), and 160 Ma (samples SAR069) (Figure 31).

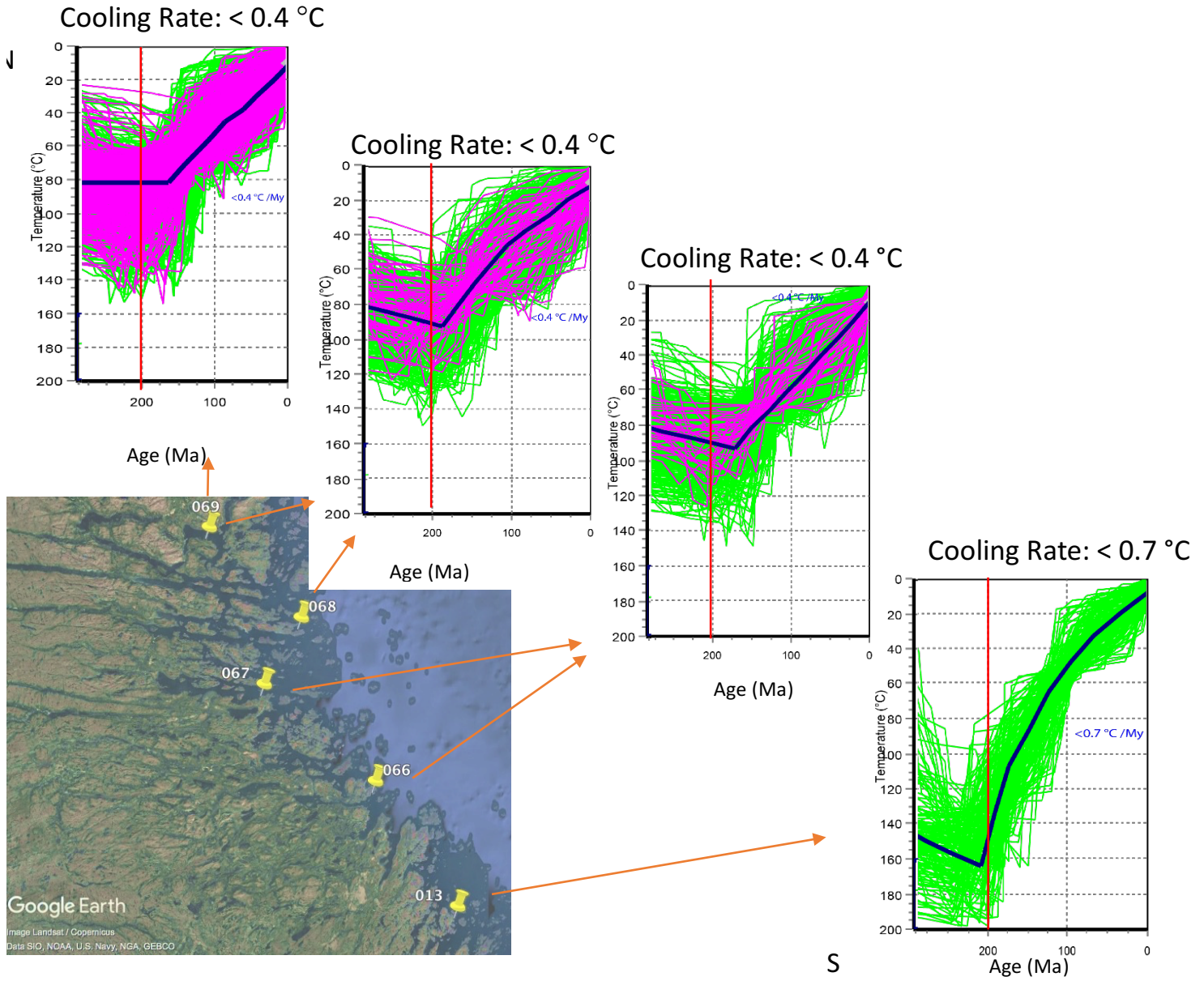


Figure 31; Snapshot of the last 300 Ma from scenario 2 of the models. A red line has been placed at 200 Ma as a reference line to help show diachronous initiation of cooling starting after 200 Ma in the south and at ~160 Ma in the northern most sample. Cooling rates are shown above figures. Green lines are acceptable paths, pink lines are good paths and the black line is the weighted mean path. Number of acceptable and good paths for each model can be found in Table 5.

This cooling phase could be attributed to tectonic exhumation related to normal faulting generated by the rifting processes. As previously discussed in the geological background, the oldest age attributed to rifting in Greenland is dated at 222.7 ± 0.3 Ma however, most ages of dyke emplacement occurred between 166 – 150 Ma (Larsen et al. 2009). Along the Labrador margin, a reheating due to syn- post-tectonic magmatic activity is not detected in our models, which could suggest that our study area is located further away from the rift axis than the exposed coast of Greenland.

An abrupt change in cooling rate is representative of exhumation due to tectonic processes such as normal faulting (Stockli 2005). The timing of these inflections in cooling rates would date the initiation of faulting (Stockli 2005). Ages at which this rapid cooling rate began in modelled t-T paths could be indicative of the initiation of the Labrador-Greenland intra-cratonic rifting as is preserved today in the rocks of the Labrador margin. This paired with continuous faulting due to increased extension as rifting developed and syn-tectonic erosion, would allow for efficient exhumation and therefore, cooling of rocks (Stockli 2005). Fault structures have been observed along the Labrador continental shelf which resulted in the formation of NW-SE trending half grabens and basins which were infilled with syn-rift deposits in the Early-Cretaceous (Dickie et al. 2011). Balkwill et al. (1990) suggest that the clastic sediments deposited along the Labrador margin were derived from local erosion of uplifted coastal areas and central Canada and transported to the margins via rivers. Uplifted coastal areas are the result of slip on the previously mentioned low angle faults and allow for faster erosion rates than flat topography.

After termination of rifting, continued erosion of topographic highs created during normal faulting could result in continued exhumation.

Importantly, the onset of the rapid cooling event seems to propagate northward through time starting at 215 Ma at the latitude of Hopedale and at 160 Ma in the North at the latitude of Nain (Figure 14). The Labrador – Greenland rift margin opened diachronously from south to north (Peace et al. 2016). This clear space-time gradient of continental cooling might result from a propagation in rifting from South to North as the craton was extended, a spatial pattern in agreement with that of the opening of the Labrador Sea. The samples display similar cooling rates which suggests that although

rifting occurred at a different timing at these locations, samples underwent the same processes.

Furthermore, this final cooling event is preceded by a very limited degree of reheating that has partially or totally reset AHe ages (as compared to ZHe ages) (aSAR069-zSAR068 and aSAR066-zSAR067). In most models, the samples seem to have resided for prolonged period of times below or just at the base of the apatite PRZ. The limited evidences for magmatic activity along our study area suggest that the rocks have not been reheated by rift-related magmatism.

Conclusion:

AHe and ZHe ages were modelled using HeFTy, a thermal modelling software, to quantify the crustal cooling of the margin to help denote exhumation as a result of rifting between Labrador and Greenland. Cooling histories obtained from our modelled results showed slow cooling followed by an increase in cooling rate during the Jurassic – Early Cretaceous. This timing is contemporaneous with initiation of rifting in the Labrador Sea. Time-temperature cooling paths showed a northward decreasing timing of initiation of cooling which was interpreted to be due to diachronous rifting from south to north yielding progressively younger ages in the North. Exhumation was most likely a result of normal faulting and subsequent erosion along the Labrador margin. We conclude that based on the models, we can interpret to see a rifting signal using (U-Th)/He thermochronology of apatite and zircon along the Labrador margin. This signal shows a spatial and temporal constraint on the propagation of the rift system through a diachronous change in initiation of cooling. Future work needs to be done to better constrain this signal by using more thermochronometers (fission track of apatite and zircon) and extending the study area.

References

- Abdelmalak, M., Geoffroy, L., Angelier, J., Bonin, B., Callot, J., Gélard, J., & Aubourg, C. (2012). Stress fields acting during lithosphere breakup above a melting mantle: A case example in West Greenland. *Tectonophysics*, 581, 132-143. doi:10.1016/j.tecto.2011.11.020
- Attendorf, H., & Bowen, R. N. (1998). Radioactive and Stable Isotope Geology. *Surveys in Geophysics*, 19(3), 283-283. doi:10.1007/978-94-011-5840-4
- Balkwill, H., Mcmillan, N., Maclean, B., Williams, G., & Srivastava, S. (1990). Geology of the Labrador Shelf, Baffin Bay, and Davis Strait. *Geological Survey of Canada, Geology of Canada*, 293-348. doi:10.1130/dnag-gna-i1.293
- Braun, Jean & Beek, Peter & Batt, Geoffrey. (2006). Quantitative Thermochronology. Quantitative Thermochronology, by Jean Braun, Peter van der Beek and Geoffrey Batt, pp. 270. Cambridge University Press, May 2006. ISBN-10: 0521830575. ISBN-13: 9780521830577
- Brune, S. (2017, November 6). Rifts and Rifted Margins: A Review of Geodynamic Processes and Natural Hazards. <https://doi.org/10.1002/9781119054146.ch2>
- Cherniak, D., Watson, E., & Thomas, J. (2009). Diffusion of helium in zircon and apatite. *Chemical Geology*, 268(1-2), 155-166. doi:10.1016/j.chemgeo.2009.08.011
- Connelly, J. N., and B. Ryan. "Late Archean Evolution of the Nain Province, Nain, Labrador: Imprint of a Collision." *Canadian Journal of Earth Sciences* 33, no. 9 (1996): 1325-342. doi:10.1139/e96-100.
- Delescluse, M., Funck, T., Dehler, S. A., Loudon, K. E., & Watremez, L. (2015). The oceanic crustal structure at the extinct, slow to ultraslow Labrador Sea spreading center. *Journal of Geophysical Research: Solid Earth*, 120(7), 5249-5272. doi:10.1002/2014jb011739
- Dickie, K., Keen, C. E., Williams, G. L., & Dehler, S. A. (2011). Tectonostratigraphic evolution of the Labrador margin, Atlantic Canada. *Marine and Petroleum Geology*, 28(9), 1663-1675. doi:10.1016/j.marpetgeo.2011.05.009
- Doré, T., & Lundin, E. (2015). RESEARCH FOCUS: Hyperextended continental margins—Knowns and unknowns. *Geology*, 43(1), 95-96. doi:10.1130/focus012015.1
- Ehlers, T. A., & Farley, K. A. (2003). Apatite (U–Th)/He thermochronometry: Methods and applications to problems in tectonic and surface processes. *Earth and Planetary Science Letters*, 206(1-2), 1-14. doi:10.1016/s0012-821x(02)01069-5

England, P., & Molnar, P. (1990). Surface uplift, uplift of rocks, and exhumation of rocks. *Geology*, 18(12), 1173. doi:10.1130/0091-7613(1990)0182.3.co;2

Ermanovics, I. "Geology of Hopedale Block, Southern Nain Province, and the Adjacent Proterozoic Terranes, Labrador, Newfoundland." *Geological Survey of Canada* 431 (1993). doi:10.4095/183986.

Farley K. A., Wolf R. A., Silver L. T. (1996) The effects of long-alpha-stopping distances on (U–Th)/He ages. *Geochimica et Cosmochimica Acta* **60**:4223–4229.

Flowers, R. M., Ketcham, R. A., Shuster, D. L., & Farley, K. A. (2009). Apatite (U–Th)/He thermochronometry using a radiation damage accumulation and annealing model. *Geochimica Et Cosmochimica Acta*, 73(8), 2347-2365. doi:10.1016/j.gca.2009.01.015

Franke, D. (2013). Rifting, lithosphere breakup and volcanism: Comparison of magma-poor and volcanic rifted margins. *Marine and Petroleum Geology*, 43, 63-87. doi:10.1016/j.marpetgeo.2012.11.003

Guenther, W. R., Reiners, P. W., Ketcham, R. A., Nasdala, L., & Giester, G. (2013). Helium diffusion in natural zircon: Radiation damage, anisotropy, and the interpretation of zircon (U-Th)/He thermochronology. *American Journal of Science*, 313(3), 145-198. doi:10.2475/03.2013.01

Hansen, K., & Reiners, P. W. (2006). Low temperature thermochronology of the southern East Greenland continental margin: Evidence from apatite (U–Th)/He and fission track analysis and implications for intermethod calibration. *Lithos*, 92(1-2), 117-136. doi:10.1016/j.lithos.2006.03.039

Harrison, T. M., & Zeitler, P. K. (2005). Fundamentals of Noble Gas Thermochronometry. *Reviews in Mineralogy and Geochemistry*, 58(1), 123-149. doi:10.2138/rmg.2005.58.5

James, D. T., S. Kamo, and T. Krogh. "Evolution of 3.1 and 3.0 Ga Volcanic Belts and a New Thermotectonic Model for the Hopedale Block, North Atlantic Craton (Canada)." *Canadian Journal of Earth Sciences* 39, no. 5 (May 29, 2002): 687-710. doi:10.1139/e01-092.

James, D.T., Miller, R.R., Patey, R.P., and Thibodeau, S. 1996. Geology and mineral potential of the Archean Florence Lake greenstone belt, Hopedale Block (Nain Province), eastern Labrador. *In* Current research. Newfoundland Department of Natural Resources, Geological Survey, Report 96-1, pp. 85–107.

Keen, C. E., Dickie, K., & Dafoe, L. T. (2018). Structural Evolution of the Rifted Margin off Northern Labrador: The Role of Hyperextension and Magmatism. *Tectonics*, 37(7), 1955-1972. doi:10.1029/2017tc004924

Kenneth A. Farley; (U-Th)/He Dating: Techniques, Calibrations, and Applications. *Reviews in Mineralogy and Geochemistry* ; 47 (1): 819–844. doi: <https://doi.org/10.2138/rmg.2002.47.18>

Ketchum, R. A. (2005). Forward and Inverse Modeling of Low-Temperature Thermochronometry Data. *Low-Temperature Thermochronology*; 275-314. doi:10.1515/9781501509575-013

Ketchum, John W.f, Nicholas G. Culshaw, and Sandra M. Barr. "Anatomy and Orogenic History of a Paleoproterozoic Accretionary Belt: The Makkovik Province, Labrador, Canada." *Canadian Journal of Earth Sciences* 39, no. 5 (2002): 711-30. doi:10.1139/e01-099.

King, A. F., & Mcmillan, N. J. (1975). A Mid-Mesozoic Breccia from the Coast of Labrador. *Canadian Journal of Earth Sciences*, 12(1), 44-51. doi:10.1139/e75-005

Larsen, L. M., Heaman, L. M., Creaser, R. A., Duncan, R. A., Frei, R., & Hutchison, M. (2009). Tectonomagmatic events during stretching and basin formation in the Labrador Sea and the Davis Strait: Evidence from age and composition of Mesozoic to Palaeogene dyke swarms in West Greenland. *Journal of the Geological Society*, 166(6), 999-1012. doi:10.1144/0016-76492009-038

Peace, A., Mccaffrey, K., Imber, J., Phethean, J., Nowell, G., Gerdes, K., & Dempsey, E. (2016). An evaluation of Mesozoic rift-related magmatism on the margins of the Labrador Sea: Implications for rifting and passive margin asymmetry. *Geosphere*, 12(6), 1701-1724. doi:10.1130/ges01341.1

Reiners, P. W. (2005). Zircon (U-Th)/He Thermochronometry. *Low-Temperature Thermochronology*; 151-180. doi:10.1515/9781501509575-008

Reiners, P. W., & Shuster, D. L. (2009). Thermochronology and landscape evolution. *Physics Today*, 62(9), 31-36. doi:10.1063/1.3226750

Shuster, D. L., & Farley, K. A. (2009). The influence of artificial radiation damage and thermal annealing on helium diffusion kinetics in apatite. *Geochimica Et Cosmochimica Acta*, 73(1), 183-196. doi:10.1016/j.gca.2008.10.013

Srivastava, S. P. (1978). Evolution of the Labrador Sea and its bearing on the early evolution of the North Atlantic. *Geophysical Journal International*, 52(2), 313-357. doi:10.1111/j.1365-246x.1978.tb04235.x

Stockli, D. F. (2005). Application of Low-Temperature Thermochronometry to Extensional Tectonic Settings. *Low-Temperature Thermochronology*; 411-448. doi:10.1515/9781501509575-018

Tappe, S., Steenfelt, A., Heaman, L. M., & Simonetti, A. (2009). The newly discovered Jurassic Tikiusaaq carbonatite-aillikite occurrence, West Greenland, and some remarks on carbonatite–kimberlite relationships. *Lithos*, 112, 385-399. doi:10.1016/j.lithos.2009.03.002

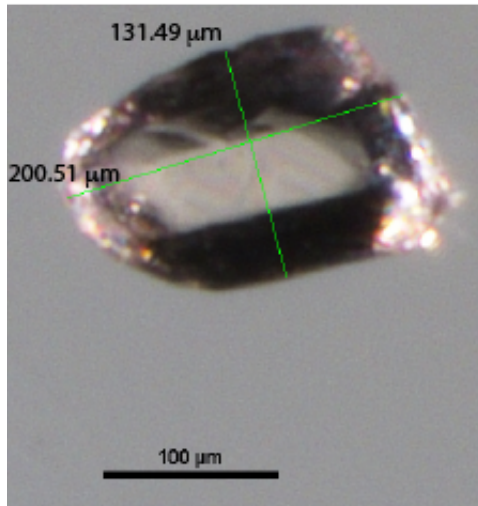
Umpleby, D. C. (1979). Geology of the Labrador Shelf. *Geological Survey of Canada*. doi:10.4095/105927

Wardle, Richard J., Donald T. James, David J. Scott, and Jeremy Hall. "The Southeastern Churchill Province: Synthesis of a Paleoproterozoic Transpressional Orogen." *Canadian Journal of Earth Sciences* 39, no. 5 (May 29, 2002): 639-63. doi:10.1139/e02-004.

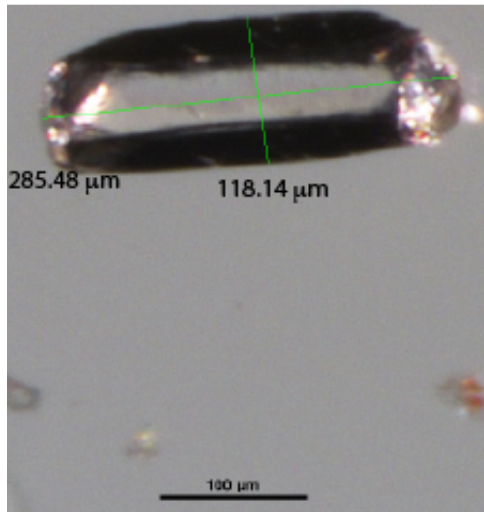
Wildman, M., Cogné, N., & Beucher, R. (2018). Fission-Track Thermochronology Applied to the Evolution of Passive Continental Margins. *Fission-Track Thermochronology and Its Application to Geology Springer Textbooks in Earth Sciences, Geography and Environment*, 351-371. doi:10.1007/978-3-319-89421-8_20

Williams, G. L., Ascoli, P., Barss, M. S., Bujak, J. P., Davies, E., Fensome, R. A., & Williamson, M. (1990). Chapter 3: Biostratigraphy and related studies. *Geological Survey of Canada, Geology of Canada*, 87-137. doi:10.4095/132698

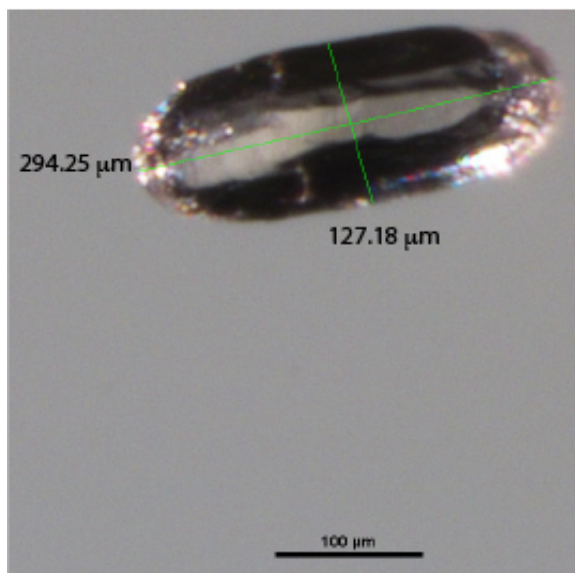
Appendix 1: Apatite Grains



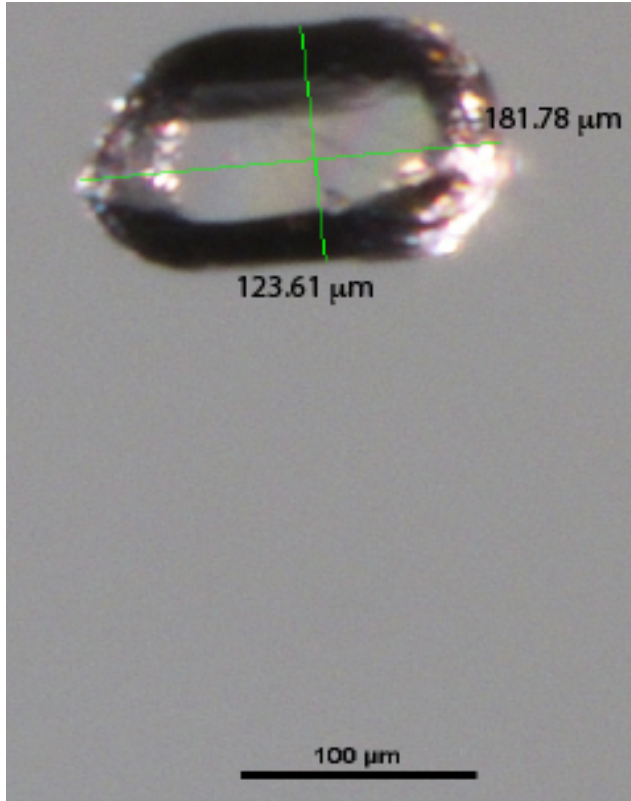
Grain aSAR013-1



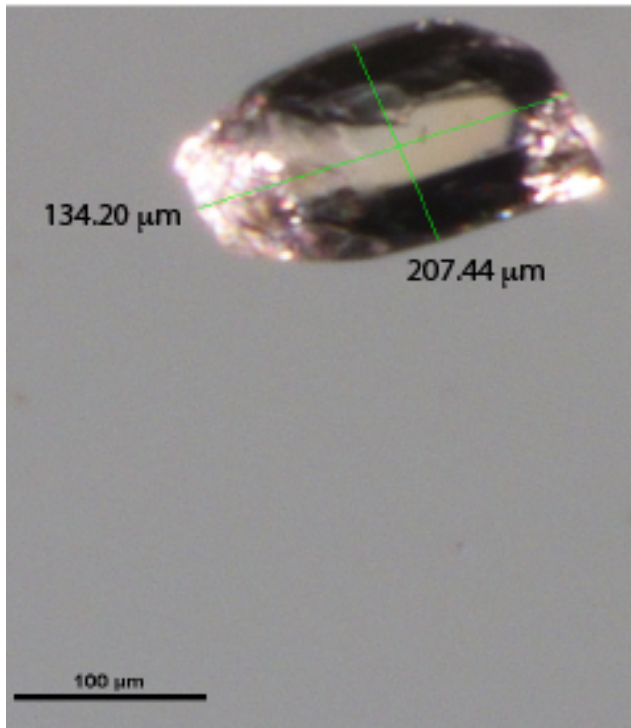
Grain aSAR013-2



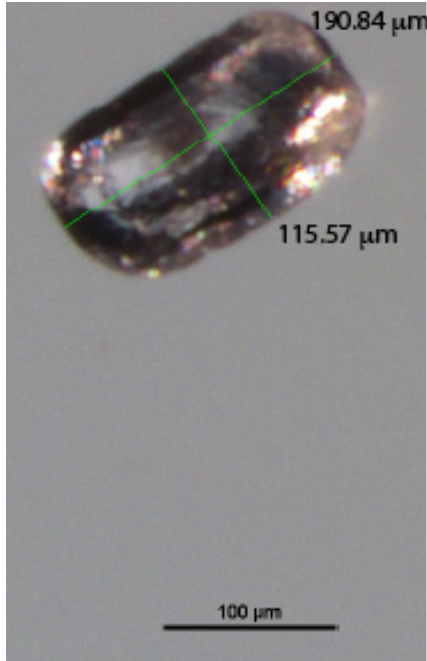
Grain aSAR013-3



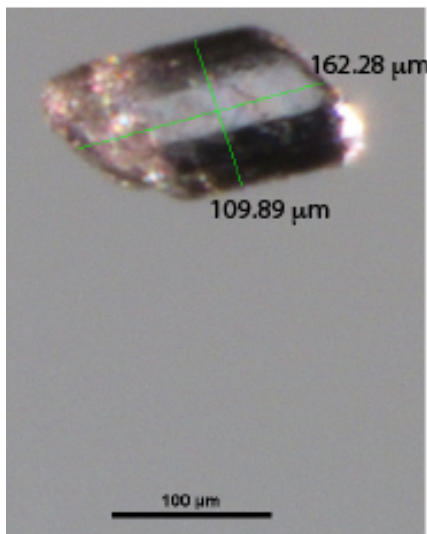
Grain aSAR013-4



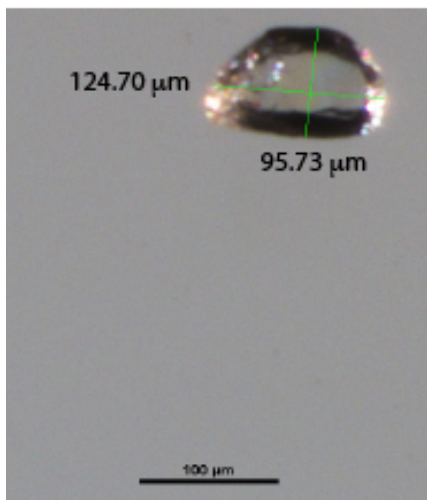
Grain aSAR013-5



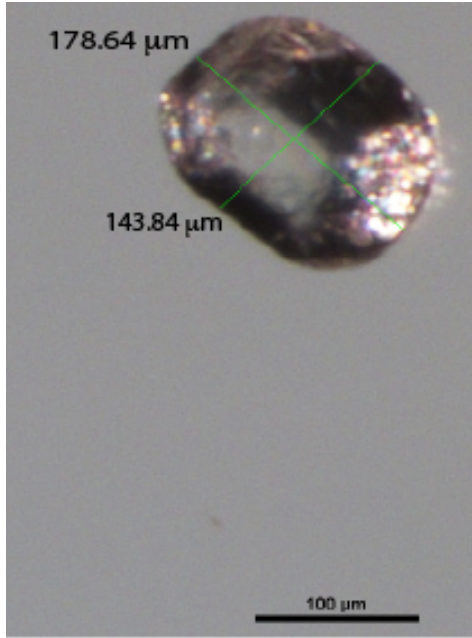
Grain aSAR066-1



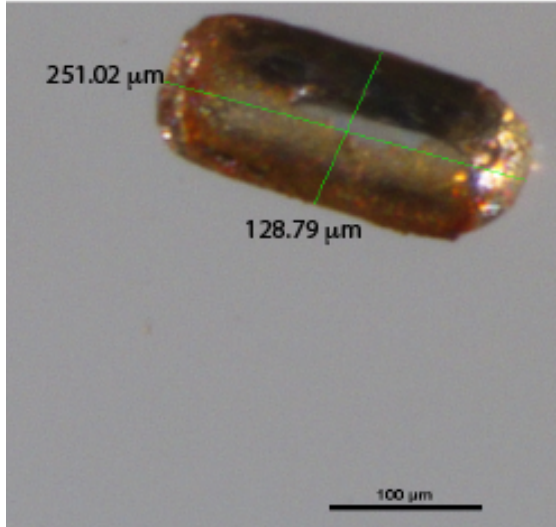
Grain aSAR066-2



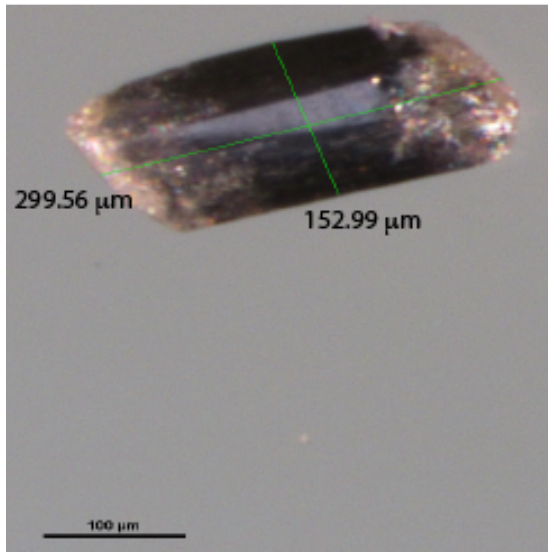
Grain aSAR066-3



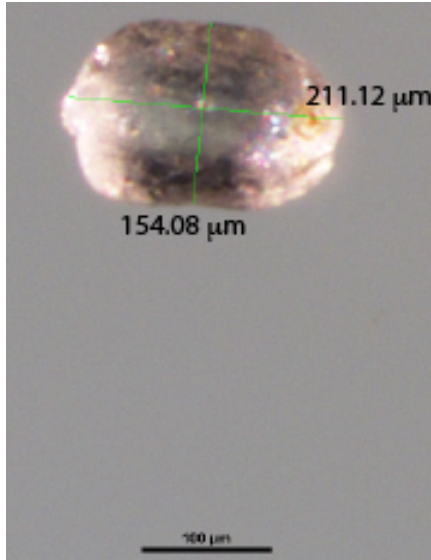
Grain aSAR066-4



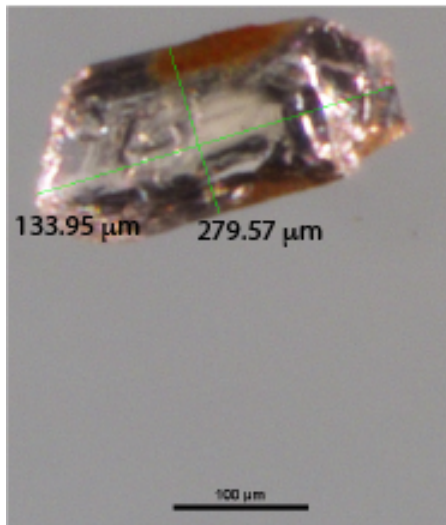
Grain aSAR066-5



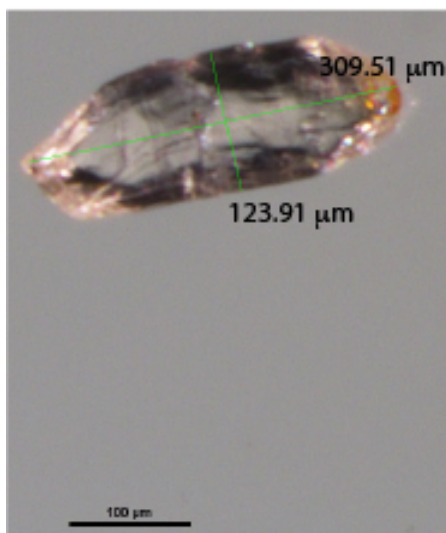
Grain aSAR069-1



Grain aSAR069-2

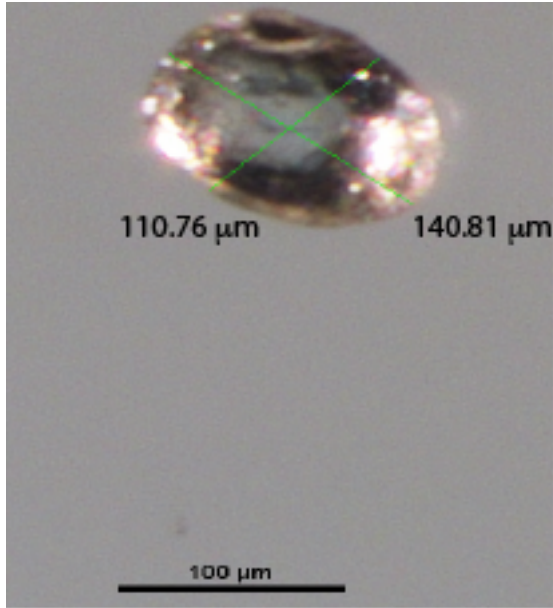


Grain aSAR069-3

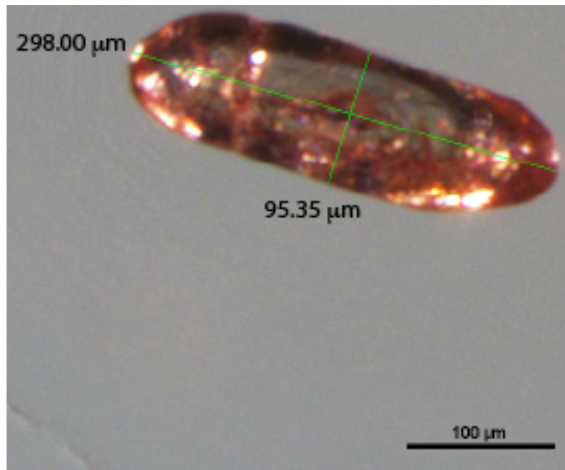


Grain aSAR069-4

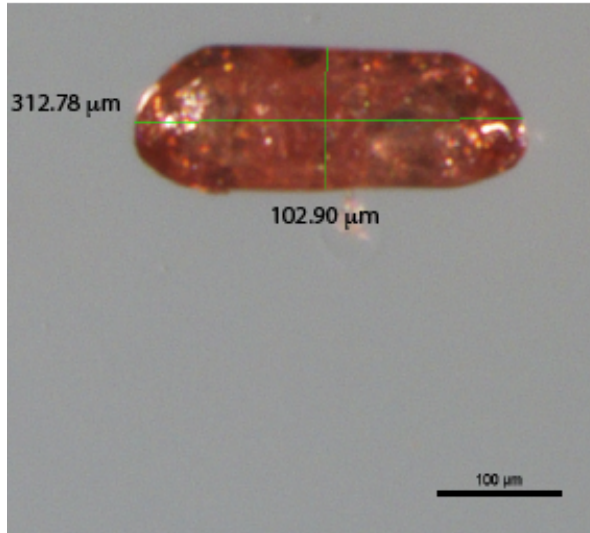
Grain aSAR069-5



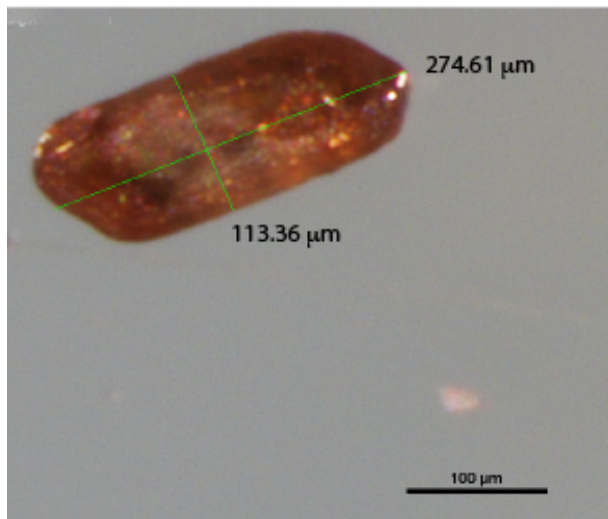
Appendix 2: Zircon Grains



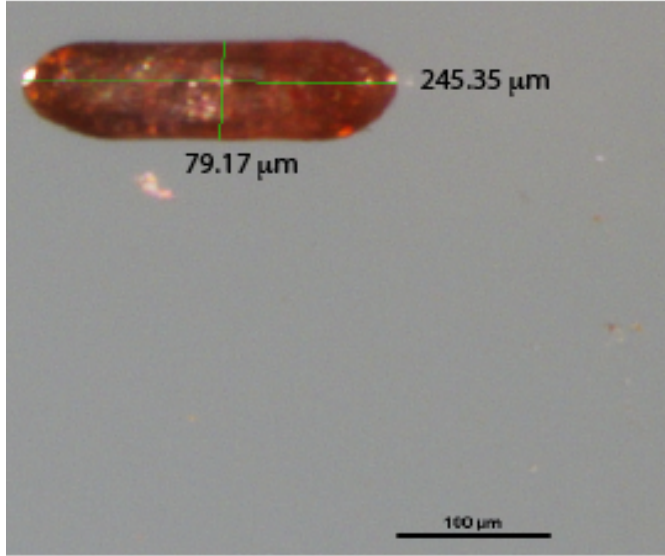
Grain zSAR013-1



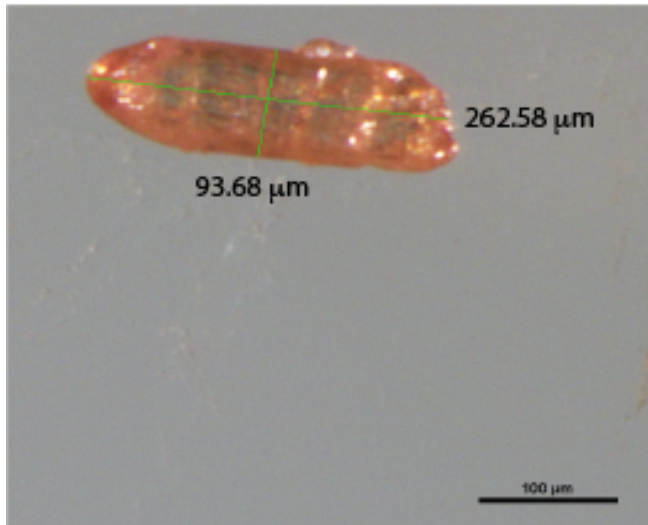
Grain zSAR013-2



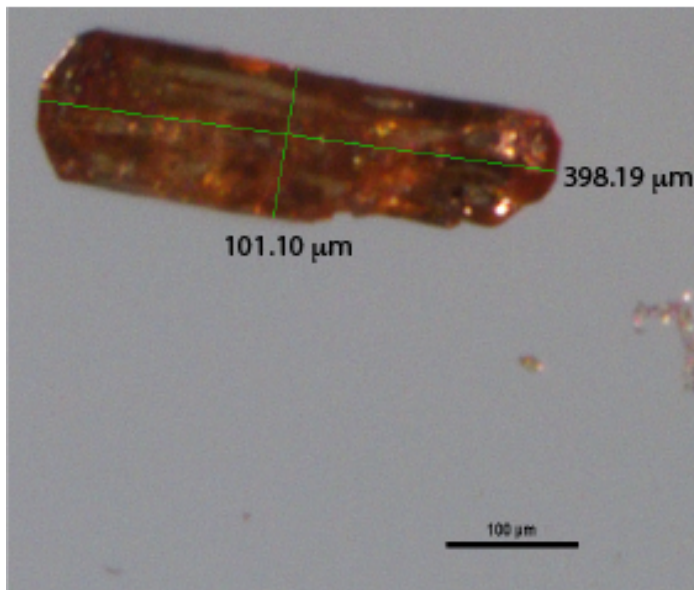
Grain zSAR013-3



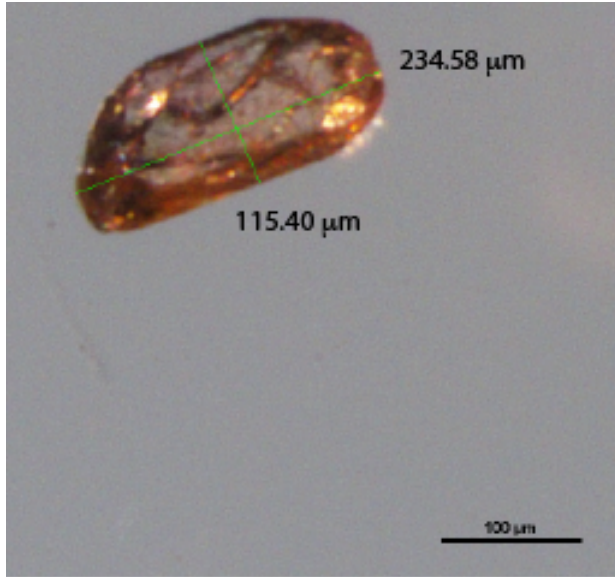
Grain zSAR013-4



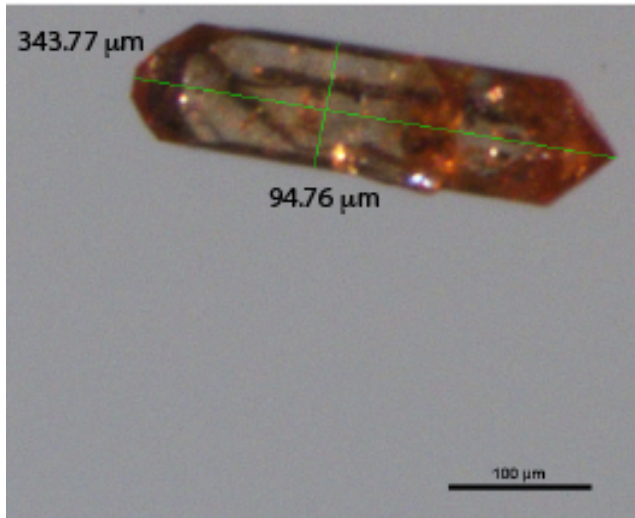
Grain zSAR013-5



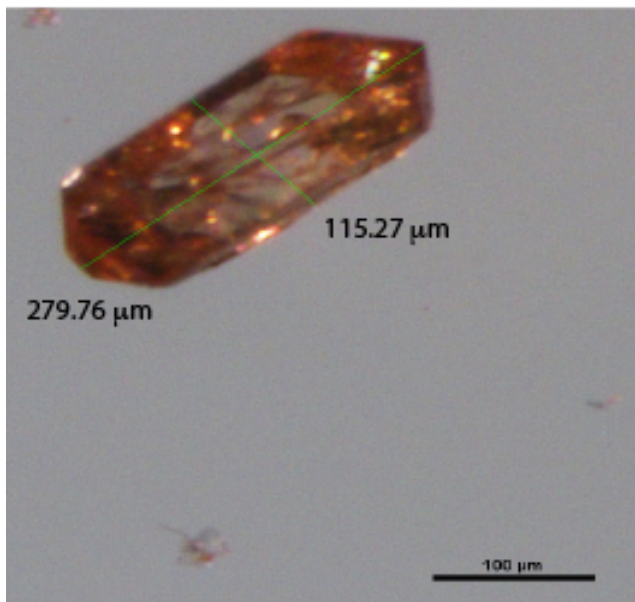
Grain zSAR067-1



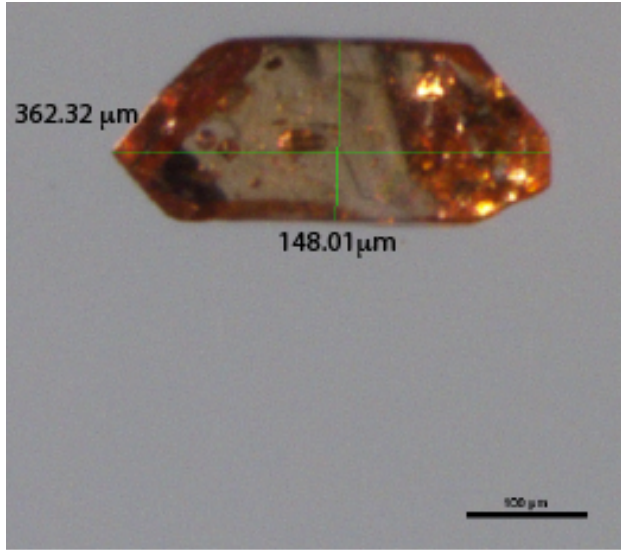
Grain zSAR067-2



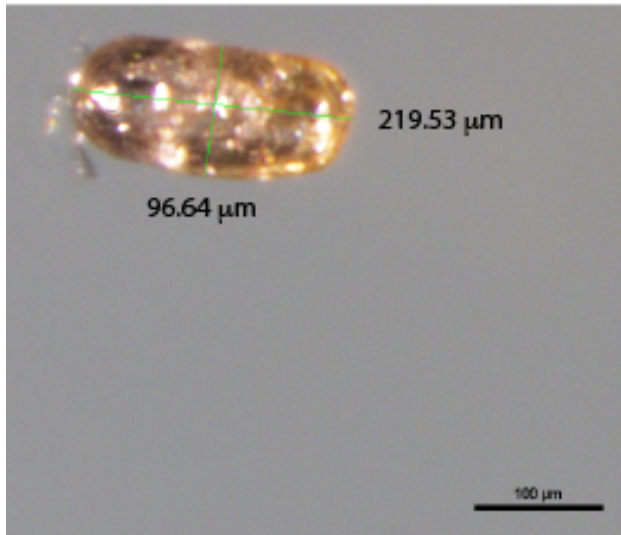
Grain zSAR067-3



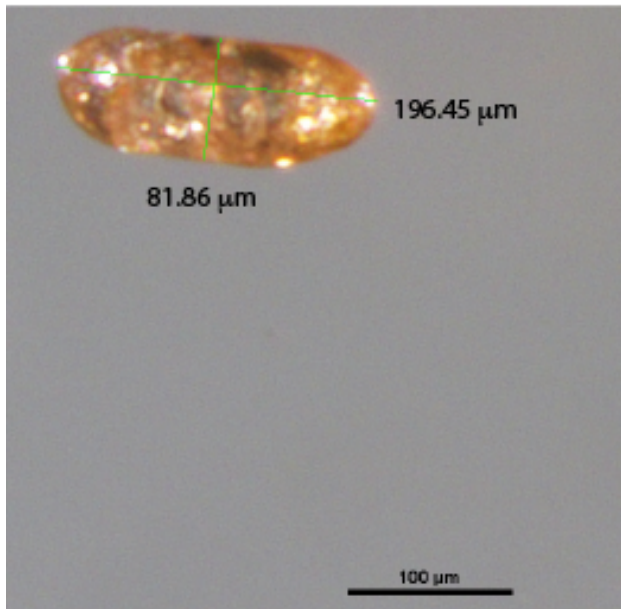
Grain zSAR067-4



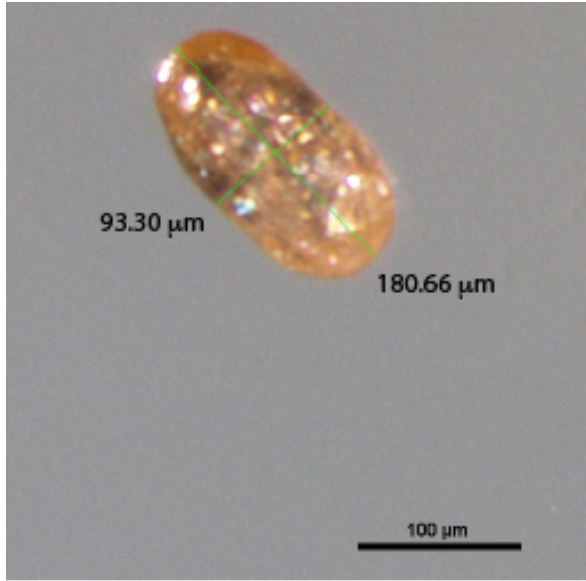
Grain zSAR067-5



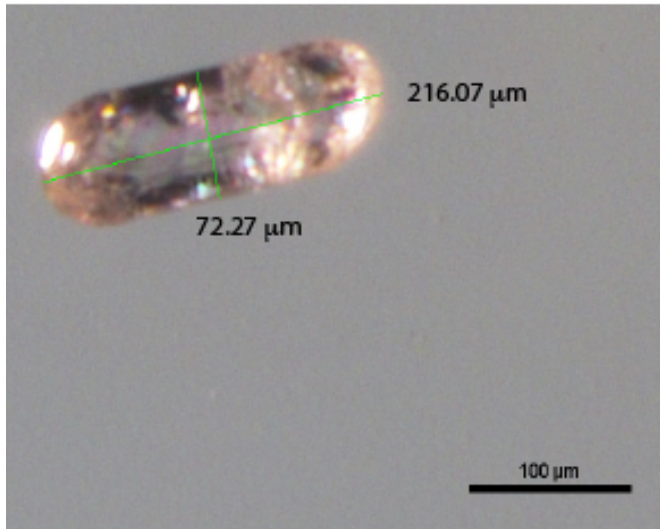
Grain zSAR068-1



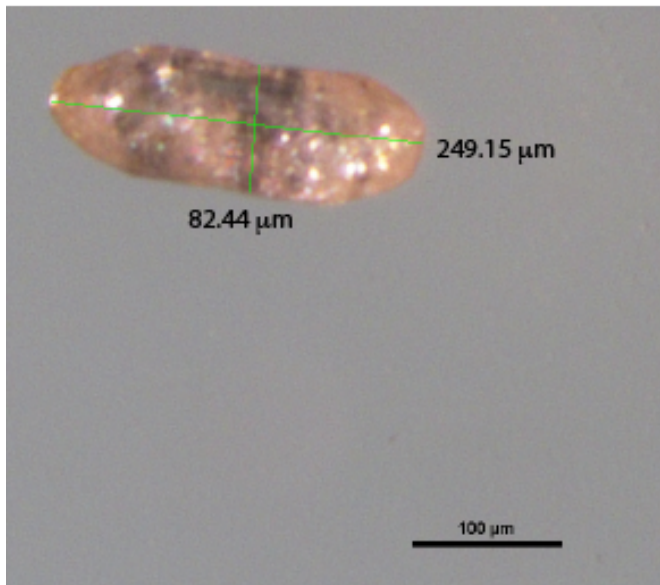
Grain zSAR068-2



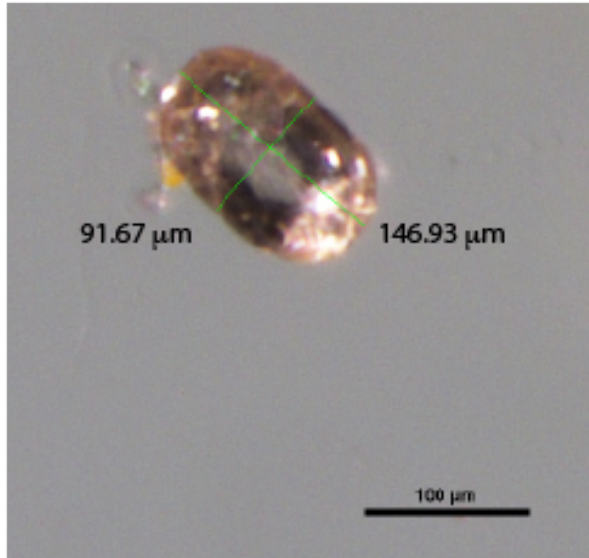
Grain zSAR068-3



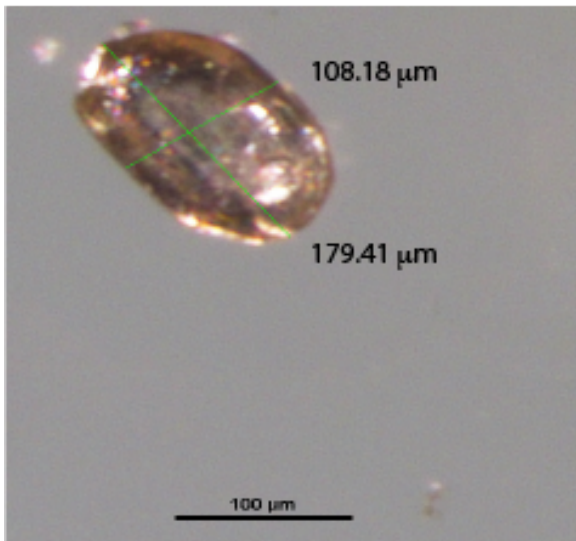
Grain zSAR068-4



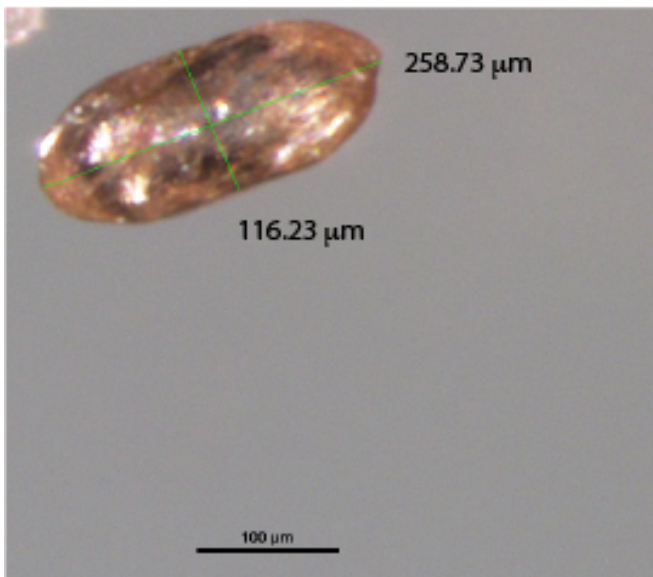
Grain zSAR068-5



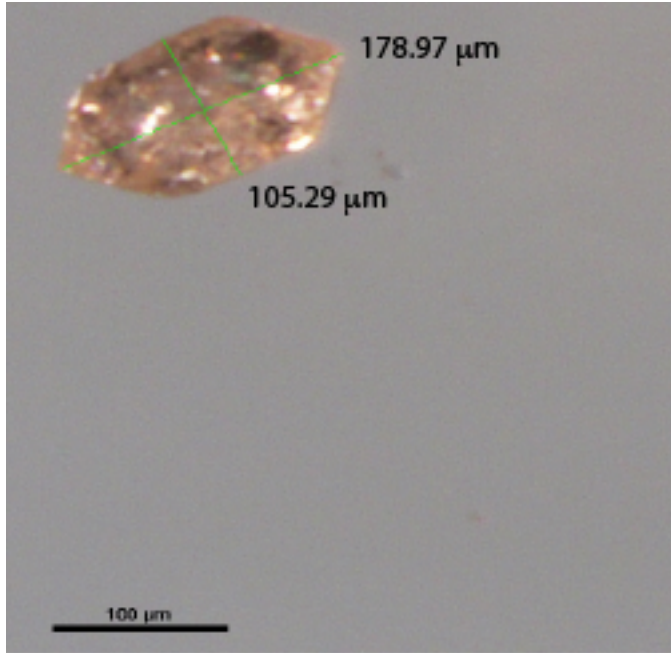
Grain zSAR069-1



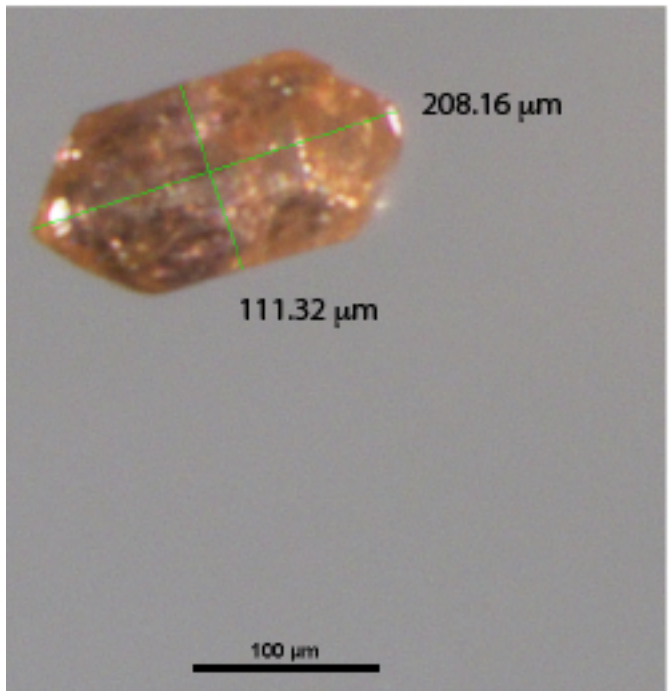
Grain zSAR069-2



Grain zSAR069-3



Grain zSAR069-4



Grain zSAR069-5